Current ground deformation along the east coastal region of China derived from GPS observations (2010-2014)

A Thesis Presented to

the Faculty of the Department of Earth and Atmospheric Sciences

University of Houston

In Partial Fulfillment

of the Requirements for the Degree

Master of Science

by

Xueyi Jia

August 2015

Current ground deformation along the east coastal region of China derived from GPS observations (2010-2014)

_____

Xueyi Jia

APPROVED:

_____

Dr. Guoquan Wang, Chairperson

_____

Dr. Michael Murphy

_____

Dr. Hyongki Lee

_____

Dean, College of Natural Sciences and Mathematics

ACKNOWLEDGMENTS

My thesis work and personal life were supported by many people, and I am pleased to have a chance to show my appreciation here.

In this acknowledgment, the order of people is not important, except the first person; my advisor Prof. Guoquan Wang. Prof. Wang discovered my potential and accepted my application for fall 2013, which offered me the opportunity to receive a superb education in the department of Earth and Atmospheric Sciences at University of Houston. He cares for my academic development. Since my second semester, Prof. Wang makes me a research assistant, which is a huge support for me. I really respect Dr. Wang's advising style. For my research, he always looks at the big picture, encourages me to develop my ideas and help me prevent several mistakes which are easy to make for new researchers.

In addition, I would like to thank Dr. Michael Murphy and Dr. Hyongki Lee, who not only oversaw this project as committee members, but gave several great advises according to their specific expertise.

I am also thankful to the other members of the HoustonNet team, my parents, and family in China.

Current ground deformation along the east coastal region of China derived from GPS observations (2010-2014)

An Abstract of a Thesis

Presented to

the Faculty of the Department of Earth and Atmospheric Sciences

University of Houston

In Partial Fulfillment

of the Requirements for the Degree

Master of Science

by

Xueyi Jia

August 2015

Abstract

This study investigated the current ground deformation that occurred along the east coastal region of China. Continuous measurements (2010-2014) from over 100 permanent GPS stations were analyzed. The GIPSY-OASIS software package (V6.3) is employed to obtain single receiver phase-ambiguity-fixed PPP solutions within a global reference frame (IGS08). To determine the magnitude and direction of local ground displacement over time, a Stable East China Reference Frame (SEChinaRF) was established using long-history data from five permanent GPS stations, which are evenly distributed along the China's east coast and have continuously operated for at least 7 years. The realization of the SEChinaRF is defined in terms of a 14-parameter Helmert transformation from the International GNSS (Global Navigation Satellite System) Reference Frame of 2008 (IGS08). The PPP daily solutions achieved 2-4 mm horizontal accuracy and 7-8 mm vertical accuracy within SEChinaRF. The local reference frame is able to identify ground deformations at the level of 1mm/year.

This study indicates that substantial land subsidence has been occurring in the Tianjin area with a steady subsidence rate of up to 45 mm/year during the past four years (2010-2014). The primary driving factor that caused the land subsidence was determined to be the excessive extraction of groundwater. Moderate subsidence (< 1 cm/year) was also observed in the east coastal regions such as Shanghai, Shandong and Guangdong. The GPS stations in eastern China also recorded significant co-seismic and post-seismic displacements induced by the

2011 Tohoku-Oki earthquake (M_W 9.0) in Japan. This study indicated that the magnitude and direction of the co-seismic and post-seismic displacement depended on both the distance and azimuth to the earthquake source. The maximum co- and post-seismic (within 3 days after the mainshock) in China was recorded by a station in Changchun, which showed 21 mm horizontal displacement toward southeast. The post-seismic deformation is still occurring in the northeastern China region with a horizontal velocity of approximately 3 mm/year toward the earthquake epicenter. No considerable vertical co- and post-seismic displacements were observed.

Table of Contents

List of Figures

List of Tables

Chapter 1 Introduction

In the past decade, Global Positioning System (GPS) technologies have been frequently applied to ground-deformation studies. High-accuracy GPS techniques are efficient and precise tools for tracking surface ground displacement, such as faulting, landslides, and subsidence (Abidin et al., 2008, Sato et al., 2003, Burkett et al., 2002, Wang et al., 2011, Wang et al., 2014). The increasing number of Continuously Operating Reference Station (CORS) networks provides abundant data for these studies to be more accurate and cost effective. As a result of the significant efforts of the International GPS Service (IGS), several hundred globally distributed GPS stations have been operating on a continuous basis, many for over 10 years. In recent years, many countries are establishing their own permanent GPS networks to support national and international geodetic and geoscientific studies. Since the beginning of the 1990s, China has established six nationwide GPS networks, which are called “National 2000 GPS Control Networks” (Yang et al., 2009). Among them, the Crustal Movement Observation Network of China (CMONOC) is one of the major scientific infrastructures, and it primarily uses GPS measurements to study ground deformation and tectonic processes in the Chinese mainland. Currently, over 260 continuously operating GPS stations have been implemented with thousands of survey-mode sites all over the mainland of China (Figure 1-1). These stations are mostly distributed in the areas with active tectonic or ground motions, such as the edge of the Tibet plateau and the Sichuan Basin. Among them, there are over 70 permanent GPS stations

distributed along the east coastal region of China (<15 km from the coast), which has been collecting data for over four years (2010-2014).

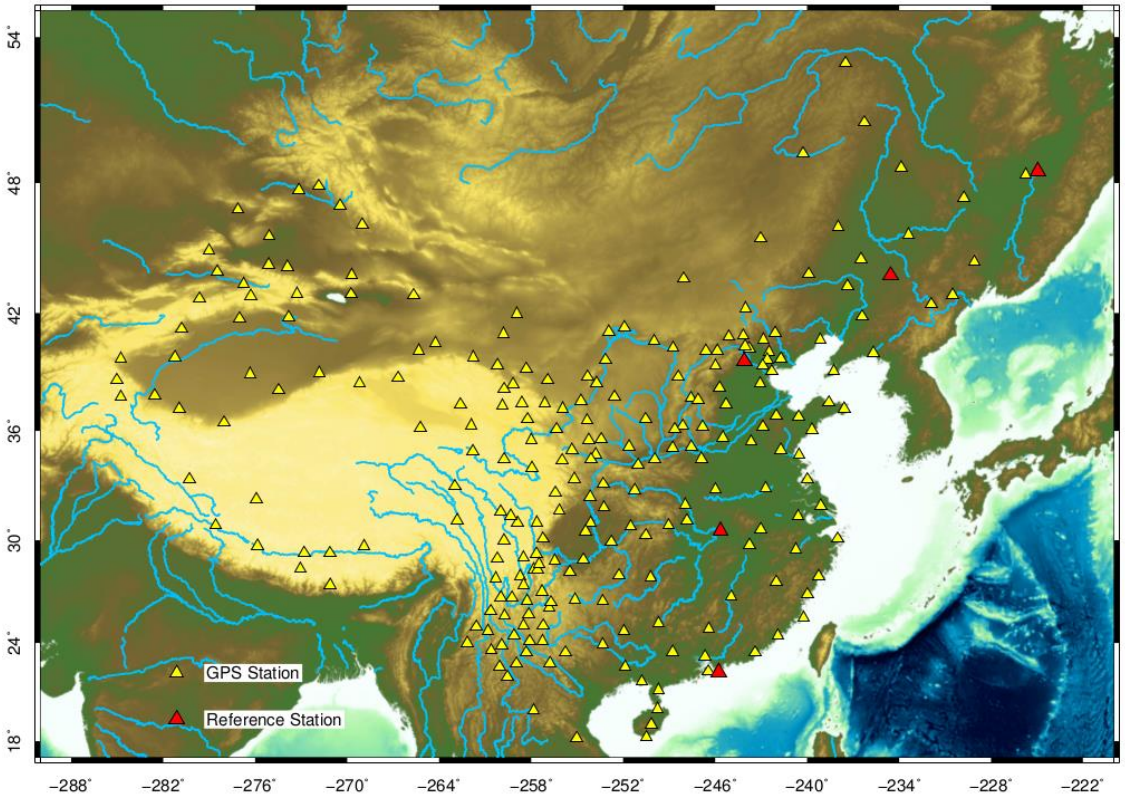

Figure 1-1 Map showing the distribution of 260 CMONOC CORS GPS stations. The yellow triangles represent the locations of the GPS stations. The red triangles represent the five selected frame stations.

There are several methods to process the raw GPS data and obtain the position Cartesian and geodetic coordinates. Originally, differential GPS (DGPS) technology was widely used for geodetic studies and surveys. DGPS is a kind of GPS Augmentation system based on an enhancement to primary GPS constellation information. It works based on a reference network, which is comprised of a number of fixed, ground-based reference stations working

continuously, to broadcast of differential information to a rover, and improve the accuracy of its position. However, in recent years, more and more researchers prefer the precise point positioning (PPP) method for accurate GPS positioning. With the single dual-frequency GPS receiver, PPP method is able to provide position solutions at centimeter to decimeter level (Samper et al., 2011). And in static mode, PPP method can produce daily positions with a 2-3 mm horizontal accuracy and a 6-8 mm vertical accuracy within a global reference frame (Bertiger et al., 2010). This approach is now widely used among the geodesy community because of the improvement of GPS orbit and clock data products in both precision and quantity. These products can be applied to reduce the errors in GPS satellite orbits and clocks, which, consequently, largely improved the position accuracy provided by PPP method.

In Chapter 2, a Chinese national GPS network project, the Crustal Movement Observation Network of China (CMONOC), along with other international organizations which archive and provide the GPS data were introduced. The database for this study is comprised of the GPS data gathered from these networks and organizations. A review of the current knowledge of PPP method, the history of the PPP method, and the advances made in PPP over the last two decades was also presented. The GIPSY/OASIS software package, which was used to employ the PPP method for GPS data processing, was discussed in the end of this chapter.

Initially, the PPP method provides position coordinates in a global reference frame, such as the International GNSS Service Reference Frame of 2008 (IGS08) (Rebischung et al., 2012). All sites are moving within a global reference frame, and it is difficult to isolate the local ground deformations within a global reference frame; however, most researchers are interested in local ground deformations. Before this study, no local-scale reference frame for the east coastal region of China has been established.

In chapter 3, a local-scale reference frame, the Stable East China Reference Frame (SEChinaRF), is defined and examined. The establishment of the SEChinaRF included the selection of reference stations, the realization of the Helmert transformation, and the calculation of the 14 transformation parameters. Examples of the products derived from the SEChinaRF were presented. Such products included the three-component displacement time series of the five reference stations, as well as the horizontal and vertical velocity fields of east China. Within the SEChinaRF, current ground deformations occurred along the east coastal region of China, such as land subsidence and co-seismic displacement, would be investigated in the following chapters.

Land subsidence is an environmental geological phenomenon that causes the slow lowering of ground-surface elevation. Increased flooding and other widespread impacts of land subsidence result in large amounts of economic costs every year. The impacts of subsidence are further increased by extreme weather events (short-term) and rising sea levels (long-term). In China, land subsidence is

currently occurring in many cities in the eastern and middle regions of the country, especially coastal cities, such as Shanghai and Tianjin (Xue et al. 2005). Tianjin is the largest coastal city in northern China. In the process of urbanization, Tianjin has experienced extensive groundwater withdrawal, and seriously suffered from land subsidence for the past 50 years. To prevent the increase of the damaging impacts in the near future, it is critical to address land subsidence related problems now.

In chapter 4, current land subsidence in the Tianjin area was examined based on the vertical displacement time series referred to SEChinaRF at four GPS stations. This part of study involved an assessment of land subsidence in Tianjin. Questions regarding the main driving factors of the subsidence, the current subsidence rates, and future scenarios were investigated. In chapter 5, land subsidence in other coastal provinces/cities, including Shanghai, Shandong, and Guangdong, was examined. Through the scrutiny of the vertical displacement position time series, different patterns of land subsidence at different regions were observed and discussed.

On March 11, 2011, a mega-thrust earthquake occurred off the coast of northeastern Japan, and it was named the 2011 Tohoku-Oki Earthquake. This earthquake resulted from sudden rupture along the portion of the megathrust fault below the area in east of Japan (Figure 1-2). During that rupture, the Pacific plate slid many meters westward beneath Japan. It was the most powerful earthquake ever recorded to have hit Japan, and the fourth-most powerful earthquake in the

world since modern record-keeping began in 1900. GPS network observations of the Tohoku-Oki earthquake of 11 March 2011 (Mw 9.0) revealed that the co-and post-seismic displacement included eastward movement of up to 5.3 m and subsidence of up to 1.2 m in the eastern Japanese island area (Ozawa et al., 2011). Meanwhile, considerable far-field co-seismic ground deformation were recorded at most GPS stations in the east coastal region of China. In chapter 6, in order to understand the impacts of the 2011 Tohoku Earthquake on the ground surface in the east coastal region of China, the far field co- and post-seismic displacement recorded at several stations were investigated and discussed.

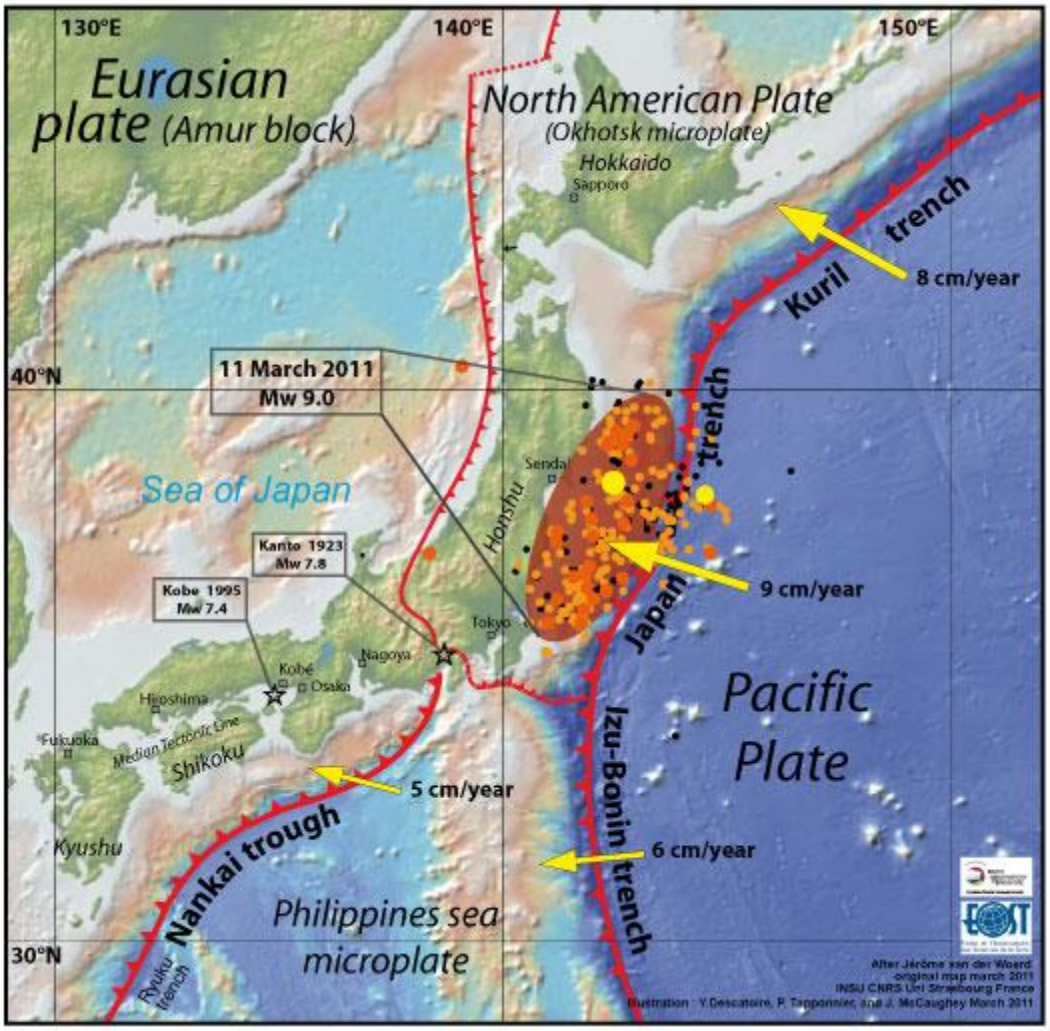

Figure 1-2 Map of the four tectonic plates in and near Japan. Red lines show the faults that form the plate boundaries; the yellow arrows show the motion of the plates related to fixed Eurasian plate. The largest yellow dot shows the epicenter of the earthquake. The smaller yellow dot shows the largest aftershock to date. Smaller dots show lesser aftershocks. (Source: Descatoire, 2011)

Chapter 2 GPS/GNSS networks and data processing

2.1 Introduction

Throughout time, a variety of ways have been developed to locate positions on earth and to navigate from one place to another. Celestial bodies like the sun and stars were used by early mariners to get an approximate knowledge of their location. In the 1920s, radio navigation was introduced, which used the radio frequencies to determine a position on earth. During the Cold War in the 1960s, the global positioning system (GPS) was designed for military and intelligence applications. It is a network of satellites that orbit the earth at fixed points above the planet and send signals to a GPS receiver on earth to locate the exact position, speed, and time anywhere on the planet.

In 1960, the US government launched the first satellite system, Transit, The five Transit satellites orbiting the earth allowed ships to fix their position on the seas once an hour. Between 1978 and 1985 a total of 11 "Block" satellites were launched. GPS developed quickly for military purposes during this period; however, it was not until the Soviet Union shot down a Korean passenger jet - flight 007 - in 1983 that the Reagan Administration in the US allowed GPS for civilian applications. As a result, aircrafts shipping and transporting all over the world could fix their positions and avoid straying into restricted foreign territory. Upgrade of the GPS was delayed by the NASA space shuttle Challenger disaster in 1986, and until 1989, the first Block II satellites were launched. In 1993, the US launched their 24th Navstar satellite into orbit, which completed the modern GPS constellation of

satellites - a network of 24 - known now as the Global Positioning System (GPS). The GPS network currently has 31 active satellites in the GPS constellation (Figure 2-1).

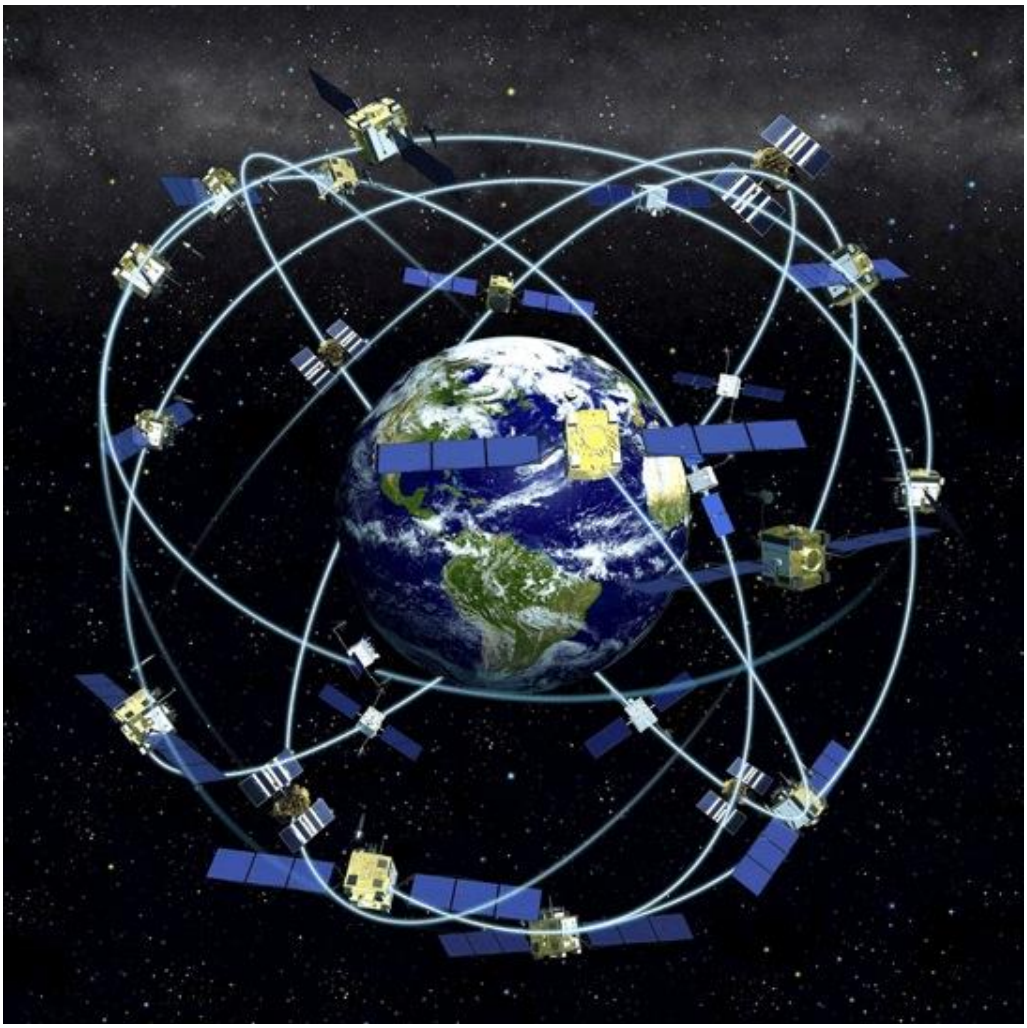

Figure 2-1 The Global Positioning System is a constellation of satellites (currently, a total of 31 satellites) that orbit the earth twice a day, transmitting precise time and position (latitude, longitude and altitude) information. (Source: http://cdn.fieldtechnologies.com/wp-content/uploads/2011/10/gps-system.jpg)

GNSS stands for Global Navigation Satellite System. It is the standard generic term for satellite navigation systems that provide autonomous geo-spatial positioning with global coverage. This term includes the GPS, GLONASS, Galileo, Beidou, and other regional systems (the term GPS is specific to the United States' GNSS system). The availability of Global Navigation Satellite System (GNSS) data provided by Continuously Operating Reference Stations (CORS) has opened the door for many applications, including ground deformation studies, researches of the global ionosphere, icebergs, and water vapor, marine and land navigation, and aircraft positioning and guidance (Klobuchar, 1987; Jonsson, 2002; Lachapelle, 2009). The increased number of CORS networks provided abundant GPS data for these studies to be more accurate and cost effective. The infrastructure of the GPS network has raised the attention of many counties. The Chinese GPS network project is named the Crustal Movement Observation Network of China (CMONOC). GPS Data gathered from CMONOC is one important part of the database of this study. The networks of U.S National Geodetic Survey (NGS) and UNAVCO also archive a large amount of GPS data from the several permanent stations established by other organizations. These long-history data were critical for a variety of purposes in this study.

2.2 Database—Chinese GPS data

2.2.1 CMONOC

China has established six nationwide GPS networks since the beginning of the 1990s for different research purposes. With the support of the IGS network and

advanced data-processing strategies, by integrating the six existing GPS networks, an accurate and unified national GPS control network with more than 2500 sites has been established, which is called “National 2000 GPS Control Network” (Yang et al., 2009). The Crustal Movement Observation Network of China (CMONOC) is one of the major scientific infrastructures that mainly uses GPS measurements to study earthquake and tectonic processes in the Chinese mainland. The first phase of the national GPS network of China was implemented in 1998. In Phase I of the project, 27 continuous GPS stations as well as over 1000 campaign sites were established. The follow-up Project (Phase II) of CMONOC, was implemented with an additional 1000 campaign sites and 223 continuous GPS stations in 2007 (Li et al., 2012).

The distribution of the GPS stations of CMONOC is illustrated in Figure 2-2. These GPS stations are mostly located in the areas with active tectonic or ground motions, such as the edge of the Tibet plateau and the Sichuan Basin. Among these stations, there are over 70 continuous GPS stations along the east coastal region (<15 km from the coast) of China, which have collected data for over four years (2010-2014). Most of these GPS stations are located in large coastal cities, such as Tianjin, Qingdao, Shanghai, and Guangdong. Figure 2-3 shows the photos of four CMONOC GPS stations at Rikeze, Xinjiang, Urumqi, Xinjiang, Xulun Hoh, Inner Mongolia and Taian, Shanxi.

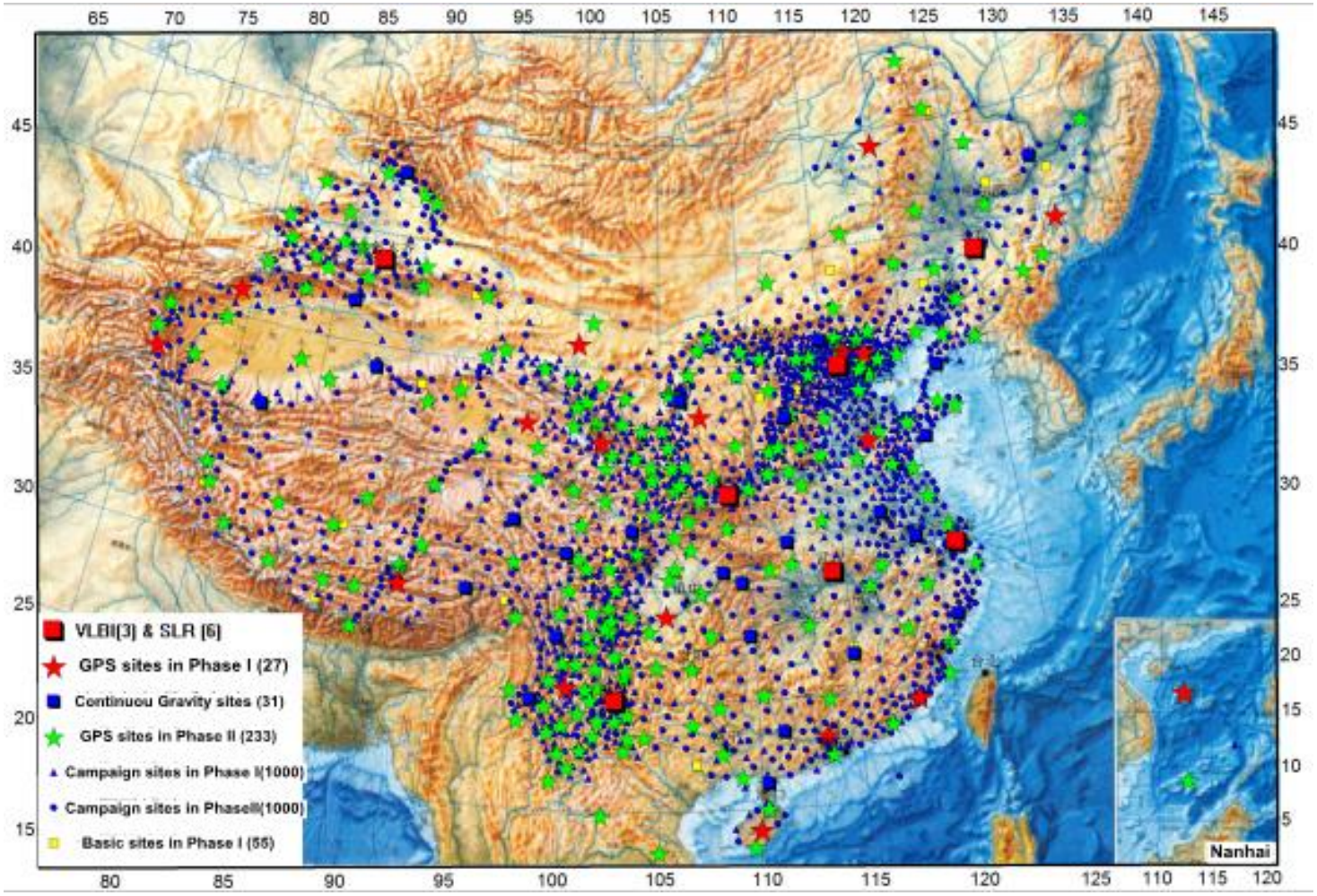

Figure 2-2 Map illustrating the infrastructures of the Crustal Movement Observation Network of China (CMONOC) (Li et al., 2012).

Figure 2-3 Photos of permanent GPS stations of CMONOC at different locations (Source: http://www.cdstm.cn/viewnews-118012.html-page-3).

2.2.2 GPS Data archived by other networks

UNAVCO is a non-profit university-governed consortium that facilitates geoscience research and education using geodesy. It is funded by the National

Science Foundation (NSF) and The National Aeronautics and Space Administration (NASA). Currently, UNAVCO archive data of over 3,400 GPS stations from a variety of networks. Among them, 9 GPS stations are located along the east coast of China, of which the raw GPS data are freely available to the public (http://facility.unavco.org/data/data.html).

The International GNSS Service (IGS) is a voluntary federation of more than 200 worldwide agencies that manage resources and permanent GPS station data to generate precise GPS products. The IGS also provided the high quality data of the GPS stations all over the world. Figure 2-4 shows the GPS stations, of which the data are archived by the IGS around the mainland of China. Each green point presents a permanent GPS station. The data of these stations can be freely downloaded from the IGS website (http://igs.org/network).

In additional, the Nevada Geodetic Laboratory (NGL) processes the GPS RINEX data files using the JPL GIPSY-OASIS II software package and provides the XYZ coordinates and other outputs. NGL reprocesses all the GPS data from UNAVCO, CORS and other GPS Data networks and has aggregated the results for more than 8,000 stations. In this study, the GPS data of 3 stations in Hong Kong and 7 stations in the Shandong province were gathered from NGL.

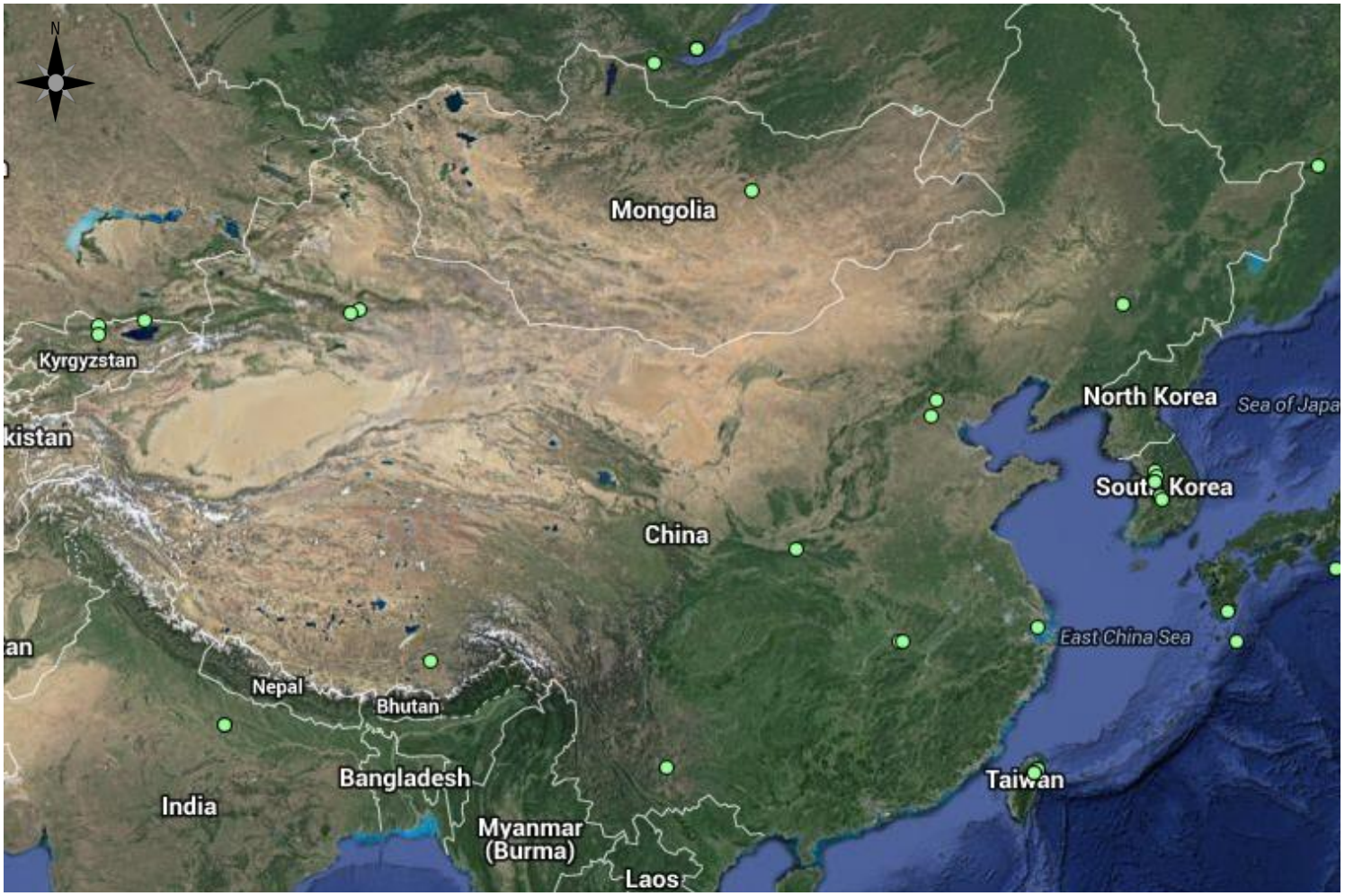

Figure 2-4 Map showing the GPS stations in International GNSS Service (IGS) network around China. The green point presents the location of a GPS station. The data of these stations are archived by IGS and are freely available to the public (Source: http://igs.org/network).

2.3 Precise point positioning method

2.3.1 PPP

Raw GPS data gathered from multiple networks and organizations (CMONOC, UNAVCO, and IGS) are filed in the RINEX format. The precise point positioning (PPP) method was applied to process these data in this study. PPP uses un-differenced dual-frequency pseudo-range and carrier-phase observations along with precise satellite orbit and clock information to determine the position of a stand-alone GPS station (Blewitt, 1989; Zumberge et al., 1997; Kouba and Springer, 2001; Ray et al., 2004; Kouba, 2005). The concept of Doppler satellite precise point positioning was proposed by Anderle (1976); however, this technique was not passionately studied until the late 1990s. Over the past two decades, dual-frequency PPP has been extensively researched, and several PPP software packages have been developed, such as GAMIT and GIPSY-OASIS. Centimeter-level point positioning is achievable in post-processed, static receiver mode of PPP method. (e.g., Zumberge et al., 1997; Gao and Chen, 2004; Choy et al., 2009).

Post-processed PPP method has many applications in geodesy and geoscience, such as the determination of the coordinates of receivers for the densification of the International Terrestrial Reference Frame (ITRF) datum, the positioning of static receivers in earthquake studies (for determining pre-, co-, and post-seismic motion), and the estimation of tropospheric delay (Ray et al., 2004; Shi et al., 2010; Kouba and Heroux, 2001). PPP has also been considered to be an effective post-event tool for crustal-deformation monitoring (e.g., Melbourne et

al., 2002), ocean-tide measuring (e.g., King and Aoki, 2003), atmospheric water vapor sensing (e.g. Bar-Sever et al., 1998; Rocken et al., 2005), and many other remote sensing applications (e.g., Jin and Komjathy, 2010).

2.3.2 GIPSY-OASIS

GIPSY-OASIS is the GNSS-Inferred Positioning System and Orbit Analysis Simulation Software package. GIPSY is developed and maintained by the Jet Propulsion Laboratory (JPL). GIPSY is a set of computer programs used to analyze radiometric data with an emphasis on GPS, including many programs and scripts. GIPSY-OASIS can process data in all modes from static to fully kinematic. It now runs on the UNIX system and is generally referred to as GIPSY-OASIS II. GIPSY and OASIS are actually two separate software packages with common modules. GIPSY was designed for standard geodetic applications, whereas OASIS is a covariance analysis package for Earth orbiting and deep space missions. In this study, GIPSY-OASIS will only be referred to as GIPSY.

GPS data examined in this study were processed using GIPSY software package (V6.3) and JPL's orbit and clock products for the GPS constellation. The orbit and clock products include a record of the wide-lane and phase bias estimates from the underlying global network of GPS stations. The major parameters estimated and key models applied in the static positioning include the VMF1 troposphere-mapping model (Boehm et al., 2006), second order ionospheric delay (Kedar et al., 2003), and the ocean tidal loading model FES2004 (Lyard et

al. 2006) calculated using the free online service operated by Onsala Space Observatory, Sweden.

The PPP method employed by GIPSY produce geocentric Cartesian coordinates (X, Y, and Z) within IGS08. These three-dimensional Cartesian coordinates can be converted to geodetic coordinates (latitude, longitude, and ellipsoidal height) within the same reference frame. The GPS ellipsoidal height is the height of the point relative to the reference ellipsoid surface. It has almost identical displacement as the orthometric height at a horizontally stable site during the same time period (Wang and Soler, 2013); therefore, the ellipsoidal height displacement time series referred to IGS08 can be directly used to interpret vertical ground deformations, such as subsidence and uplift.

Chapter 3 Stable East China Reference Frame (SEChinaRF)

3.1 Introduction

China's east coastline covers approximately 14,500 km from the Bohai gulf on the north to the Gulf of Tonkin on the south. Most of the northern half is low lying, although some of the mountains and hills of Northeast China and the Shandong Peninsula extend to the coast. The southern half is more irregular, and much of the coast is rocky and steep. South of this area, the coast becomes less mountainous: hills extend more gradually to the coast, and small river deltas are common. China's east coasts are bordered to the East China Sea, Korea Bay, Yellow Sea, and South China Sea. A large number of mega cities, such as Tianjin, Shanghai, Qingdao, and Hong Kong, are located on the east coast of China. Economic development has been more rapid in coastal provinces and cities than in the interior. The three wealthiest regions of China are along the southeast coast, centered on the Pearl River Delta; along the east coast, centered on the Lower Yangtze River; and near the Bohai Gulf, in the Beijing–Tianjin–Liaoning region. The rapid development of these areas has significant effect on the Asian regional economy. However, both natural and human-induced disasters occur frequently in the east coastal region of China, affecting hundreds of millions of people every year. They have become an important restricting factor for economic and social development. Therefore, it is critical to investigate the ground deformation, such as land subsidence and earthquake impacts, along the east coastal region of China.

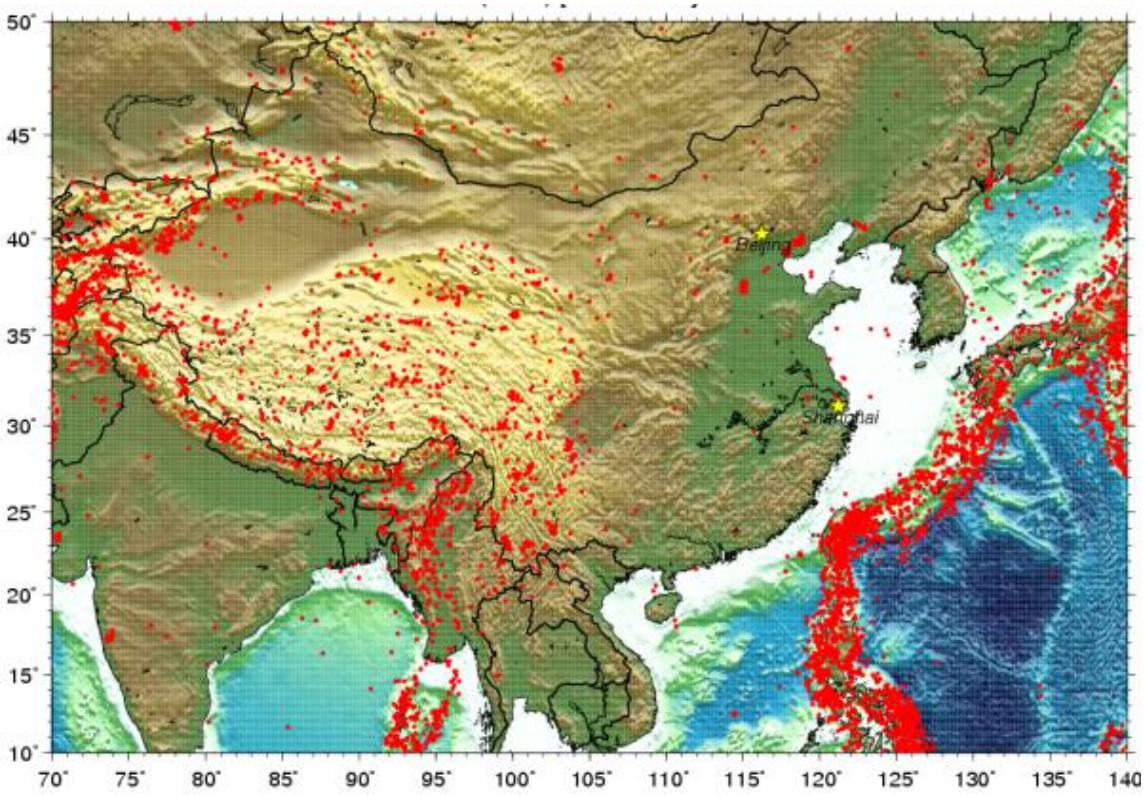

Figure 3-1 Map of Seismicity of East Asian (M>5) [1989-2005] (Source: Newman, 2013)

Figure 3-1 shows the map of seismicity of East Asian with all the earthquake of Magnitude 5 or higher from 1989 to 2005. It can be indicated that the major earthquakes occurred in eastern Asia were mainly within a triangular-shaped region. And the three boundaries of this region, which contains plateaus, mountains, and intermountain basins, are roughly the Himalayan arc, the Tianshan-Baikal, and longitude line ~105°E (Gao et al., 2011). Within this triangular region, tectonism is intense and major deformation occurs both between crustal blocks. The eastern coastal areas of China are outside this triangular region, and rigid block moves as a whole with relatively few major earthquakes and relatively weak Cenozoic deformation. Therefore, a stable local reference

frame co-rotated with rigid block of east China is geologically reasonable to be established.

Displacement time series and velocity vectors derived from GPS measurements are investigated for the purpose of studying the ground deformation in China's east coastal region. Previous studies discussed the products from GPS process based on several continental-scale reference frames, such as the International GNSS Service (IGS) reference frame of 2008 (IS08), and the Eurasia fixed-reference frame. These reference frames are realized using an approach to minimize the overall movements of a large number of selected frame stations distributed in the study area. Local ground deformation information is biased by these large-scale reference frames.

Figure 3-2 illustrates the horizontal velocity field of the current ground movement in East China constrained from GPS measurements within the IGS08 reference frame. All the stations in the China's east coastal region are moving toward the southeast with a velocity of approximately 35 mm/year within IGS08. Similarly, in the Eurasia fixed reference frame, all of the stations in the east China are also moving towards the southeast direction, although not as fast as the velocities computed within IGS08 (Figure 3-3).To remove the effect of the large-scale reference frames, a stable East China reference frame is needed. Such reference frame covering a small area will minimize the biases that occurred in a continental-scale reference frame and highlight the site-specific local ground deformations.

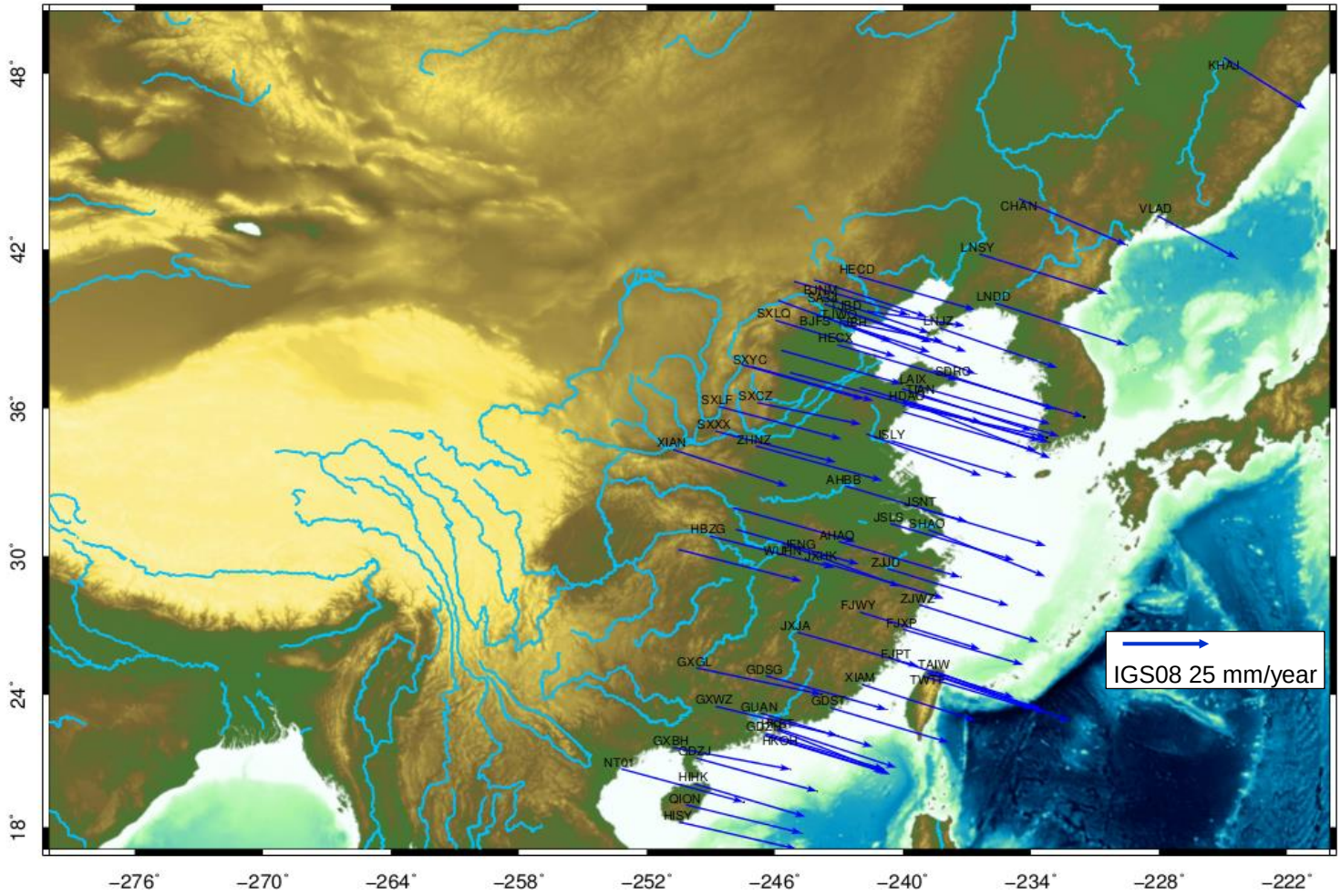

Figure 3-2 Horizontal velocity field of the current ground movement in East China constrained from GPS measurements within IGS08 reference frame.

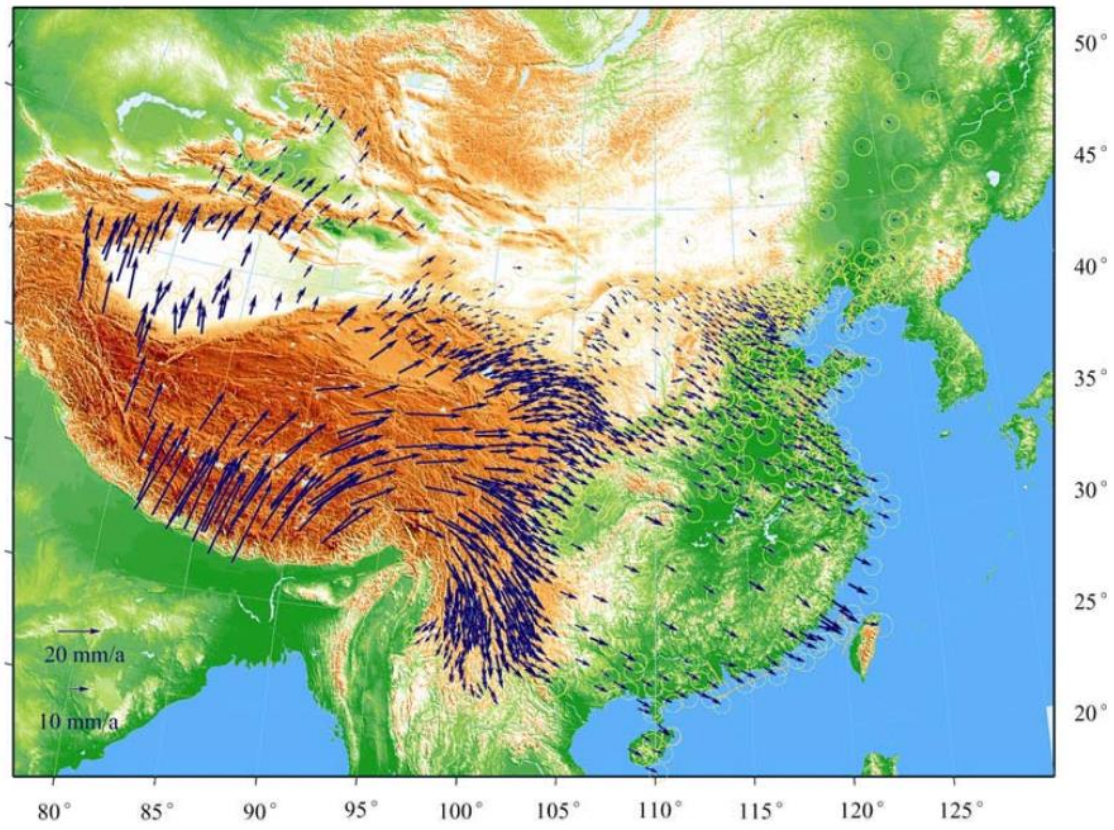

Figure 3-3 Velocity field of the current crustal movement in continental China constrained from GPS measurements in the Eurasia Fixed Reference Frame. Each arrow indicates a GPS velocity vector. (Niu et al., 2005)

3.2 Selection of reference stations

Establishing a local reference frame requires three or more common points (reference stations) to tie the two reference frames (Wang et al., 2013). A locally stable station would keep zero or “near-zero” displacement velocities within a stable reference frame. This principal is used to assess the stability of local reference frames in this study. In practice, more reference stations often result in

better transformation parameters with the least squares iteration routine (e.g., Snay, 1999; Soler and Snay, 2004); however, a reference station that is not locally stable would degrade the accuracy of the reference frame. Thus, the selection of reference stations is critical for establishing a stable local reference frame. The principal for the selection of a set of reference stations includes good geographical distributions, long measurement histories, clean daily position time series, and stable site locations (e.g., Blewitt and Lavallee, 2002; Collilieux et al., 2007).

The locations and distribution of the five reference stations selected for this study were shown in Figure 1-1. The detailed geographical information of the five reference stations is listed in Table 1-1. WUHN is located in Wuhan University, Hubei, China. It began collecting data in March of 1996. BJFS is located in the Fangshan District, Beijing, and the collecting of data at BJFS began in September of 1998. KHAJ, with 11 years of collected data (2001 to 2012), is located at Khabarovsk, Russia. CHAN is located in Changchun, China, and this station began to record GPS data in October of 2004. HKOH has a data history of 10 years (2005-2014) and is located at the Shek O Country Park, Hong Kong. Figure 3-3 shows the photos of the three reference stations WUHN, BJFS, and CHAN.

Table 3-1 Geographical information of 5 Frame Stations Derived from GIPSY PPP Solutions within the IGS08 Reference Frame

Station	Date Installed	Latitude	Longitude(°)	Height(m)	Location
WUHNN	01/1993	30.532	-245.6427	25.825	Wuhan
KHAJ	05/1996	48.5214	-224.9538	130.4763	Khabarovsk*
BJFS	09/1995	393631.05	-244.1075	60.06	Beijing
CHAN	07/2000	43.7905	-234.5558	271.53	Changchun
HKOH	10/2000	22.492	-245.7714	41.178	Shenzhen

*Khabarovsk is a city in the east of Russia.

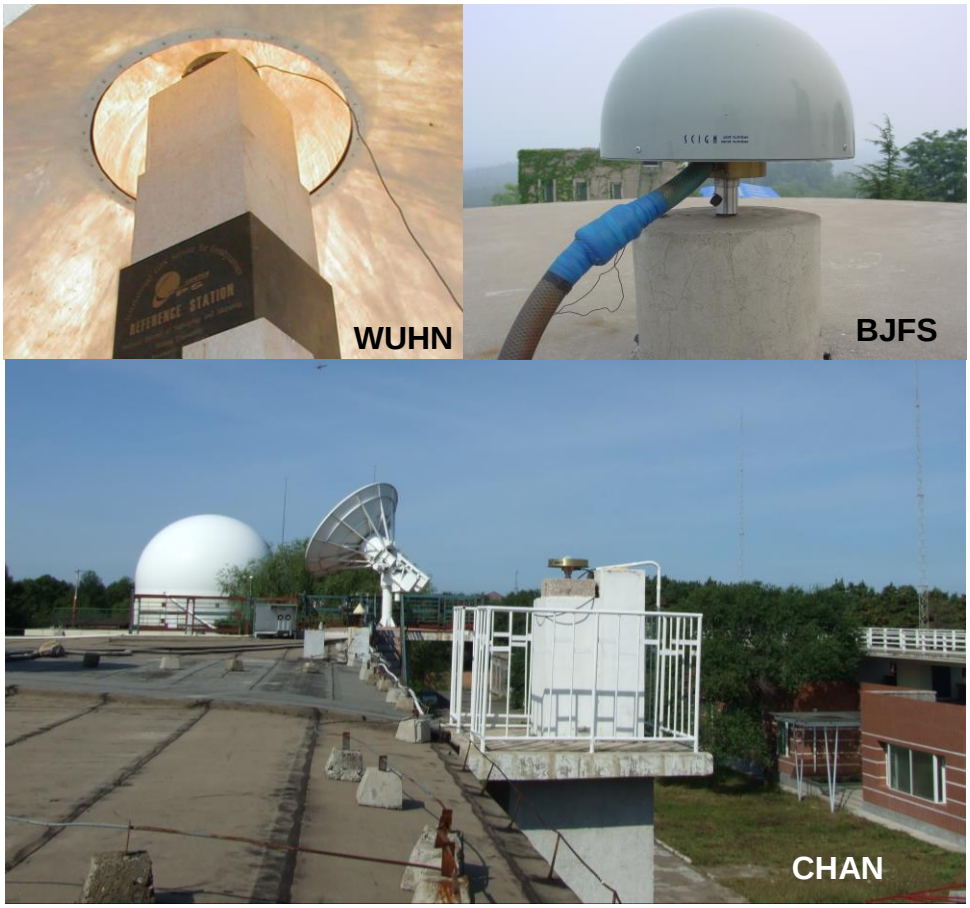

Figure 3-4 Photos of three reference stations: WUHN, BJFS, and CHAN (Source: www.unavco.org/data/gps-gnss)

Although most stations have collected data for over 14 years, not all the available data were used to established the SEChinaRF. For example, most stations in northeast China were affected by the 2011 Tohoku-Oki earthquake in Japan, so there would be a discontinuity of the horizontal time series on March 11, 2011, when the earthquake occurred. The horizontal displacement time series of four GPS stations, KHAJ, CHAN, BJFS, and WUHN shifted by 8-21 mm during the earthquake. So the data collected after the March of 2011 were not used for the establishment of the SEChinaRF. However, station HKOH is located over 3000 km awayfrom the earthquake epicenter, and no significantly co-seismic displacement induced by the earthquake was found at HKOH. Therefore, the data after March of 2011 recorded at HKOH were still used.

Figure 3-4 shows the displacement time series of the X, Y, and Z coordinates for the five reference stations within the Earth-Centered Earth-Fixed (ECEF) Cartesian coordinate system referred to IGS08. It also presents the data span used to establish the SEChinaRF. First, all reference stations had data histories of longer than 7 years. Second, no considerable subsidence was observed in these five reference stations. Third, no stations had data-discontinuities longer than seven months (HKOH, 07/2011-02/2012; KHAJ, 03/2004-09/2004), and there were no velocity discontinuities.

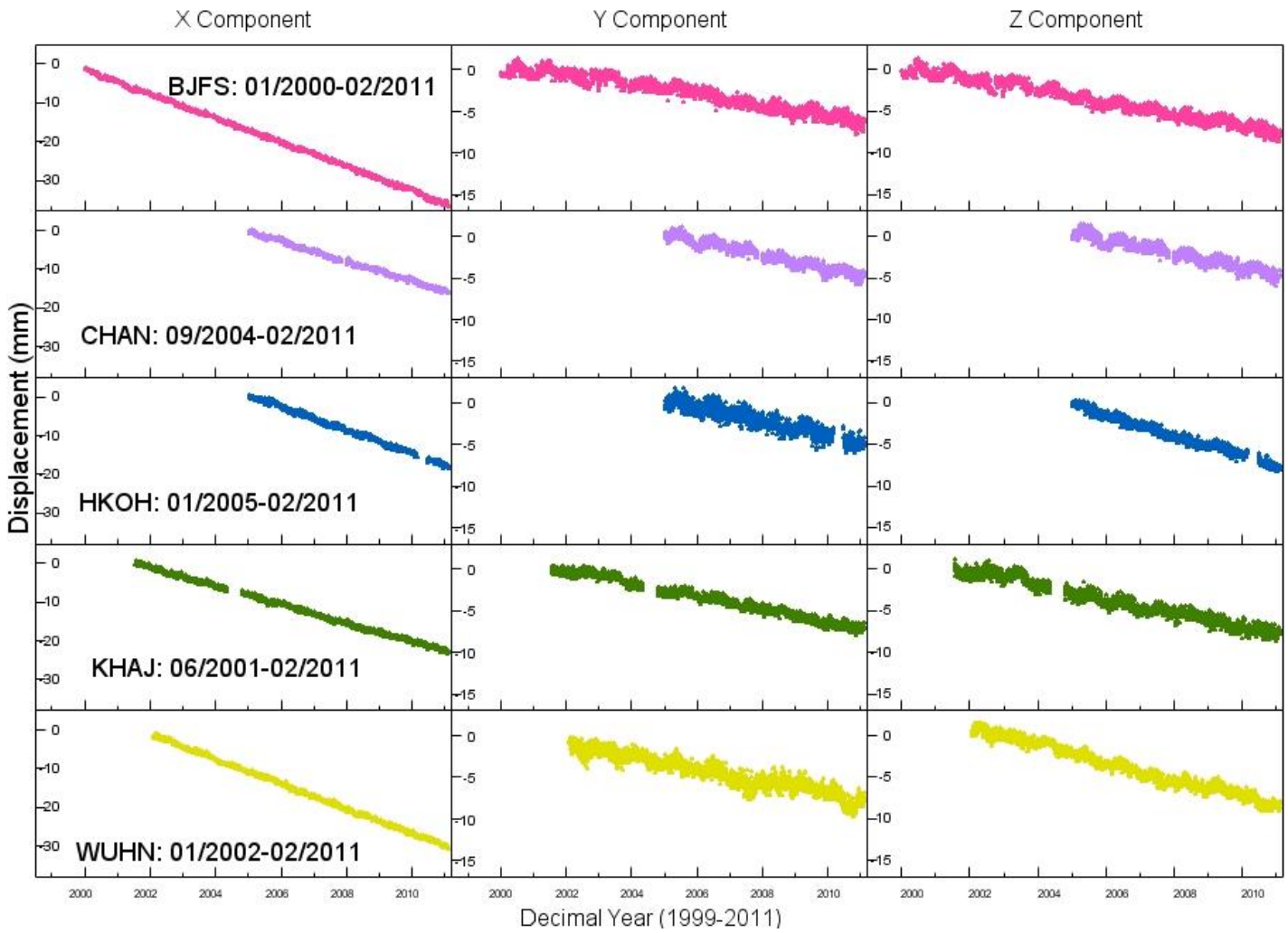

Figure 3-5 Earth-Center Earth-Fixed (ECEF) Cartesian coordinates (X, Y, Z) of five reference stations within IGS08. The data of all the stations after February of 2011 were not used, because their discontinuity induced by the 2011 Tohoku-Oki earthquake.

3.3 Realization of the East China Reference Frame

3.3.1 Helmert transformation

Helmert transformation was applied to convert positional coordinates from IGS08 to SEChinaRF. The transformation of GPS coordinates was performed using a daily 14-parameter similarity transformation, which includes 3 translations, 3 rotations, 1 scale, and their rates. The coordinates of a station within SEChinaRF can be calculated by the following equations:

$$X(t)_{SEChinaRF} = T_X(t) + [1+s(t)] \cdot X(t)_{IGS08} + R_Z(t) \cdot Y(t)_{IGS08} - R_Y(t) \cdot Z(t)_{IGS08}$$

$$Y(t)_{SEChinaRF} = T_Y(t) - R_Z(t) \cdot X(t)_{IGS08} + [1+s(t)] \cdot Y(t)_{IGS08} + R_X(t) \cdot Z(t)_{IGS08}$$

$$Z(t)_{SEChinaRF} = T_Z(t) + R_Y(t) \cdot X(t)_{IGS08} - R_X(t) \cdot Y(t)_{IGS08} + [1 + s(t)] \cdot Z(t)_{IGS08}$$

From the equations, T_X (t), T_Y (t), and T_Z (t) are translations along the X-, Y-, and Z- axis; R_X (t), R_Y (t), and R_Z (t) are counterclockwise rotations around these three axes; and s(t) is a differential scale factor between IGS08 and SEChinaRF.

3.3.2 Calculating 14 transformation parameters

Helmert transformation parameters can be calculated using a set of individual points with known coordinates in reference systems before and after the transformation. At least two points and one coordinate from a third point must be known to determine a total of seven parameters. Thus, a system of linear equations with seven equations and seven unknowns is formed and can be solved.

Table 3-2 lists the averaged XYZ coordinates of these five reference stations at epoch 2013.0 and the velocities along the X, Y, and Z axes within IGS08. The XYZ coordinates listed in Table 3-2 were calculated using the following equation:

$$\bar{X}\,(2013) = \sum_{i=1}^{n} (X\,(i) + (2013.0 - t\,(i)) \times V)/n.$$

Here, X (i) represents the coordinate time series of one component in IGS08; t (i) represents epochs; n is the number of total samples; and V is the velocity. Since the two frames are aligned at epoch 2013.0, X (2013) can be regarded as the coordinates in both frames at epoch 2013.0:

$$X_{IGS08}\,(2013) = \bar{X}\,(2013) = X_{SEChinaRF}\,(2013)$$

The coordinates of these reference stations in both IGS08 and SEChinaRF can be modeled using a linear regression. The velocities in SEChinaRF can be regarded as zeros since SEChinaRF is defined as a strictly stable frame. For example, the coordinates at epoch 2008.0 can be calculated using the following equations:

$$X_{IGS08}\,(2008) = X_{IGS08}\,(2013) + (2008.0 - 2013.0) \times V,$$

$$X_{SEChinaRF}\,(2008) = X_{SEChinaRF}\,(2013).$$

The coordinates of these five common points within both IGS08 and SEChinaRF are then available, so the seven parameters for the Helmert transformation at epochs 2013.0 can be calculated. The results are listed in Table

3-3. The rates of these Helmert parameters (T'_X, T'_Y, T'_Z, R'_X, R'_Y, R'_Z, and s') can be obtained using a simple differential method. For example:

$$T'_X = (T_X\ (2013) - T_X(2008))/5.0,$$

$$R'_X = (R_X\ (2013) - R_X(2008))/5.0,$$

$$s' = (s\ (2013) - s(2008))/5.0$$

Table 3-2 Earth-Centered Earth-Fixed Coordinates (XYZ, IGS08, Epoch: 2013.0) and velocities of five Frame Stations Derived from GIPSY PPP Solutions.

GIPSY PPP Solutions (IGS08, Epoch: 2013.0)							Velocity (mm/year)		
Station	X* (m)	Y* (m)	Z* (m)	RMS-X (cm)	RMS-Y (cm)	RMS-Z (cm)	V_X	V_y	V_z
WUHN	-2267749.647	5009154.241	3221290.624	0.303	0.653	0.443	-31.97	-7.39	-10.53
CHAN	-2674427.411	3757143.161	4391521.612	0.467	0.428	0.351	-25.73	-8.48	-8.49
HKOH	-2423817.295	5386056.951	2399883.227	0.392	0.668	0.455	-31.62	-9.47	-11.15
BJFS	-2148744.314	4426641.229	4044655.877	0.468	0.526	0.294	-31.20	-6.19	-7.19
KHAJ	-2995266.633	2990444.534	4755575.821	0.516	0.348	0.353	-23.97	-7.87	-8.49

*X,Y,Z are the average coordinates calculated using the equation:

$$\bar{X}\,(2013) = \sum_{i=1}^{n} (X\,(i) + (2013.0 - t\,(i)) \times V)/n.$$

Table 3-3 Fourteen Parameters for Helmert Reference Frame Transformation from IGS08 to SEChinaRF

Parameter	Unit	IGS08 to SEChinaRF t0=2013.0
Tx(t0)	m	0.0
Ty(t0)	m	0.0
Tz(t0)	m	0.0
Rx(t0)	radian	0.0
Ry(t0)	radian	0.0
Rz(t0)	radian	0.0
s(t0)	unit less	0.0
dTx	m/year	6.594790E-03
dTy	m/year	5.727830E-04
dTz	m/year	-5.397500E-03
dRx	radian/year	-1.793725E-09
dRy	radian/year	-7.142687E-09
dRz	radian/year	5.634794E-09
ds	1/year	0.0

*Counterclockwise rotations of axes (X, Y, Z) are positive.

The XYZ coordinates within SEChinaRF then were converted into longitude, latitude and height coordinates. Three-component time series and velocities of these five reference stations were investigated. Table 3-4 shows the comparison of the three component velocities of the five reference stations within IGS08 and SEChinaRF, as well as their standard deviations. It can be founded that horizontal velocities were smaller than 1.4 mm/year and vertical velocities were smaller than 0.9 mm/year. They are ignorable compare to velocities within IGS08. Figure 3-4 and 3-5 illustrate the three component geodetic time series of the five reference stations referred to IGS08 and SEChinaRF.

Table 3-4 Comparison of the three component velocities of the five reference stations within IGS08 and SEChinaRF

Station Id	Date duration	NS Velocity (IGS08, mm/yr)	NS Velocity (SEChinaRF, mm/yr)	Standard deviation of NS velocity mm/yr	EW Velocity (IGS08, mm/yr)	EW Velocity (SEChinaRF, mm/yr)	Standard deviation of EW velocity mm/yr	UD Velocity (IGS08, mm/yr)	UD Velocity (SEChinaRF, mm/yr)	Standard deviation of UD velocity mm/yr
CHAN	09/2004-02/2011	-11.68	1.38	0.023	25.88	-0.78	0.024	-0.02	-0.60	0.084
KHAJ	06/2001-02/2011	-14.16	-0.52	0.013	22.50	-0.71	0.012	1.19	0.06	0.042
BJFS	01/2000-02/2011	-10.67	1.28	0.011	30.77	1.44	0.011	1.57	0.81	0.036
HKOH	01/2005-02/2011	-12.21	-0.48	0.019	32.76	0.73	0.025	-0.31	0.67	0.044
WUHN	01/2002-02/2011	-12.35	-0.13	0.013	32.17	0.91	0.016	0.15	0.25	0.055

The 2011 Tohoku earthquake had a significant influence to the time series of these five stations, therefore, the data used to define the SEChinaRF were cut off after the earthquake.

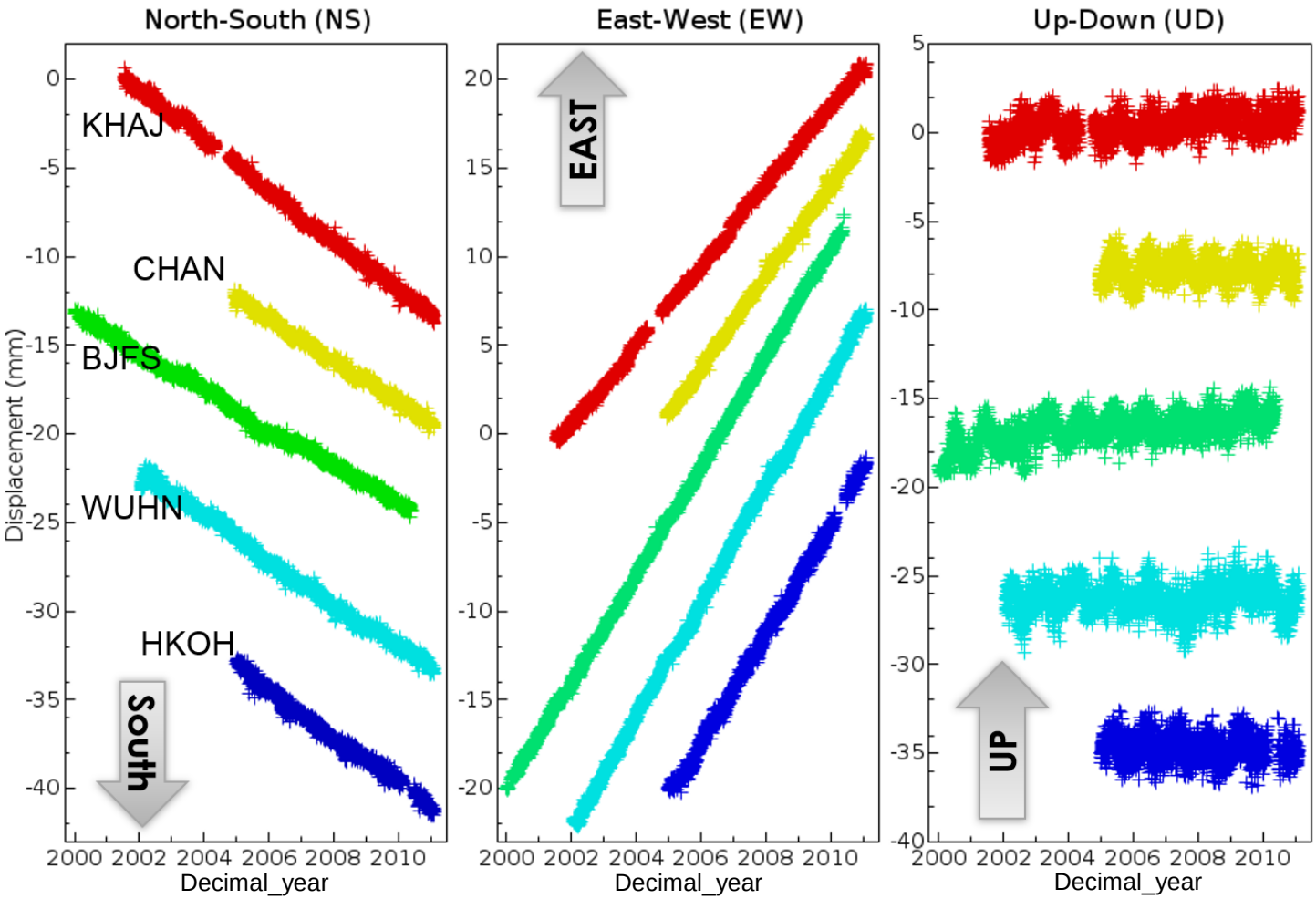

Figure 3-6 Three component geodetic time series (12/1999-02/2011) of the five reference stations referred to IGS08

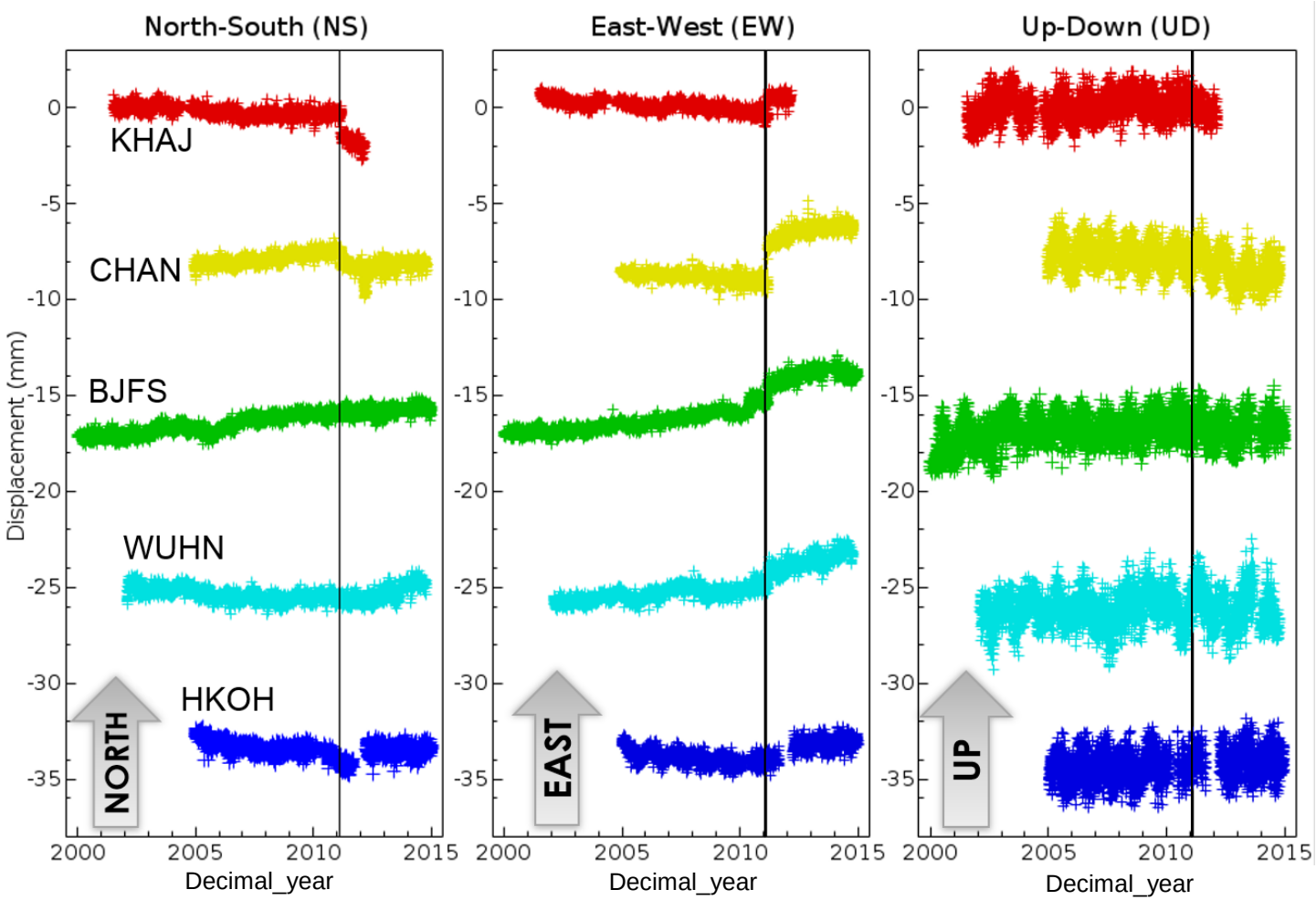

Figure 3-7 Three component geodetic time series of the five reference stations referred to SEChinaRF. The black vertical line represent the date of the 2011 Tohoku-Oki earthquake.

3.4 Products derived from SEChinaRF

3.4.1 Examples of the three-component displacement time series

The three components represent three geodetic directions: north to south (NS), east to west (EW), and up to down (UD). Comparing three-component displacement time series in two different reference frames allows for an in-depth evaluation of the selected reference frames. In IGS08, the horizontal velocities are about 10 mm/year along the NS direction and 30 mm/year along the EW direction. As shown in Table 3-4, the velocities of all three components in SEChinaRF are less than 1.4 mm/year, which is under the velocity resolution that can be distinguished by the current local reference frame. The near-zero velocities of the reference stations in SEChinaRF indicate that all five sites were stable over the past 9 years (2002-2011) for WHUN, 11 years (2000-2011) for BJFS, 7 years (2004-2011) for CHAN, 9 years (2005-2014) for HKOH, and 10 years (2001-2011) for KHAJ. These figures also indicate that the vertical coordinates within IGS08 and SEChinaRF are approximately identical. Figures 3-5~3-9 present the full time-span three-component displacement time series for the five reference stations, referred to both IGS08 and SEChinaRF. Though these full-time-span time-series clearly explained the reason why only certain portion of the whole data span were selected for the establishment of SEChinaRF. For example, in Figure 3-5, we can evidently observe that shift of both the NS and EW displacement time series induced by the 2011 March 11 earthquake in Japan. And Figure 3-7 shows that there were no considerable impact on station HKOH by the earthquake. The co-

and post-seismic displacement associated with the 2011 earthquake will be further discussed in chapter 6.

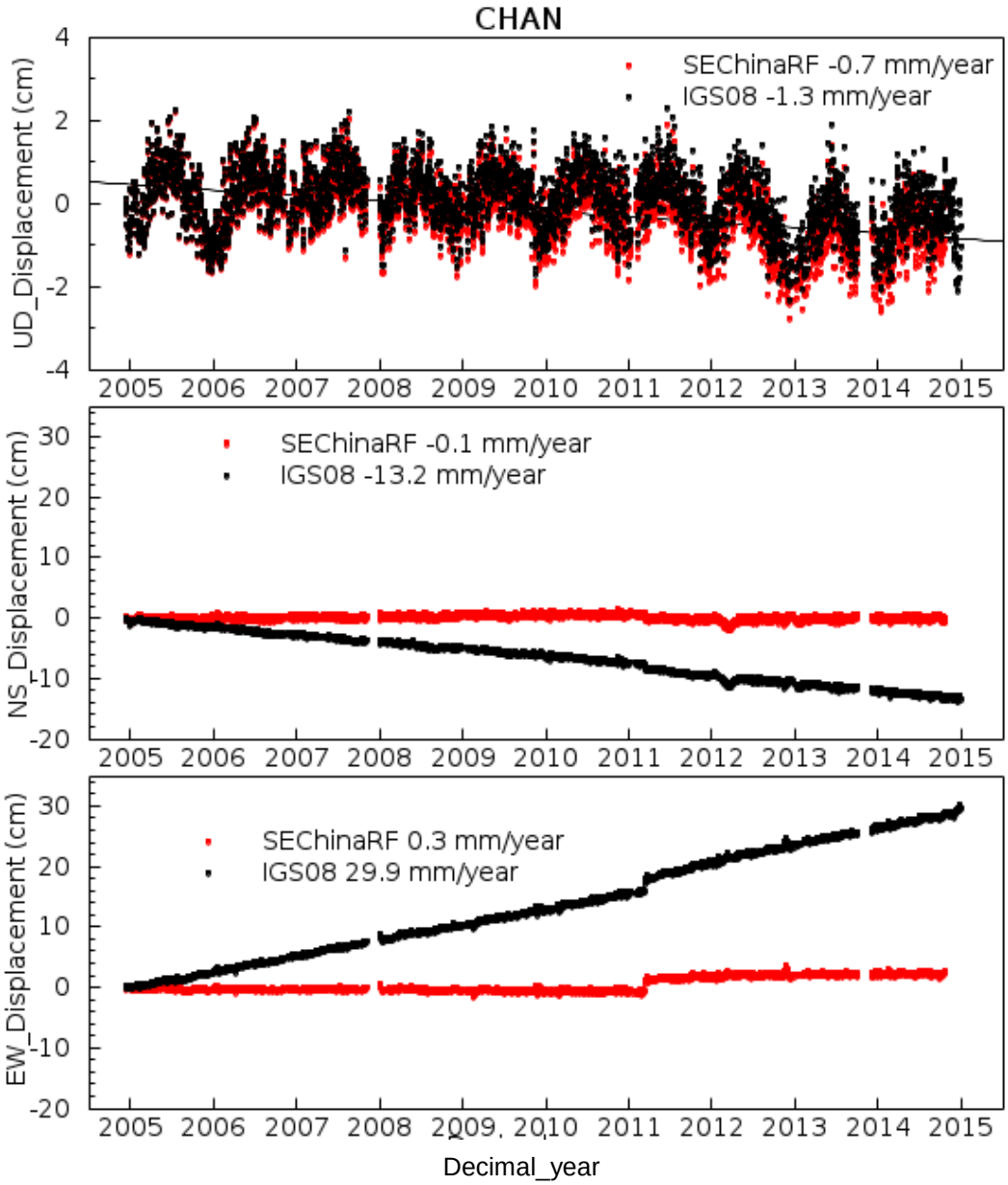

Figure 3-8 Displacement time series at frame site CHAN (2005-2015) referred to two reference frames: IGS08 (global, red) and SEChinaRF (local, black). The horizontal step in early 2011 was caused by the 2011 Tohoku-Oki earthquake (M_W 9.0) in Japan.

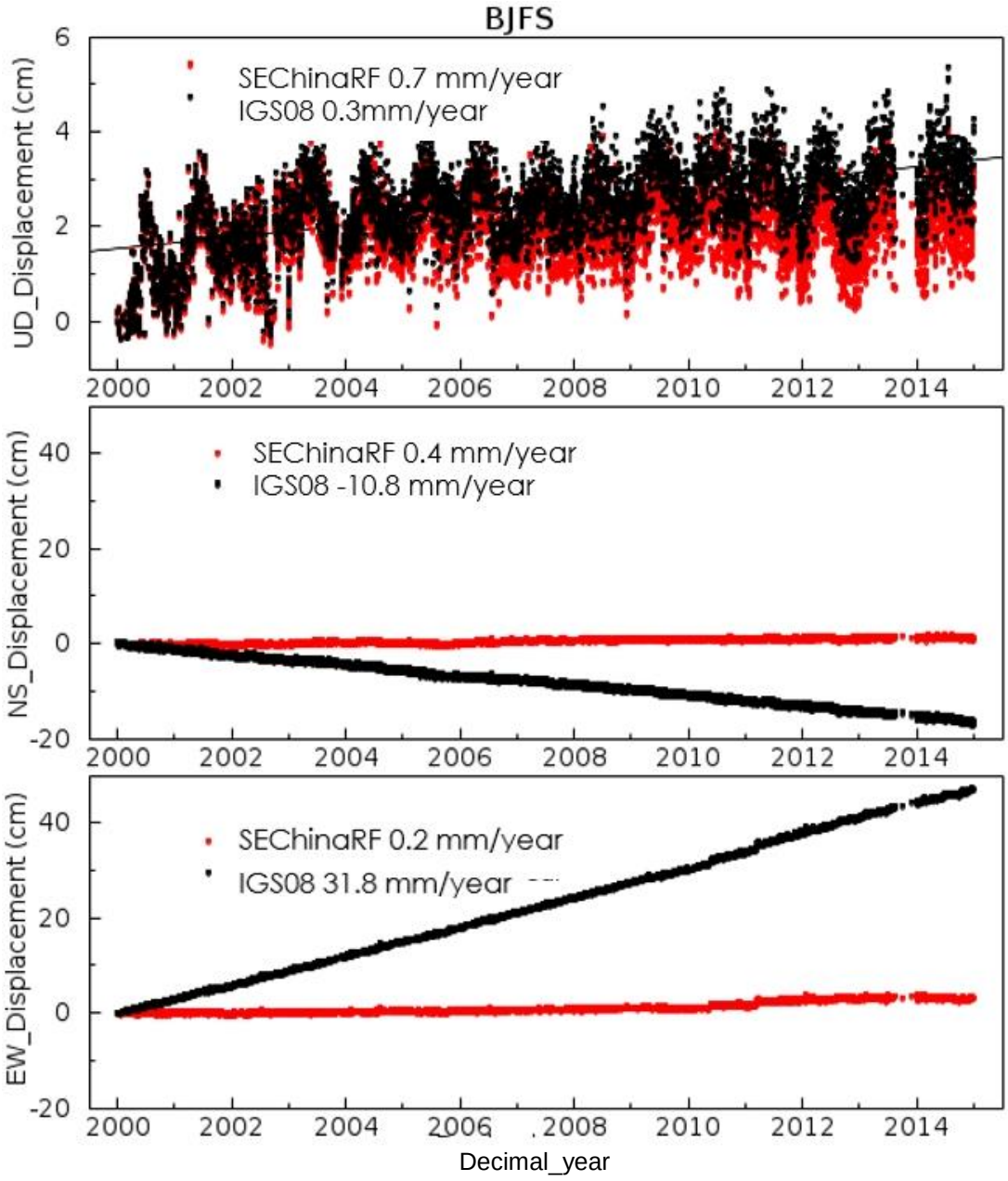

Figure 3-9 Displacement time series at frame site BJFS (1999-2015) referred to two reference frames: IGS08 (global, red) and SEChinaRF (local, black). The horizontal step in early 2011 was caused by the 2011 Tohoku-Oki earthquake (M_W 9.0) in Japan.

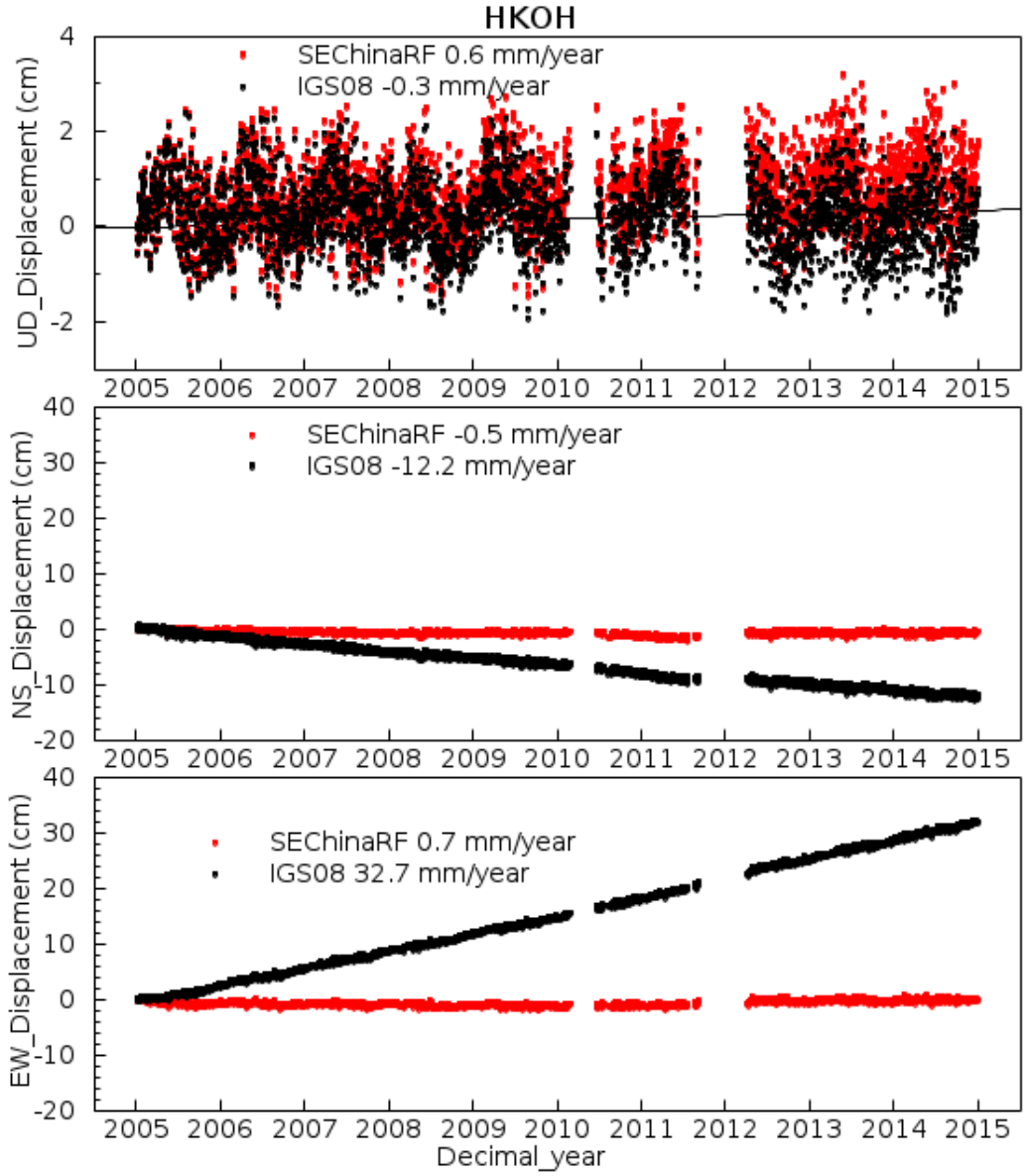

Figure 3-10 Displacement time series at frame site HKOH (2005-2014) referred to two reference frames: IGS08 (global, red) and SEChinaRF (local, black).

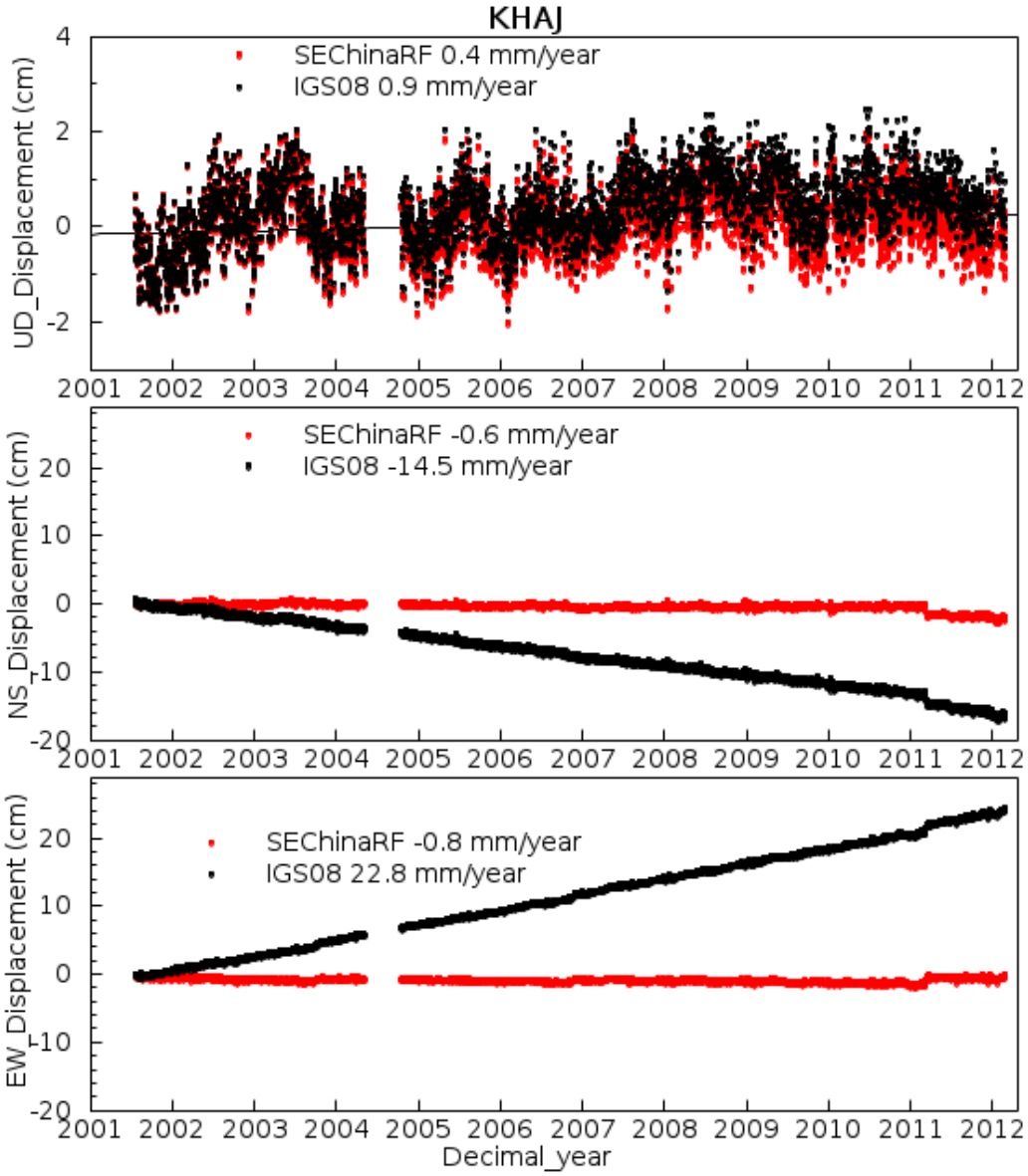

Figure 3-11 Displacement time series at frame site KHAJ (2001-2014) referred to two reference frames: IGS08 (global, red) and SEChinaRF (local, black). The horizontal step in early 2011 was caused by the 2011 Tohoku-Oki earthquake (M_W 9.0) in Japan.

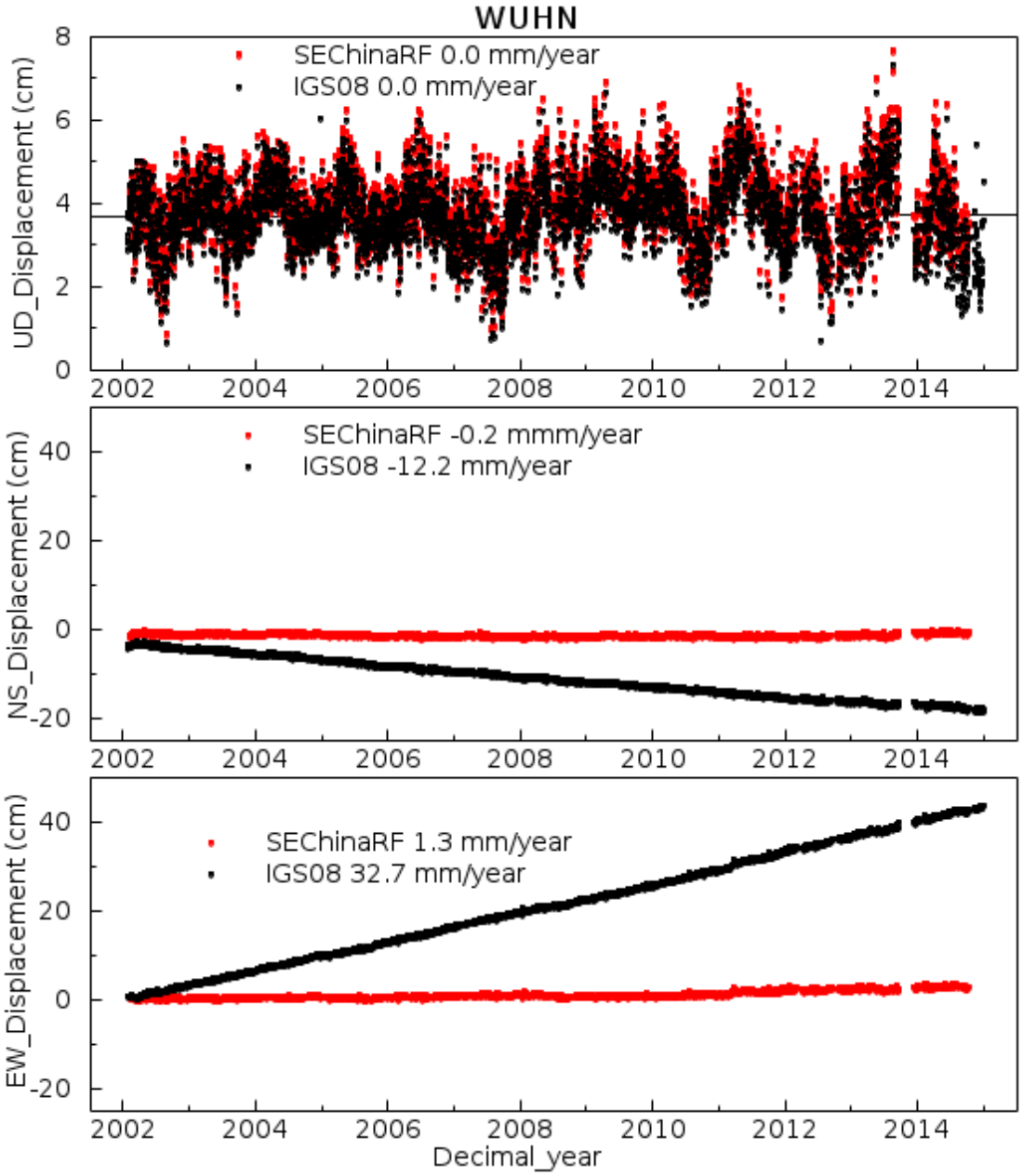

Figure 3-12 Displacement time series at frame site WUHN (1996-2014) referred to two reference frames: IGS08 (global, red) and SEChinaRF (local, black).

Table 3-5 lists the root-mean-square (RMS) of the displacement time series for the five reference stations in SEChinaRF. RMS is often used to assess the precision of GPS measurements. RMS accuracy is the degree of closeness of an observed value to its true value. The average RMS accuracy of these five stable stations within SEChinaRF is about 2.81 mm in the horizontal directions and 7.09mm m in the vertical direction.

Table 3-5 Geodetic coordinates (longitude, latitude, ellipsoidal height) of five reference stations and the repeatability (RMS) of PPP solutions within the SEChinaRF

Geodetic Coordinates (SEChinaRF)				RMS Accuracy		
Station	Latitude(°)	Longitude(°)	Height (m)	NS (mm)	EW (mm)	UD (mm)
WUHN	30.5316	-245.6427	25.81	2.34	2.25	7.90
KHAJ	48.5214	-224.9538	130.47	2.10	1.85	6.58
BJFS	39.6086	-244.1075	87.44	2.14	2.10	6.89
CHAN	43.7907	-234.5558	271.26	1.83	1.89	6.78
HKOH	22.2476	-245.7714	166.37	7.54	4.04	7.28
Average				3.19	2.43	7.09

3.4.2 Horizontal and vertical velocity fields of east China

Figure 3-10 and Figure 3-11 present the average horizontal and vertical displacement velocity fields derived from GPS observations (2010–2014) along the east coast of China, referred to both IGS08 and SEChinaRF. The vertical displacement velocity vectors are relative to the mass center of the earth. These velocity vectors indicated that both horizontal and vertical ground motions were site specific. Comparing GPS results in the two different reference frames allows for an in depth analysis of motion at varying scales. In Figure 3-10, horizontal velocity vectors in IGS08 indicated a common movement direction towards the southeast, which could be easily misinterpreted as consistent local ground displacements. Using the local reference frame would avoid this type of mistake. Figure 3-10 shows that the local horizontal movements have a common direction towards northeast with a velocity of approximately 4 mm/year. This indicated that the horizontal resolution of SEChinaRF is about 4 mm/year. It is acceptable considering SEChinaRF was established with only five reference stations, and it covers a large amount of coastal region of east China.

Figure 3-11 shows the vertical velocity vectors of permanent GPS stations alone the east coastal region of China. Substantial land subsidence in several coastal cities, such as Tianjin, Shandong and Guangdong could be observed from this figure. Land subsidence of east China's coastal cities will be further investigated in Chapter 4 and Chapter 5.

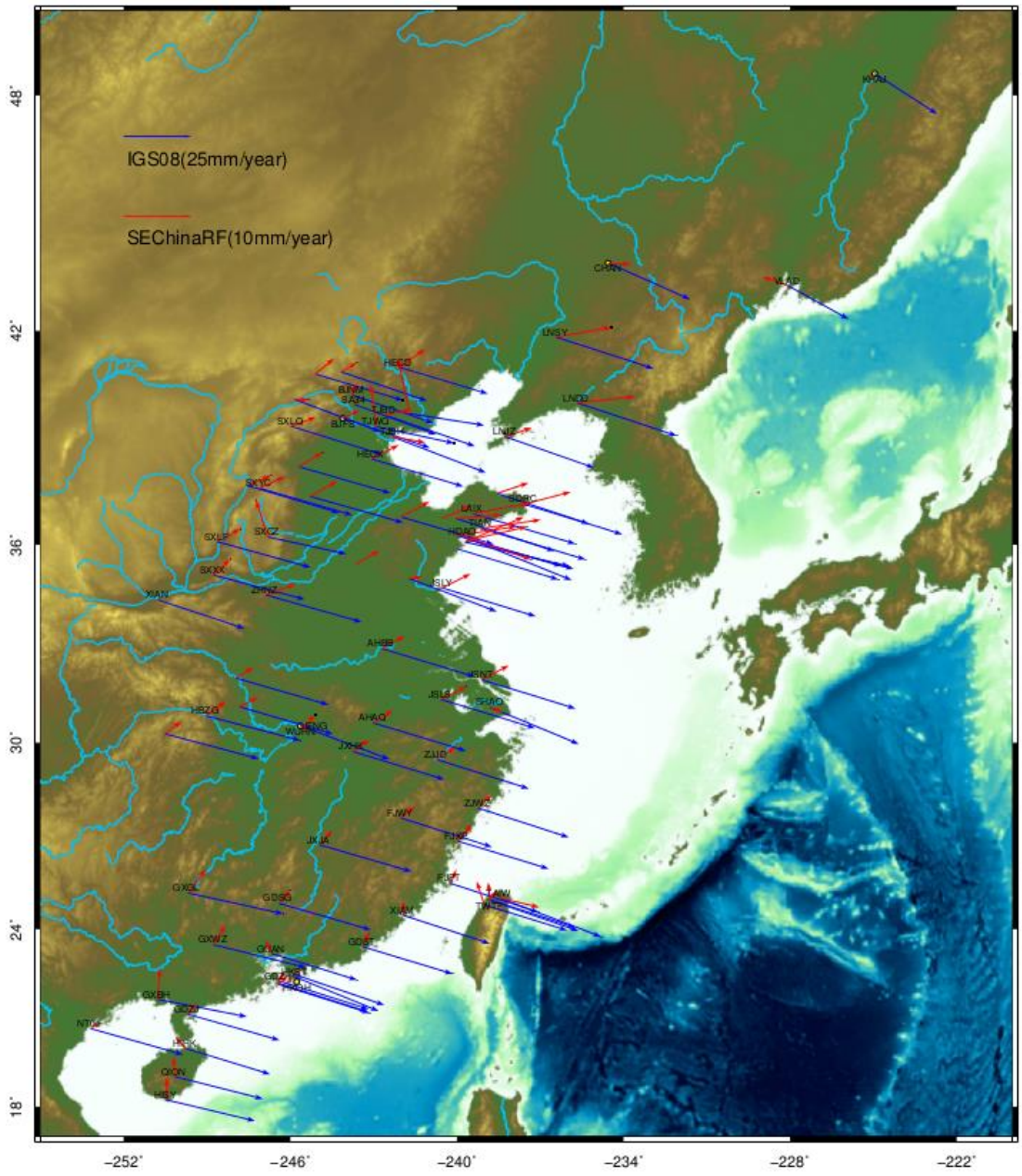

Figure 3-13 Horizontal velocity vectors of permanent GPS stations in east China. The blue arrows represent the average horizontal velocities of GPS stations during the past four years (2010-2014) referred to IGS08. The red arrows represent the average horizontal velocities of GPS stations during the past four years (2010-2014) referred to SEChinaRF.

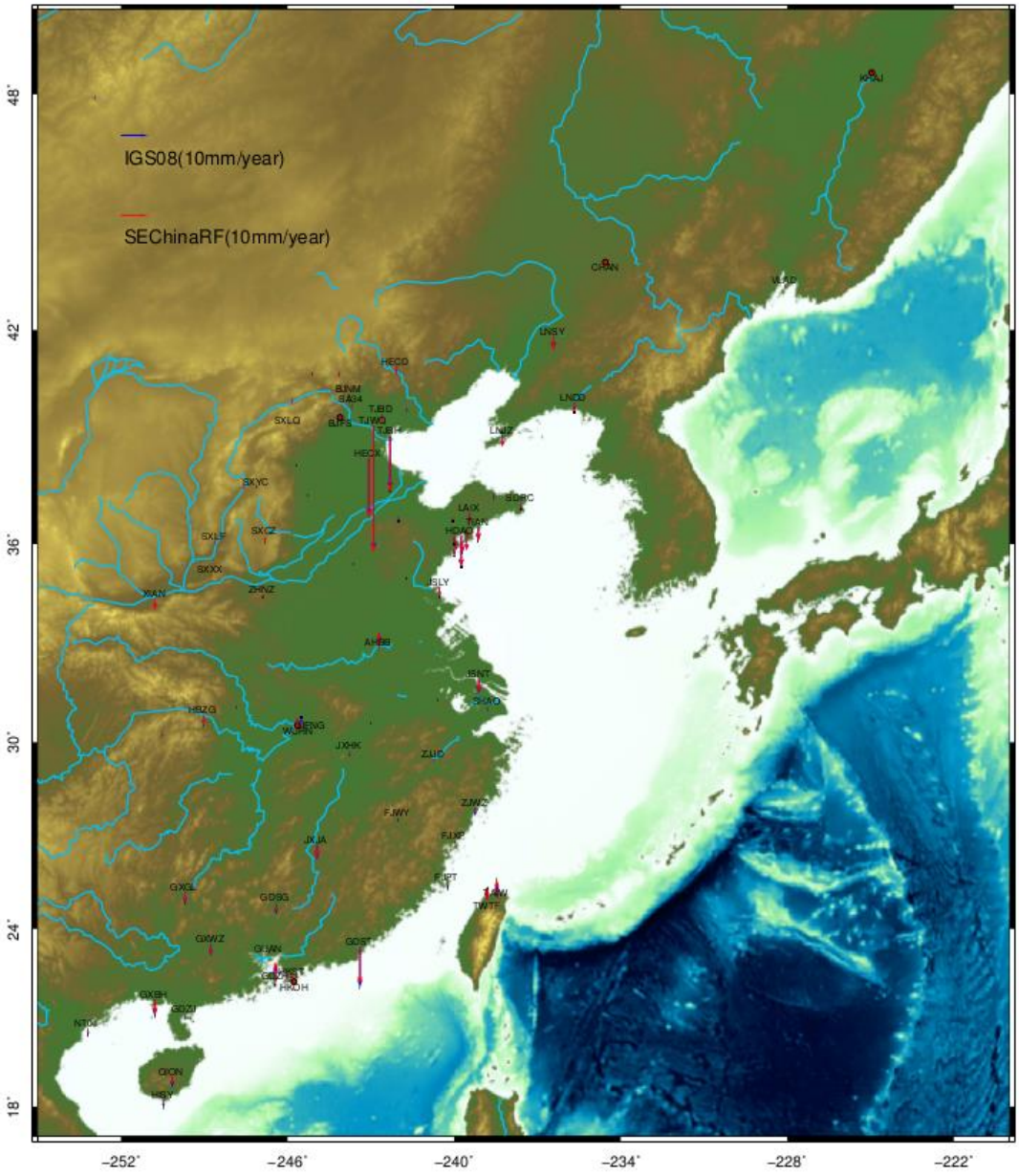

Figure 3-14 Vertical velocity vectors of permanent GPS stations in east China. The blue arrows represent the average vertical velocities of GPS stations during the past four years (2010-2014) referred to IGS08. The red arrows represent the average vertical velocities of GPS stations during the past four years (2010-2014) referred to SEChinaRF.

Chapter 4 Land Subsidence in Tianjin

4.1 Introduction: Sinking cities

Land subsidence is an environmental geological phenomenon that causes a downward shift of ground-surface relative to a datum, such as the sea-level. In many coastal and delta cities (e.g., Jakarta, Ho Chi Minh City, Bangkok), the land subsidence rate is much faster than the absolute sea level rising rate. (Erkens et al., 2014). Table 4-1 presents a recent subsidence study of 6 coastal megacities (Kaneko and Toyota, 2011; Erkens et al., 2014). In additional, in Shanghai, China, the mean cumulative subsidence in urban areas was 1.97 m from 1921-2009, and the average subsidence rate from 1996 to 2009 was 12.09 mm/year (Xu et al., 2012). Land subsidence in these coastal megacities develops slowly, resulting no evident damage in a short time. However, the economic loss over a long time is shocking. It can induce serious problems such as the damage of building and infrastructures, and the increase in flooding risk and sea water intrusion in coastal zones (Hu et al. 2009).

Subsidence can be caused by multiple driving factors, such as the dissolution of limestone, mining, extraction of underground fluid and natural gas, earthquakes, and tectonic movements. Land subsidence in coastal areas is most often caused by human activities, mainly from the removal of subsurface water. Considering that water is partly responsible for holding the ground up, a large amount of groundwater withdrawal from certain types of rocks, such as fine-grained sediments, will cause the rocks to collapse. Furthermore, excessive

groundwater pumping will result in the compaction of soils in some aquifer systems. This not only causes permanent land subsidence, but it also results in a permanent reduction in the total storage capacity of the aquifer system, because the compaction of the subsoil may reduce the size and number of the open pore spaces in the soil that previously held water. Therefore, the monitoring of land subsidence in coastal areas is critical for both economic development and the protection of the subsurface environment.

Table 4-1 Subsidence in sinking cities

City	Mean cumulative subsidence in period 1900-2013 (mm)	Mean current subsidence rate (mm/year)	Maximum subsidence rate (mm/year)	Estimated additional mean cumulative subsidence until 2025 (mm)
Jakarta*	2000	75-100	179	1800
Ho Chi Minh City*	300	Up to 80	80	200
Bangkok*	1250	20-30	120	190
New Orleans*	1130	6	26	>200
Tokyo**	4250	Around 0	239	0
West Netherlands*	275	2-10	>17	70

Sources: * Erkens et al., 2014; Kaneko and Toyota, 2011.

4.2 Land subsidence in Tianjin, China

In China, land subsidence is currently a major issue for a large number of provinces and cities in the eastern and middle regions of the country, including Shanghai, Tianjin, Jiangsu, and the Hebei provinces; the total subsidence area is more than 7.9×10^4 km^2 (Hu et al., 2004). Tianjin is a metropolis in northern China with a population of about 13 million people inhabiting an area of about 11,760 km^2. It is the largest coastal city in northern China and the cradle of industrial modernization in China. Tianjin borders the Hebei province and the Beijing municipality in the north and the Bohai Gulf portion of the Yellow Sea in the east. In the process of urbanization, Tianjin has experienced extensive groundwater withdrawal for water resources, and this has induced disasters, such as land subsidence and groundwater quality deterioration. Currently, Tianjin is the city with the most serious land subsidence issues in China.

For the past 50 years, Tianjin has suffered dramatically from land subsidence. The maximum cumulative subsidence reached 3.22 m, and the total affected area was nearly 8,000 km^2. The subsidence reached its most critical state in the early 1980s when it occurred at a rate as high as 110 mm/year. At the same time, groundwater extraction had also reached a maximum of 1,200 million m^3 (Yi et al., 2011). The government of Tianjin began to control the groundwater withdrawal to reduce the severe land subsidence since 1985. By importing the Luan River to Tianjin, the subsidence rate in urban areas dropped to 10–15 mm/year; however, considering that Tianjin is one of the most rapidly developing areas in China and lies within the East Asia monsoon region, it is always short of surface and groundwater resources. As a result of rapid economic development

and population growth, the groundwater in the Tianjin coastal area has been intensively exploited during the past decades, and, consequently, the rate of land subsidence in the Tianjin coastal area has been increasing since 2001 (Figure 4-1). In 2010, with a subsidence rate of 30–40 mm/year, several new suburban subsidence centers were formed (Yi et al., 2011).The significant land subsidence along with the rise in the sea level may seriously damage the economy as well as society.

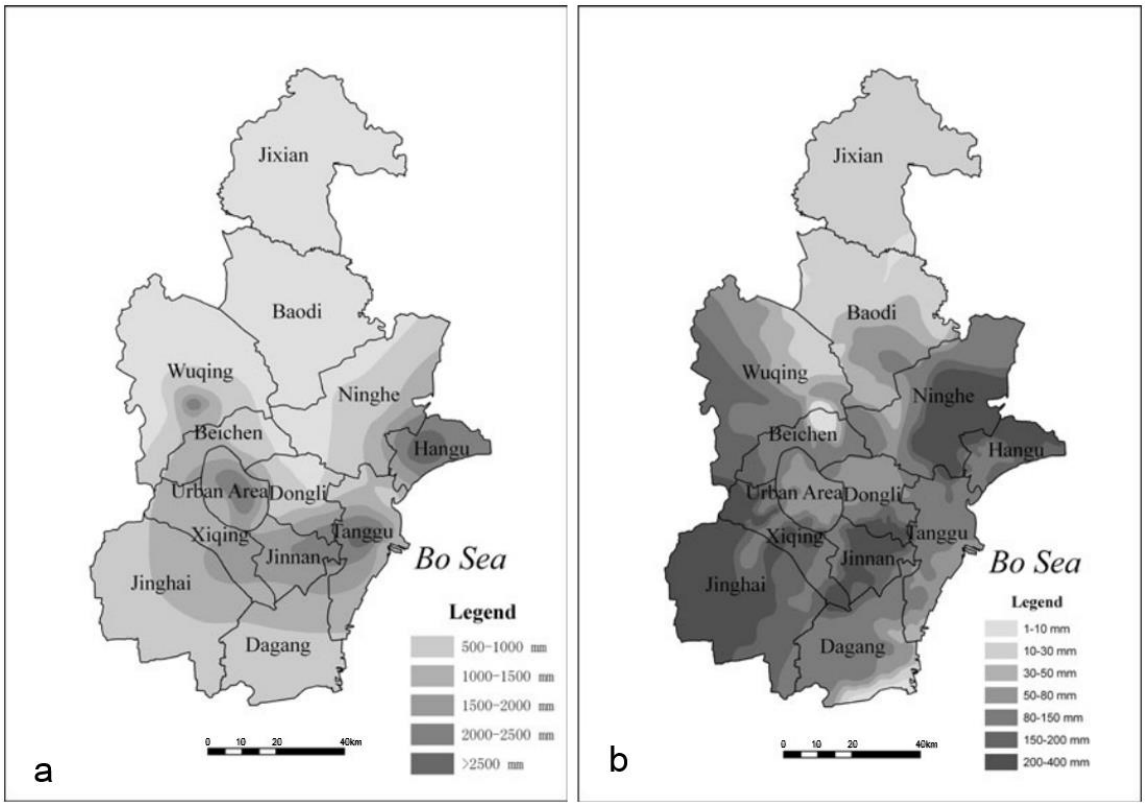

Figure 4-1 a) Map of the cumulative land subsidence (mm) in the Tianjin metropolitan area from 1967 to 2000; b) Map of cumulative land subsidence (mm) in the Tianjin metropolitan area from 2001 to 2007 (Yi et al., 2011)

4.3 GPS-based monitoring of land subsidence in the Tianjin area

In the past two decades, Global Positioning System (GPS) technologies have been frequently applied to urban subsidence studies both as a complement

and an alternative to conventional surveying methods. A large number of permanent continuously operating GPS stations have been installed in China over the past five years. The GPS data from four stations of the CMONOC in the Tianjin area are thoroughly discussed in this chapter. This study provides a well-developed example of the GPS-based monitoring of land subsidence with centimeter to millimeter accuracy.

The vertical displacement time series of three permanent GPS stations in

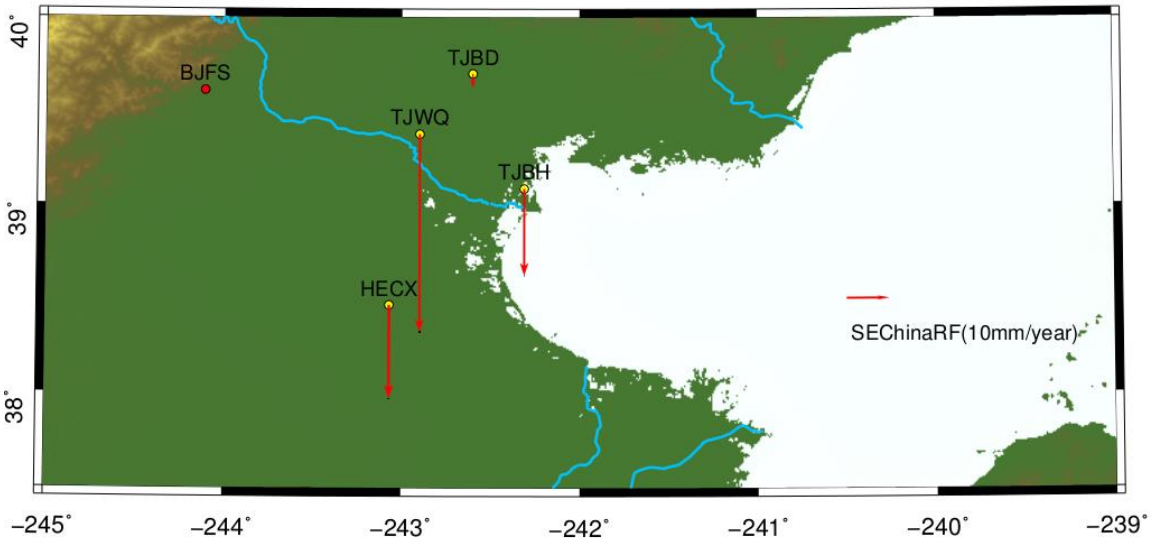

Figure 4-2 Map illustrating the locations of the four study GPS stations and the vertical velocity vectors in SEChinaRF.

Tianjin, TJBD (2010-2014), TJBH (2010-2014), and TJWQ (2010-2014), and one station in the Hebei province, HECX, are examined. Because HECX is only 104 km from downtown Tianjin, it can be used to investigate the land subsidence status of the great Tianjin area in this study. Figure 4-2 shows the locations of the four GPS stations in Tianjin area. The red arrow represents the vertical velocities of

these stations. They are derived from the GPS position time series referred to SEChinaRF, which are listed in Figure 4-3 ~ 4-6.

Table 4-2 shows the observation period, geographic information and subsidence rates of the four GPS stations in Tianjin area. It can be found that at station TJWQ, the subsidence rate was about 45 mm/year referred to SEChinaRF. It was considerably large and indicated that the subsidence in this region should be investigated and controlled. Meanwhile, the subsidence rates at TJBH and HECX were approximately 20 mm/year, which were smaller than the subsidence rate at TJWQ. However, they were also relatively large for coastal cities. And at station TJBD, the subsidence rate was 1.9 mm/year, which was acceptable.

Table 4-2 Geographical information and vertical velocities of the four GPS stations in Tianjin area

Station ID	Observation period	Longitude (°)	Latitude (°)	Subsidence rate (IGS08) (mm/yr)	Subsidence rate (SEChinaRF) (mm/yr)	Standard deviation (mm/yr)
TJBD	08/2010-09/2014	-242.6008	39.6975	-1.2	-1.9	0.12
TJBH	08/2010-09/2014	-242.3108	39.0837	-18.9	-19.4	0.12
TJWQ	08/2010-09/2014	-242.8970	39.3754	-44.9	-45.6	0.19
HECX	02/2010-08/2012	-243.0691	38.4648	-20.9	-21.4	0.13

TJBD is located in the Baodi district of Tianjin. This area is the least economically developed and has the smallest population compared to the other three areas. Over 80% of water usage in Baodi is for agriculture uses and only less than 15% is from groundwater. Consequently, the subsidence rate at TJBD is about 1.9mm/year (Figure 4-3).

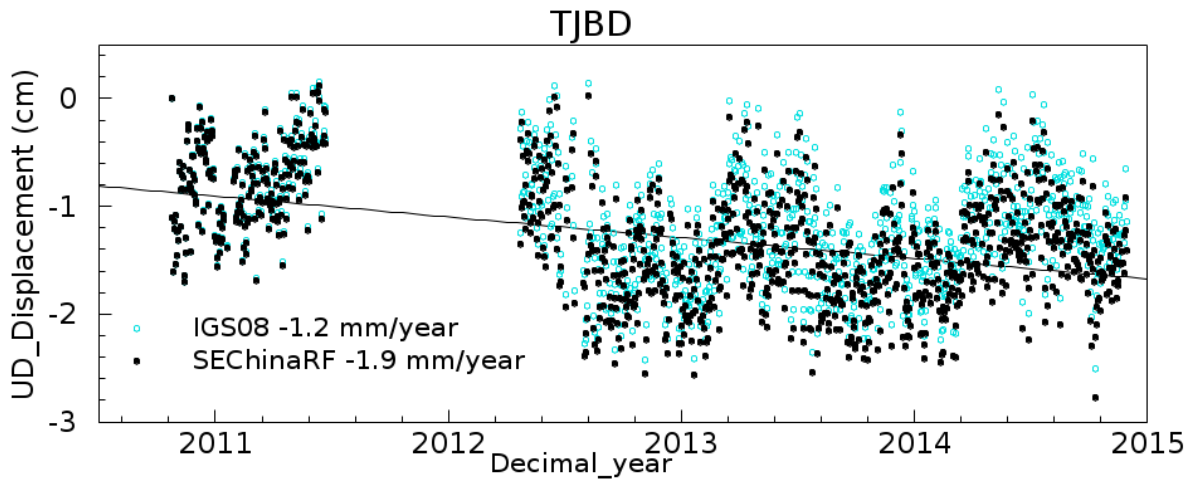

Figure 4-3 Vertical Displacement time series at TJBD (2010-2014) referred to IGS08 (global, cyan circle) and SEChinaRF (local, black point)

Tianjin Binhai New Area locates in the northeastern part of the North China Plain. It is one of the most rapidly developing areas in China. Because of the shortage of water resources, groundwater in the study area has been intensively exploited during the past decades to meet the demand of rapid economic development and population growth. Consequently, Tianjin Binhai New Area suffers the one of the most severe land subsidence in China. The accumulated land subsidence recorded by station TJBH has reached approximately 80 mm

during the past four years, and the subsidence rate is 19.4 mm/year, referred to SEChinaRF (Figure 4-4).

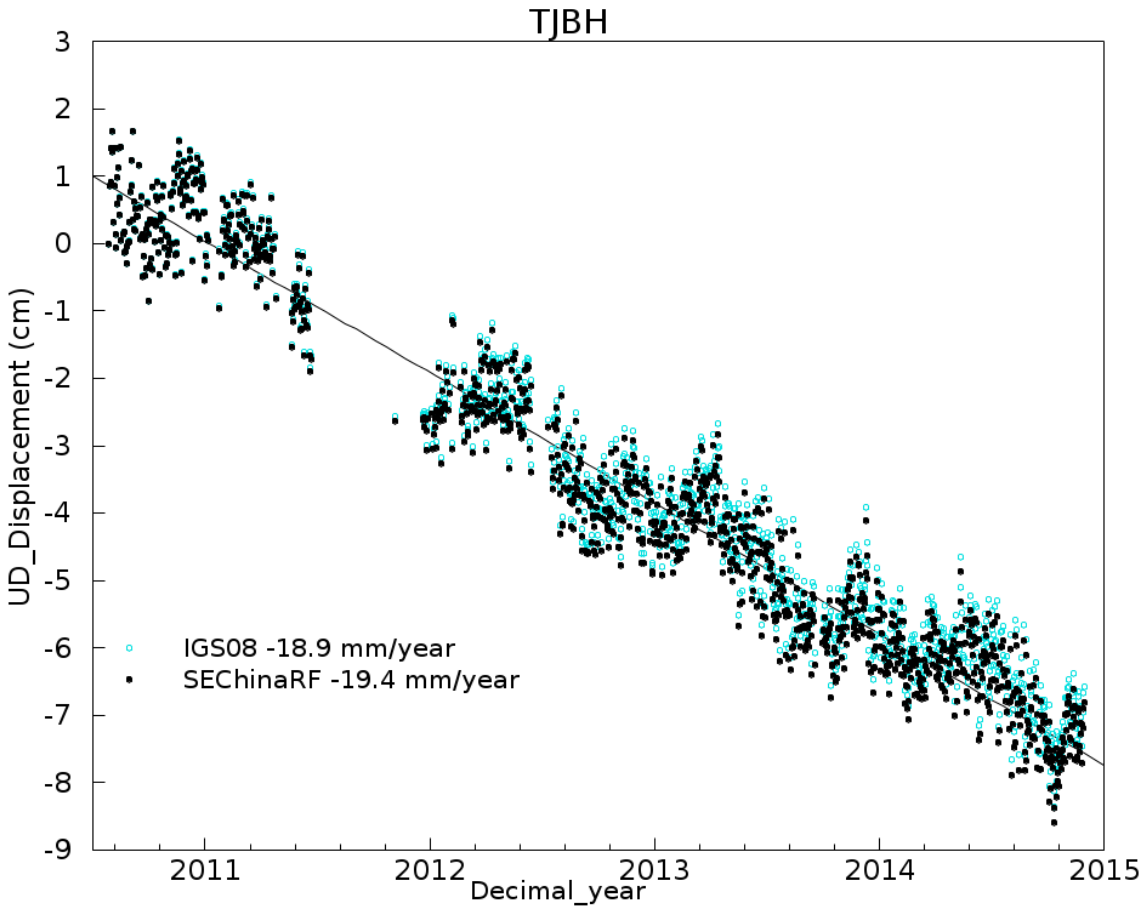

Figure 4-4 Vertical Displacement time series at TJBH (2010-2014) referred to IGS08 (global, cyan circle) and SEChinaRF (local, black point)

TJWQ is located in the Wuqing district, which has a unique location advantage called the “Corridor of Beijing and Tianjin” and has been experiencing major urbanization recently. The population in this district has reached 1,053,300, and the water usage reached 350 million cubic meters in 2012. Over 25% of water usage is from groundwater. TJWQ has had a rapid subsidence rate during the past

four years with an accumulated subsidence of approximately 170mm and a subsidence rate of 45.6 mm/year (Figure 4-5). This observation provides firm evidence that Wuqing is developing into new subsidence center in Tianjin.

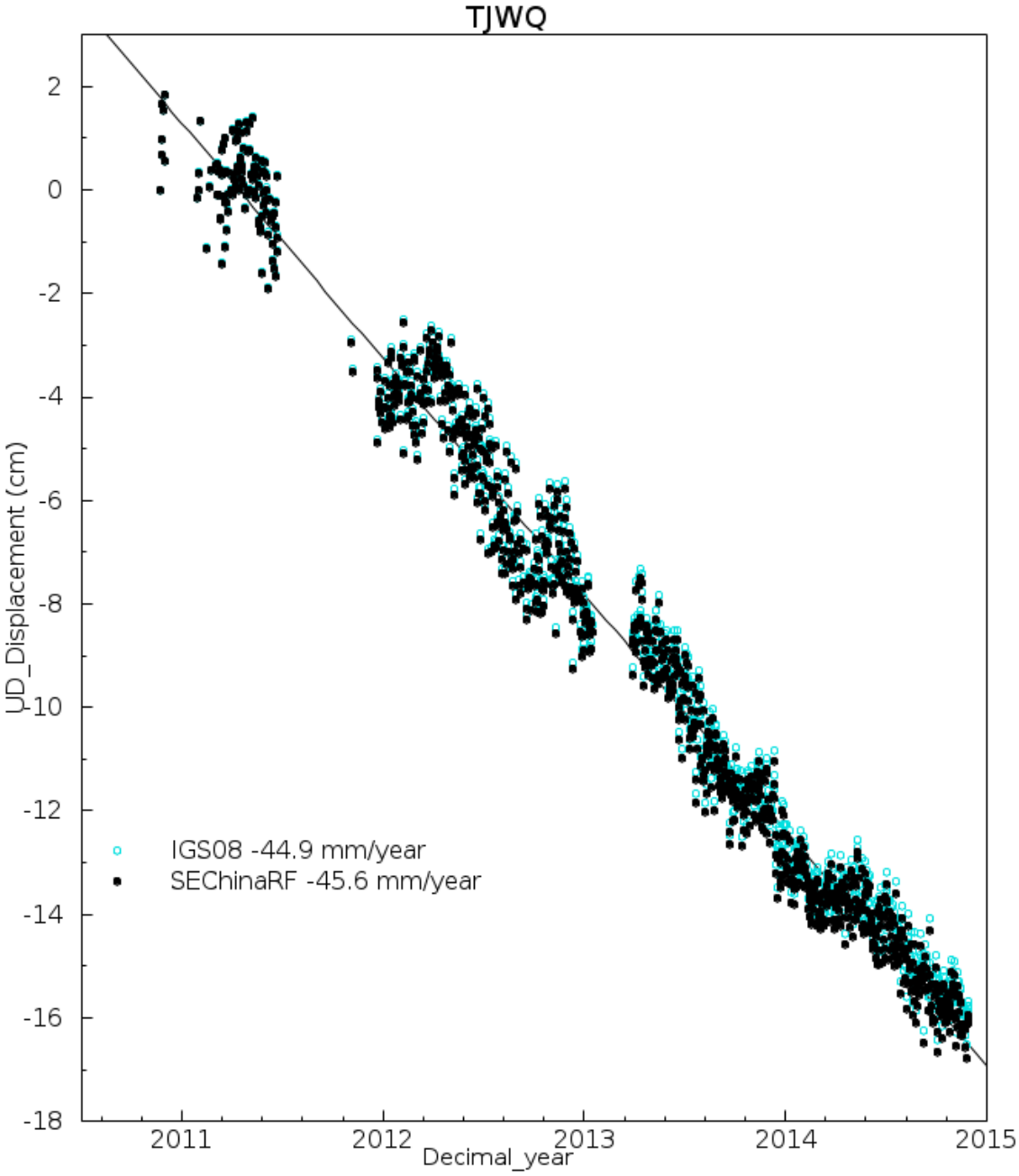

Figure 4-5 Vertical Displacement time series at TJWQ (2010-2014) referred to IGS08 (global, cyan circle) and SEChinaRF (local, black point)

HECX is located at Cangzhou, Hebei province. It is located approximately 90 km from the major port city of Tianjin and 100km from the coastline of Bohai Bay. Cangzhou is a major industrial city. The accumulated land subsidence at HECX has reached nearly 90 mm during the past four years, and the subsidence rate is 21.4 mm/year, referred to SEChinaRF (Figure 4-6).

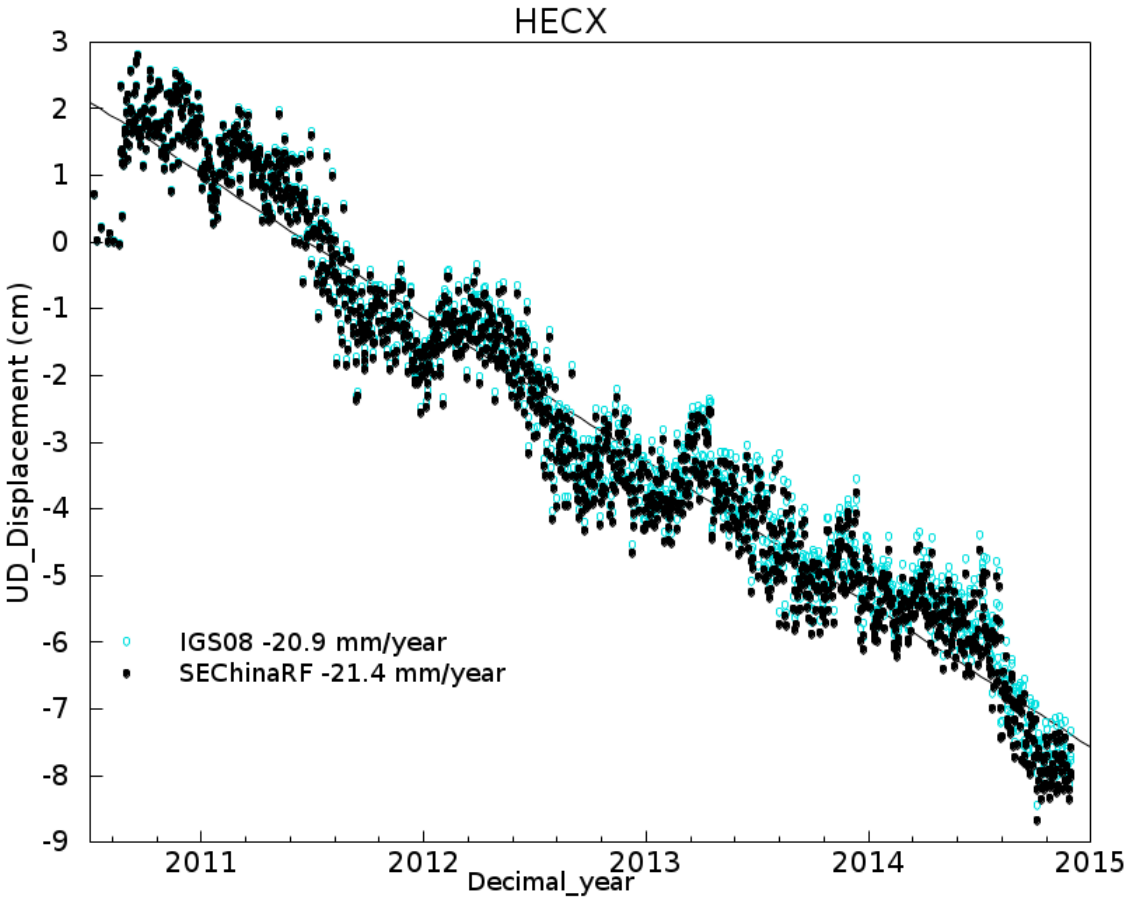

Figure 4-6 Vertical Displacement time series at HECX (2010-2014) referred to IGS08 (global, cyan circle) and SEChinaRF (local, black point)

Figure 4-7 demonstrates the comparison of the four-year vertical displacement time series at four stations: TJBD, HECX, TJBH, and TJWQ, referred to SEChinaRF. The subsidence rates are site-specific in this area.

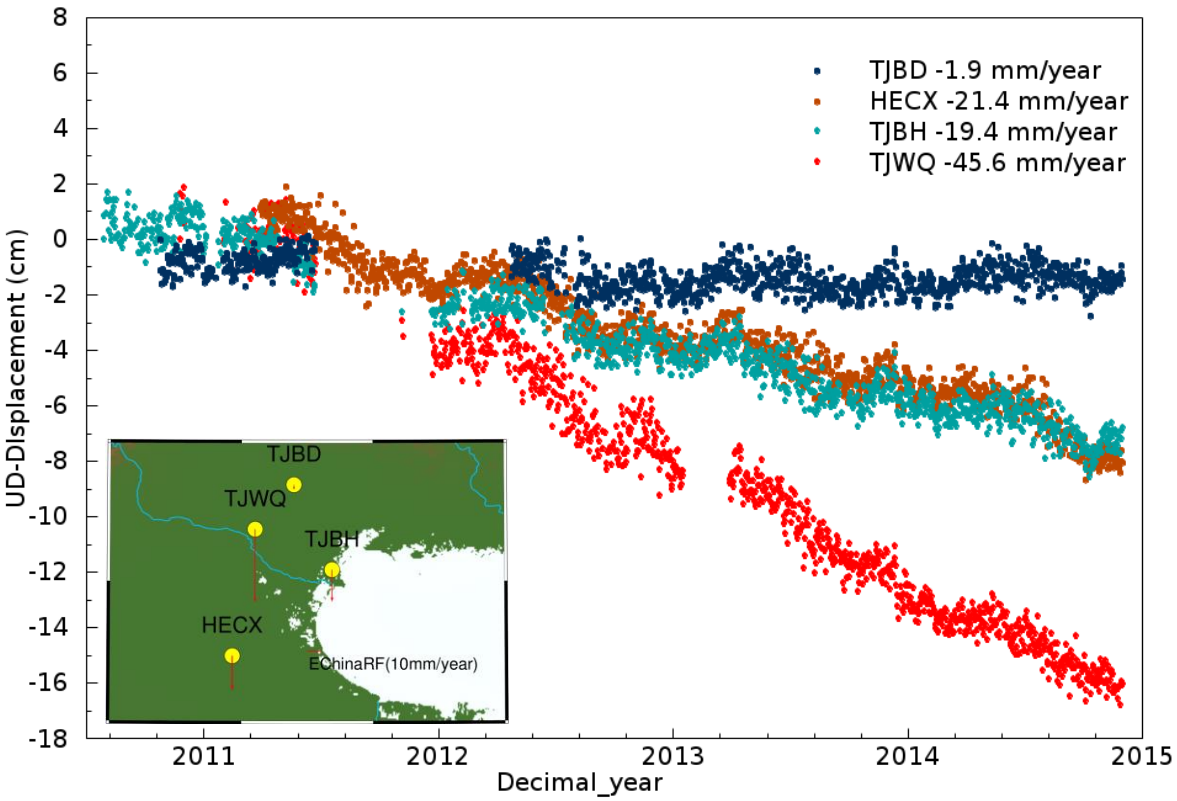

Figure 4-7 Comparison of vertical displacement time series at four stations: TJBD, HECX, TJBH, and TJWQ referred to SEChinaRF (2010-2014). The subsidence rates of these stations are: 1.9 mm/year at TJBD; HECX, mm/year at HECX; 19.4 mm/year at TJBH; 45.6 mm/year at TJWQ.

4.4 Driving factors of subsidence in Tianjin area.

Excessive exploitation of groundwater and petroleum as well as mining can result in a slow but eventually significant land subsidence. (Abidin et al. 2001; Ferronato et al. 2003; Leake 2004). It may cause geological, hydrogeological, environmental, and economic impacts (Holzer and Johnson 1985; Holla and Barclay 2000; Abidin et al. 2008; Phien-wej et al. 2006). This attracts a lot of attention from the government, communities, industries, and academia. Although it cannot be completely avoided in groundwater resource-dependent areas, land subsidence can be controlled more sustainably through governmental legislation, monitoring, industrial plans, and technological advances (Singh 1986, Abidin et al. 2008). A thorough analysis of the exact causes of the land subsidence is crucial for the control and prevention of the subsidence.

Subsidence can have natural as well as human-induced causes. The natural causes include tectonics, glacial isostatic adjustments, and natural sediment compaction. Subsidence caused by human activities occurs as a result of compression of shallow layers by the weight of buildings, or as a result of drainage and the subsequent oxidation and consolidation of organic soils. In deeper layers, subsidence is caused by the extraction of resources, such as oil, gas, coal, salt, and groundwater, and excessive groundwater extraction due to rapid urbanization and population growth, which can be a major cause of severe land subsidence.

Tianjin has the longest history of groundwater exploitation in China. By 1948, there were 51 groundwater pumping wells in Tianjin, with a pumping volume of approximately 4×10^4 m^3/year (Tianjin Municipal Editorial Board of Local Chronicles, 2004). The groundwater pumping volume has drastically increased since 1949 as a result of rapid economic development and urbanization. The history of groundwater withdrawal can be divided into three stages. The first stage is the period of continuous increase before 1981 as result of economic development. The second stage is the period of rapid decrease from 1981 to 198 that was attributed to the implementation of pumping regulations. The third stage refers to the gradual increase occurring after 1989 that has continued to the present. The annual groundwater pumping volume from 1981 to 2007 is shown in Figure 4-8. In the 1970s, the average pumping volume was 7.1×10^8 m^3/year; this number reached a maximum of up to 12 × 108 m3/year in 1981. Thereafter, the pumping volume gradually decreased because of a water transportation project of the Luan River to Tianjin City that was completed in 1983. After 1988, it gradually

increased, and the extraction rate was stable in the 1990s, and the average pumping volume was about 7×10^8 m^3/year.

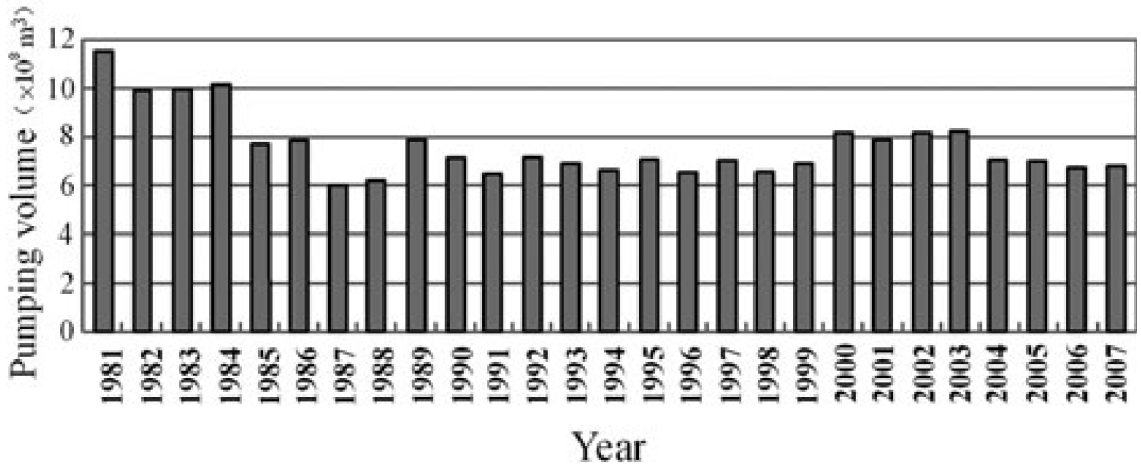

Figure 4-8 Annual groundwater pumping volume in Tianjin City from 1980 to 2007 (Yi et al., 2011).

Groundwater exploitation in each district in Tianjin has a difference process of change and at present has a different developmental trend, which is related to the severity of the measures implemented for the groundwater management and the importation of substitute water resource. Table 4-3 lists the annual groundwater pumping intensity of four district. The three GPS station, TJBD, TJWQ, and TJBH investigated in this study are located in Baodi District, Wuqing District, and Binhai District, respectively. The pumping intensity of Baodi in the northern part of Tianjin were larger than those of the other districts. However, because Baodi District id located in the bedrock areas, the groundwater exploitation did not induce noticeable land subsidence. According the observations at TJBD, the subsidence rate is only about 2 mm/year. In the rapidly industrialized suburban areas,

groundwater exploitation has been increased significantly. Taking the Wuqing District as an example, the average groundwater pumping intensity was 3.97 × 10^4, 3.97 × 10^4, 3.97 × 10^4, 3.97 × 10^4 m3/year km2 in the 1970s, 1980s, 1990s, and 2000s, respectively. This increasing groundwater pumping intensity resulted in the occurrence of a new subsidence center in Wuqing District. According to GPS station TJWQ, the subsidence rate is about 45 mm/year in this area. The urban area of Tianjin and Binhai new district (used to be named as Tanggu District) have experienced most severe land subsidence in China during the past 50 years. Therefore, groundwater withdrawal in these areas is strictly limited, so groundwater exploitation has continuously decreased since the 1980s.The observation at GPS station TJBH indicates a land subsidence of about 20 mm/year in the Binhai new district.

Table 4-3 Annual groundwater pumping intensity in the four areas of Tianjin from 1970 to 2000 (Yi et al., 2011).

	Average pumping intensity (1,000 m/a km^2)			
	1970s	1980s	1990s	2000s
Baodi	80.3	78.7	81.2	91.9
Wuqing	39.7	62.2	74.4	72.7
Binhai	60.0	75.6	24.1	27.5
Urban	333.8	207.2	46.8	45.2

The hydrogeological units of the Tianjin area can be divided into two systems, the Quaternary aquifer system and the Tertiary aquifer system (Yi et al., 2011). The Quaternary aquifer system ranges from the surface to 500 m, and the Tertiary aquifer system ranges from 500 to 1,100 m (Tianjin Geological Survey and

Mine Resource Administration, 1992; Angelo et al., 2008). The groundwater abstraction is restricted to the Quaternary aquifer system at present, which is closely related to the land subsidence in this area.

Pumping groundwater reduces pore water pressure in aquifers. For the aquifers with sand or conglomerate beds, which behave in an elastic manner, when groundwater is recharged, expansion of aquifer sand and gravel layers occurs and contributes to lifting up the ground surface as an elastic rebound (Waltham 2002). However, clay compaction is largely an irreversible, one-way process, and it is the major source of severe pumping-induced land subsidence (Terzaghi, 1925; Holzer, 1984; Phien-wej et al., 2006). Ground level change reflected in groundwater recovery is the competition between subsidence from the starved aquifer section and uplift from the recharged aquifer section (Chih et al., 2007).

Figure 4-9 illustrates the correlation between the groundwater pumping rate and subsidence velocity in the urban area of Tianjin. It is clearly seen that these two numerical values correlate very well, indicating that the dominant cause of land subsidence in Tianjin is groundwater pumping.

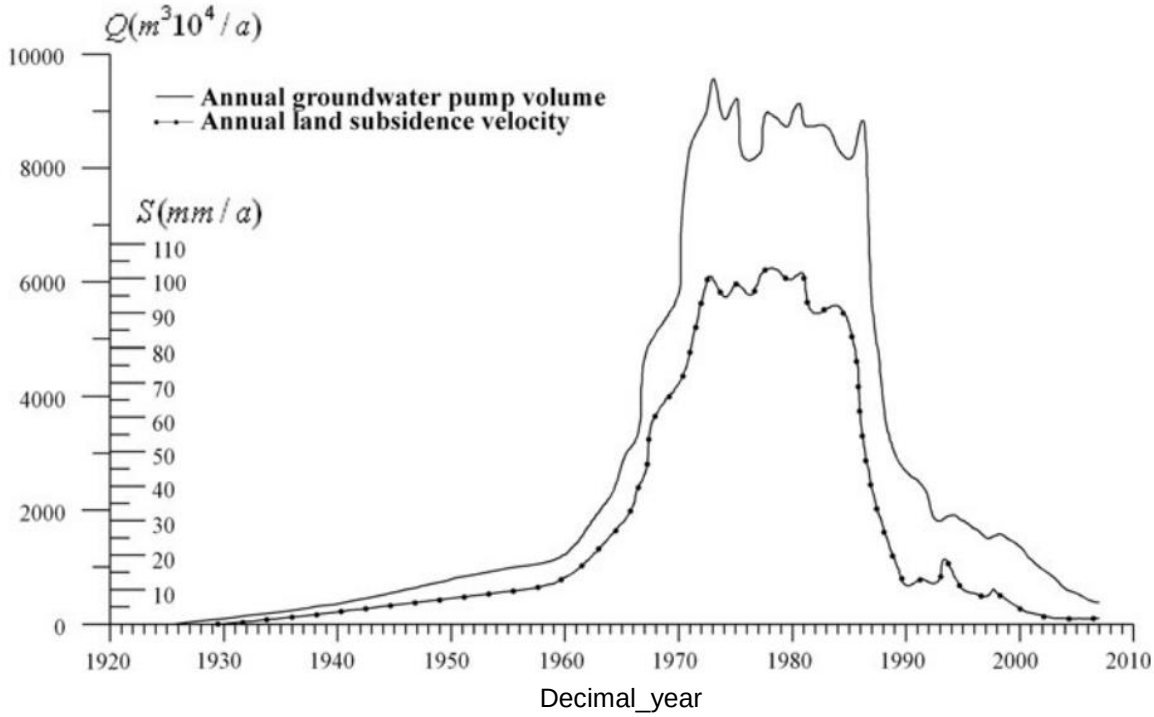

Figure 4-9 The relation curve of annual land subsidence velocity and annual groundwater pump volume in the urban area (Yi et al., 2011).

For the case of Tianjin, rapidly expanding urban areas require large amounts of water for the domestic and industrial water supply. This leads to over-exploitation of groundwater resources. Moreover, multiple large construction activities require site dewatering for foundation excavations. This causes lowering of the groundwater level as well, resulting in soil compaction, and, subsequently, land subsidence. Figure 4-10 demonstrates the comparison of the google satellite views of the three GPS stations in the Tianjin area. TJBD is located in a rural area surrounded by cropland, and it shows the least recognizable land subsidence with a rate of 1.9 mm/year. In contrast, TJBH and TJWQ are located in the suburban area with several buildings and human constructions. Accordingly, in addition to the ground water extraction, the weight of construction may be an additional cause of the severe land subsidence in the Tianjin area.

Figure 4-10 Comparison of the google satellite views at the locations of the three GPS stations, TJBD, TJWQ, and TJBH.

Several measures can be adopted to mitigate and prevent land subsidence disasters, including restricting groundwater exploitation, groundwater injection,

prohibiting use in a specific zone, a pricing policy for water resources, advocating water-saving technology, and strict enforcement of groundwater laws (Hu et al., 2009; Hu et al., 2004). This study showed that the GPS measurements could play an important role in multiple public policy decision making processes in the rapidly growing area.

Chapter 5 Land subsidence in other coastal areas

5.1 Introduction

Over the past 20 years, the rapid developments of urbanization and industrialization in China have resulted in increasing land subsidence issues and contributing to extremely expensive damage to the environment and the economy in a large number of coastal cities. Hu et al. (2004) concluded that the land subsidence of China can be classified into the following three types of geographic regions (Table 5-1): a) the coastal plain and river delta regions, such as Shanghai, Tianjin, and Hong Kong; b) the plain regions in front of major mountains, such as the North China Plain and the Songliao Plain; and c) regions in the valleys and basins among the mountains, such as Xi'an and Taiyuan.

The subsidence of particular cities and municipalities is briefly summarized in Table 5-2. More than 11 cities have experienced severe subsidence during the past 100 years. These cities include Shanghai, Tianjin, Suzhou, Wuxi, Changzhou, Cangzhou, Xian, Fuyang, Taiyuan, and An'yang (Hu et al., 2004). The land subsidence in China has been caused primarily by the increasing withdrawal of groundwater. These cities experiencing subsidence are also cities with a rapid expansion and development of industrialization and urbanization in China during the last two decades.

Table 5-1 Geographical distribution of major cities where substantial land subsidence in China are occurring (Hu et al., 2004)

Geographical units	Number	Percentage of subsiding cities (total cities: 39) (%)	City name
The coastal plain and river delta region	14	36	Shanghai, Tianjin, Suzhou, Wuxi, Changzhou, Ningbo, Jiaxing, Hezhe, Jiing, Dezhou, Fuyang, Zhanjiang, Haikou, Fuzhou
The plain region in front of major mountains	19	49	Beijing, Cangzhou, Hengshui, Renqiu, Hejian, Bazhou, Baoding, Dacheng, Nangong, Feixiang, Handan, Xuchang, Kaifeng, Luoyang, An'yang, Ha'erbing, Daqing, Qiqiha'er, Jiamusi
Regions in valleys and basins among mountains	6	15	Taiyuan, Datong, Yuci, Jiexiu, Xi'an, Kunming

Table 5-2 Summary of the land subsidence conditions in major cities of China (Hu et al., 2004; Duan, 1998)

Major city	Subsidence area (km^2)	Brief history of land subsidence in each city
Shanghai	850	The land subsidence began in 1920. The most serious subsidence occurred in 1964. The maximum subsidence is 2.63 m. The subsidence has been controlled gradually. Currently, the ground surface is at a state of minor fluctuation of subsidence and rebound.
Tianjin	11,760	Since 1959, subsidence has been occurring on the plain with an area of 10,000 km^2. The maximum subsidence is 3.06 m, and the subsidence rate is 160 mm/year. Currently, the average subsidence rate is between 8 and 56 mm/year.
Suzhou, Wuxi, Changzhou	380	Subsidence appeared in 1960. Their accumulative subsidence is 1.1, 1.05, and 0.9 m, and the current maximum subsidence rates are 40–50, 15–25, and 40–50 mm/year, respectively.
Ningbo, Jiaxing	263	The maximum accumulative subsidence is 0.346 and 0.597 m, respectively, from 1960 to 1989. The present maximum subsidence rates are 18 and 41.9 mm/year.
Xi'an	250	Seven subsidence centers appeared beginning in the 1950s; the maximum accumulative subsidence is 1.9 m, and the maximum subsidence rate is 136 mm/year.
Xuchang, Kaifeng, Luoyang, An'yang	59	Subsidence appeared in 1985, 1979, and 1979, and the maximum subsidence amount to 0.208, 0.21, 0.113, and 0.337 m, respectively. An'yang is the regional subsidence, and the rate is about 65 mm/year.
10 cities in Hebei Province	36,000	Subsidence began in the 1950s on the Hebei plain and formed 10 subsidence centers: Cangtzhou, Hengshui, Renqiu, Hejian, Bazhou, Baoding, Dacheng, Nangong, Feixiang, and Handan. The maximum accumulative subsidence is 1.131 m, and the rate is 96.8 mm/year.
Beijing	314	Subsidence began at the end of the 1950s. The maximum accumulative subsidence is 0.597 m.
Zhanjiang	0.25	Subsidence appeared in the 1960s. The accumulative subsidence is 0.11 m. Subsidence has been controlled basically because of decreasing groundwater withdrawal.

In this chapter, I investigated the land subsidence that has occurred in the other coastal provinces and cities of east China. Three-component displacement time series of several GPS stations referred to both IGS08 and SEChinaRF were examined. Figure 5-1 illustrates the locations of the GPS stations examined in this study and the positions of the four areas - Tianjin, Shandong, Shanghai, and Guangdong, where different patterns of land subsidence were observed. Land subsidence in Tianjin has been studied and discussed in chapter 4. By a thorough investigation of the vertical displacements of another 11 GPS stations, different patterns of land subsidence were observed at Shandong province, Shanghai, and Guangdong province.

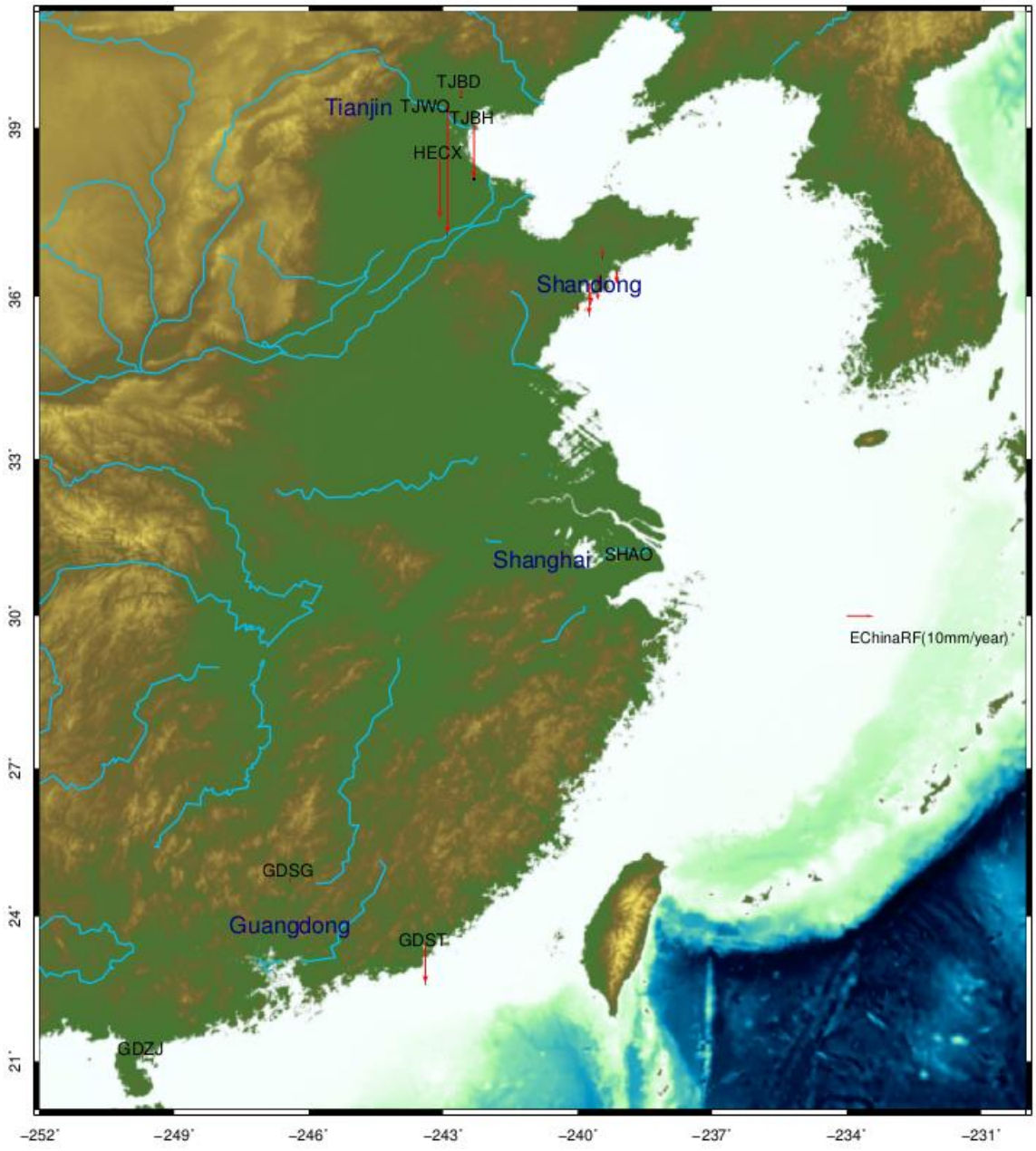

Figure 5-1 Map showing the positions of the cities and provinces investigated along the east coastal region of China. Red arrow presents the subsidence rate of each GPS station within SEChinaRF.

5.2 Shandong

Shandong is a coastal province of China and part of the East China region. It is located on the eastern edge of the North China Plain in the lower regions of the Yellow River and extends out to the sea in the form of the Shandong Peninsula (Figure 5-1). Shandong borders the Bohai Sea to the north, covers an area of 157,100 km^2, and has a population of 97,333,900. Qingdao is a major city in the eastern Shandong Province. Qingdao includes a small peninsula and the surrounding areas on the East China Sea facing South Korea.

Seven permanent GPS stations with continuous data of over 33 months were investigated. Among these stations, JNAN, HDAO, XIAO, QYLU, and TIAN are located in the city of Qingdao; JIMO is located in the city of Jimo, which is located to the north of Qingdao; and LAIX is located in the city of Laixi (Figure 5-2). Table 5-4 illustrates the survey periods, position coordinates, and subsidence rates (referred to SEChinaRF) of these seven GPS stations. Figure 5-3 shows the comparison of the vertical displacement time series of the seven GPS stations in Shangdong referred to SEChianRF from 2010 – 2013. And the three-component displacement time series, referred to both IGS08 and SEChinaRF, of each station are shown in Figures 5-4 ~ 5-10. It can be founded that, the largest subsidence was record at HDAO, with a rate of 11.3 mm/year. And for the other six stations, the subsidence rates are between 2.9 mm/year and 4.9 mm/year.

Table 5-3 Subsidence in Shandong

Station ID	Observation period	Longitude (°)	Latitude (°)	Subsidence rate (IGS08) (mm/yr)	Subsidence rate (SEChinaRF) (mm/yr)	Standard deviation (mm/yr)
XIAN	02/2010-08/2012	-250.7785	34.3686	-3.43	-4.19	0.17
XIAO	02/2010-08/2012	-239.6961	36.0767	-4.12	-4.15	0.77
HDAO	02/2010-08/2012	-239.7450	36.2340	-11.26	-11.31	0.89
JNAN	02/2010-08/2012	-239.9963	35.8763	-2.84	-2.86	0.58
LAIX	02/2010-08/2012	-239.4402	36.9031	-3.77	-3.87	0.61
QYLU	02/2010-08/2012	-239.5531	36.1376	-4.06	-4.09	0.74
TIAN	02/2010-08/2012	-239.1263	36.4687	-4.92	-4.95	0.79

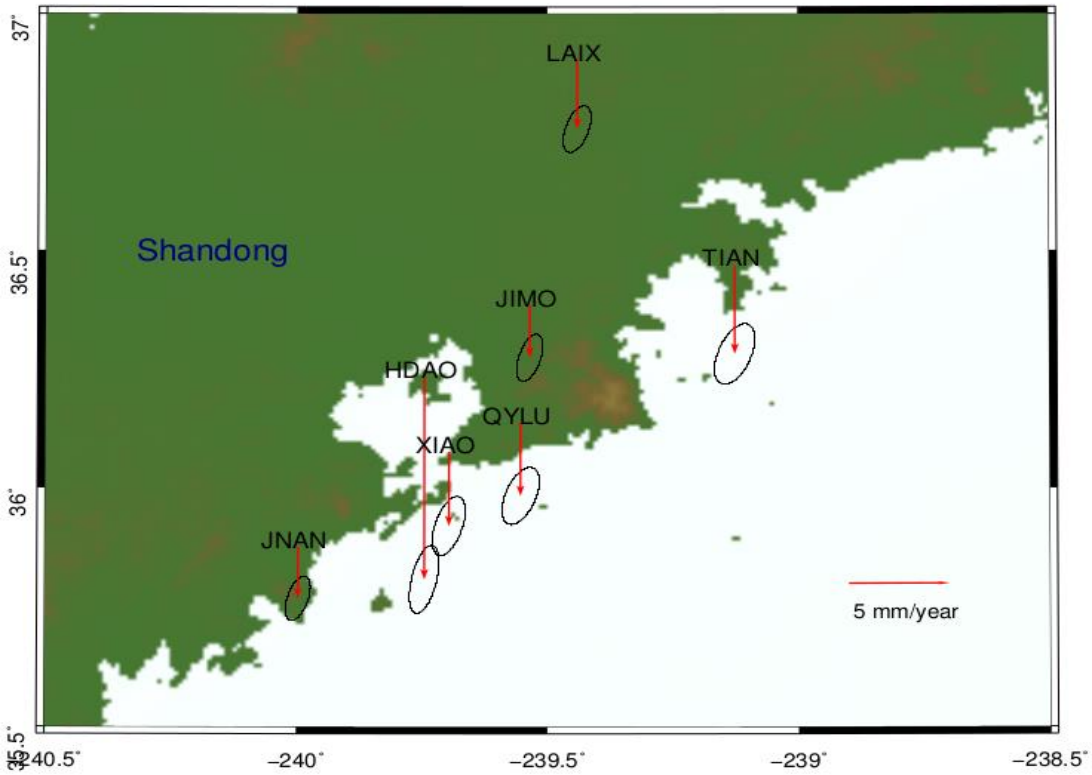

Figure 5-2 Map illustrating the subsidence of seven GPS stations along the east of coast of Shandong. The error ellipses represent 90% confidence.

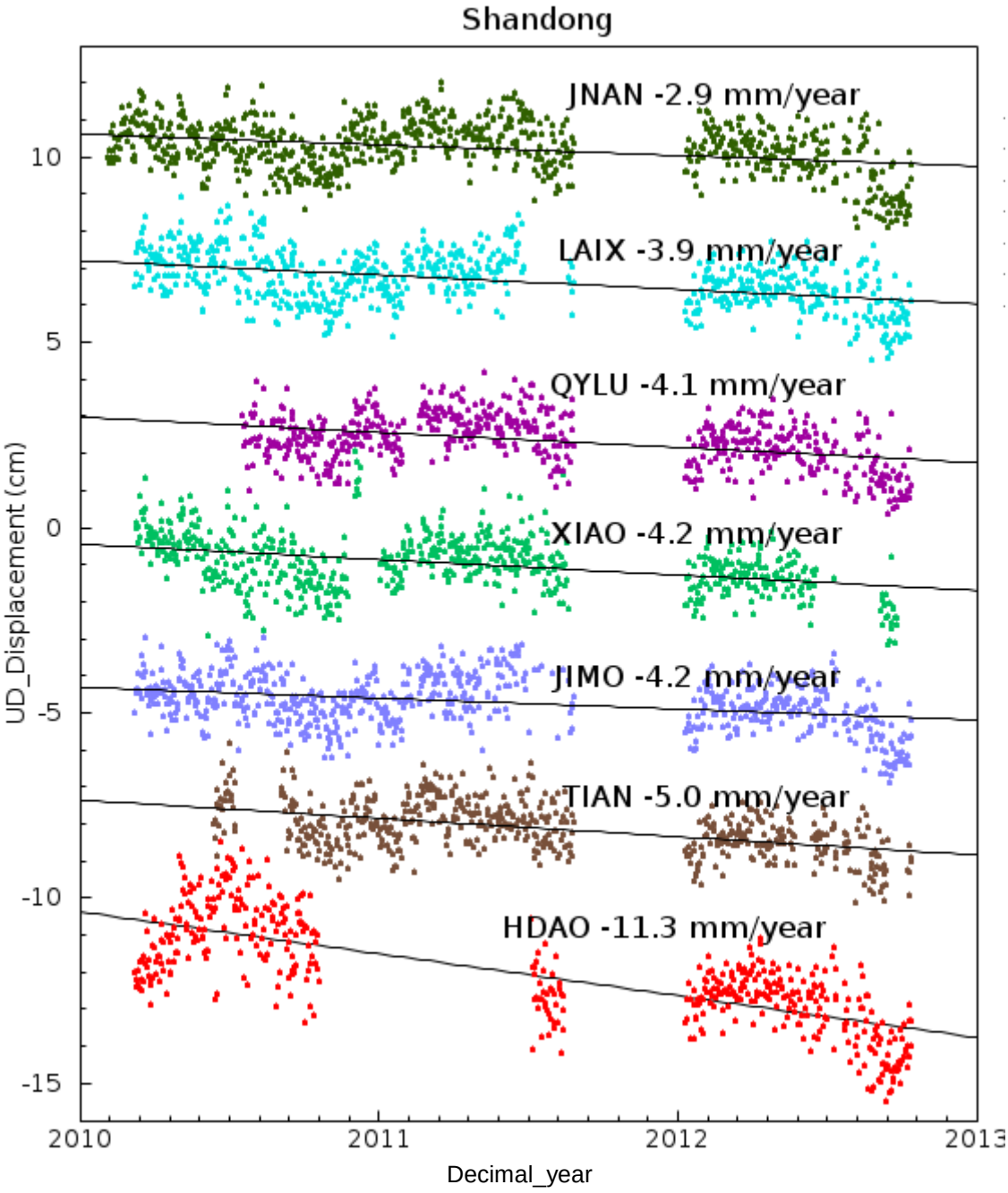

Figure 5-3 The vertical displacement time series of the seven GPS stations in Shandong referred to SEChinaRF from 2010 – 2013.

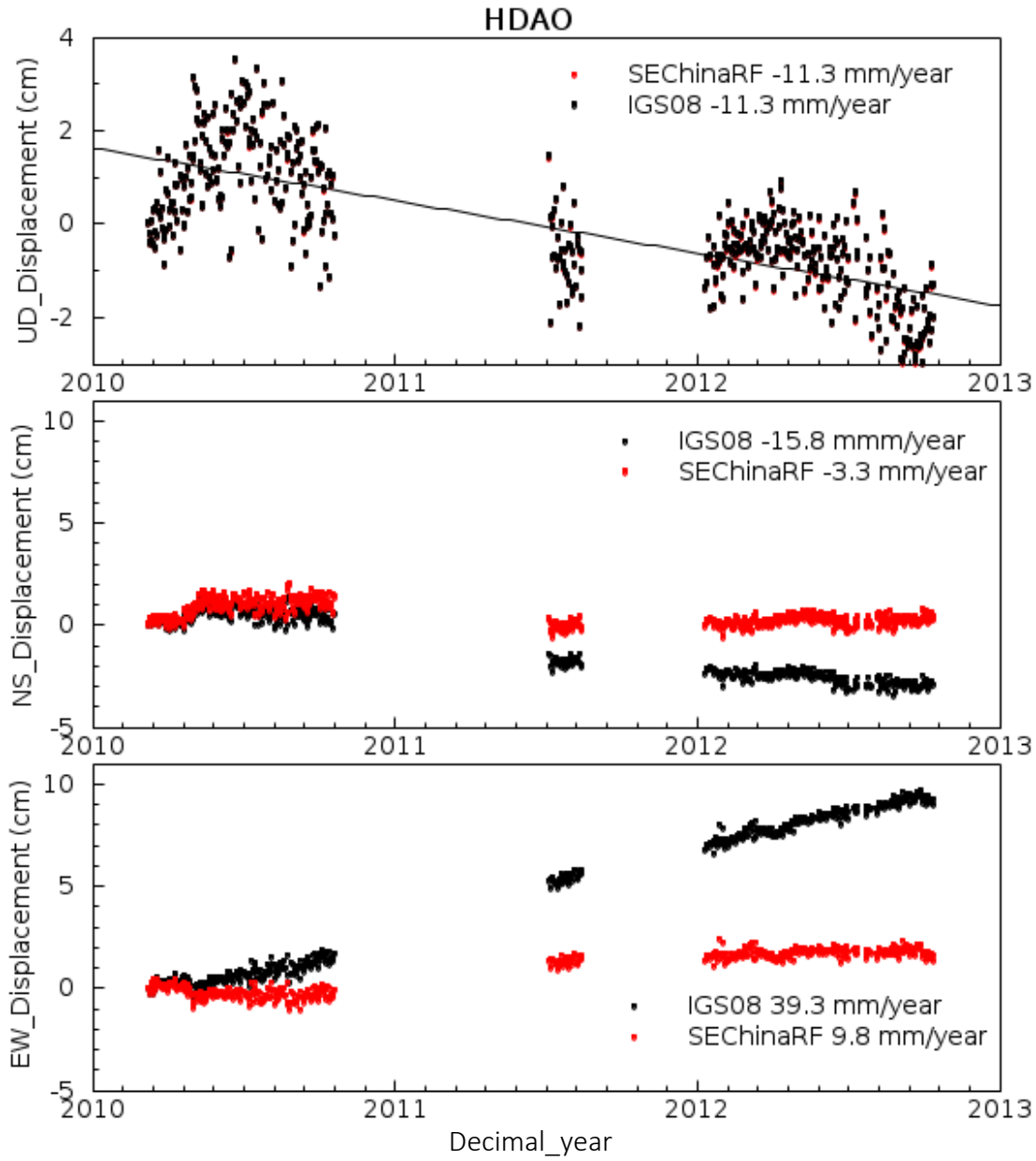

Figure 5-4 Displacement time series at HDAO (2010-2012) referred to IGS08 (global, red) and SEChinaRF (local, black)

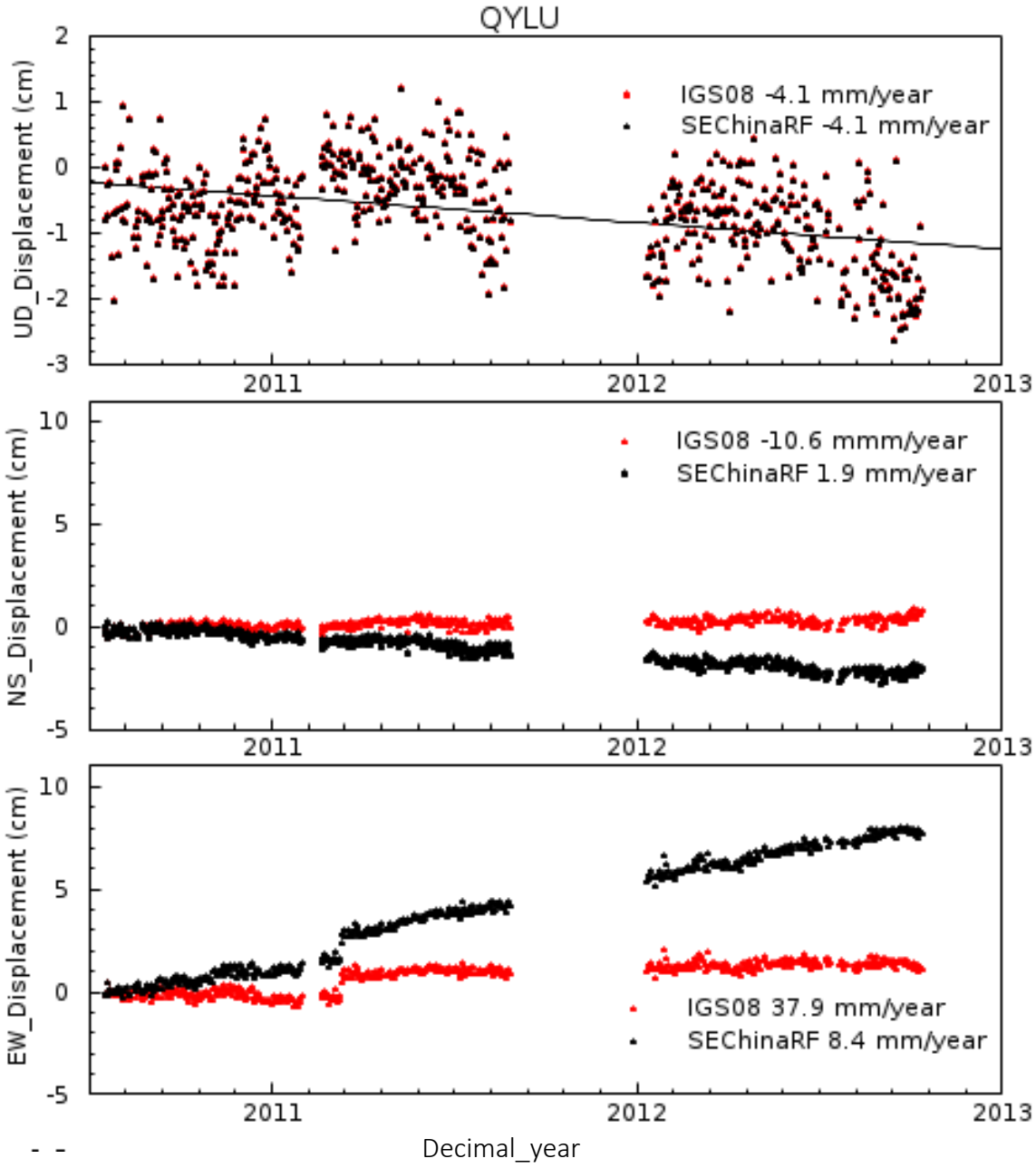

Figure 5-5 Displacement time series at QYLU (2010-2012) referred to IGS08 (global, red) and SEChinaRF (local, black)

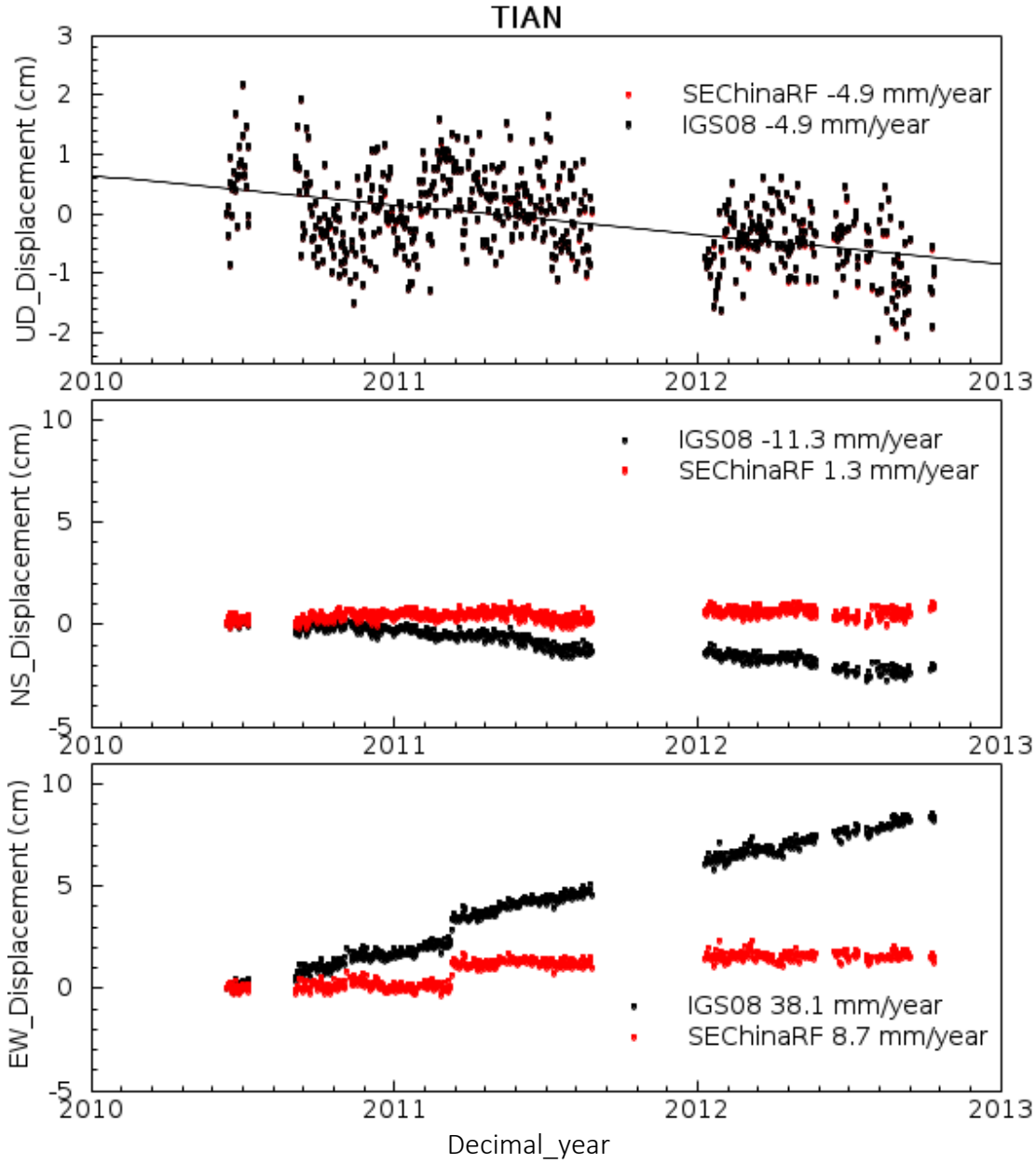

Figure 5-6 Displacement time series at TIAN (2010-2012) referred to IGS08 (global, red) and SEChinaRF (local, black)

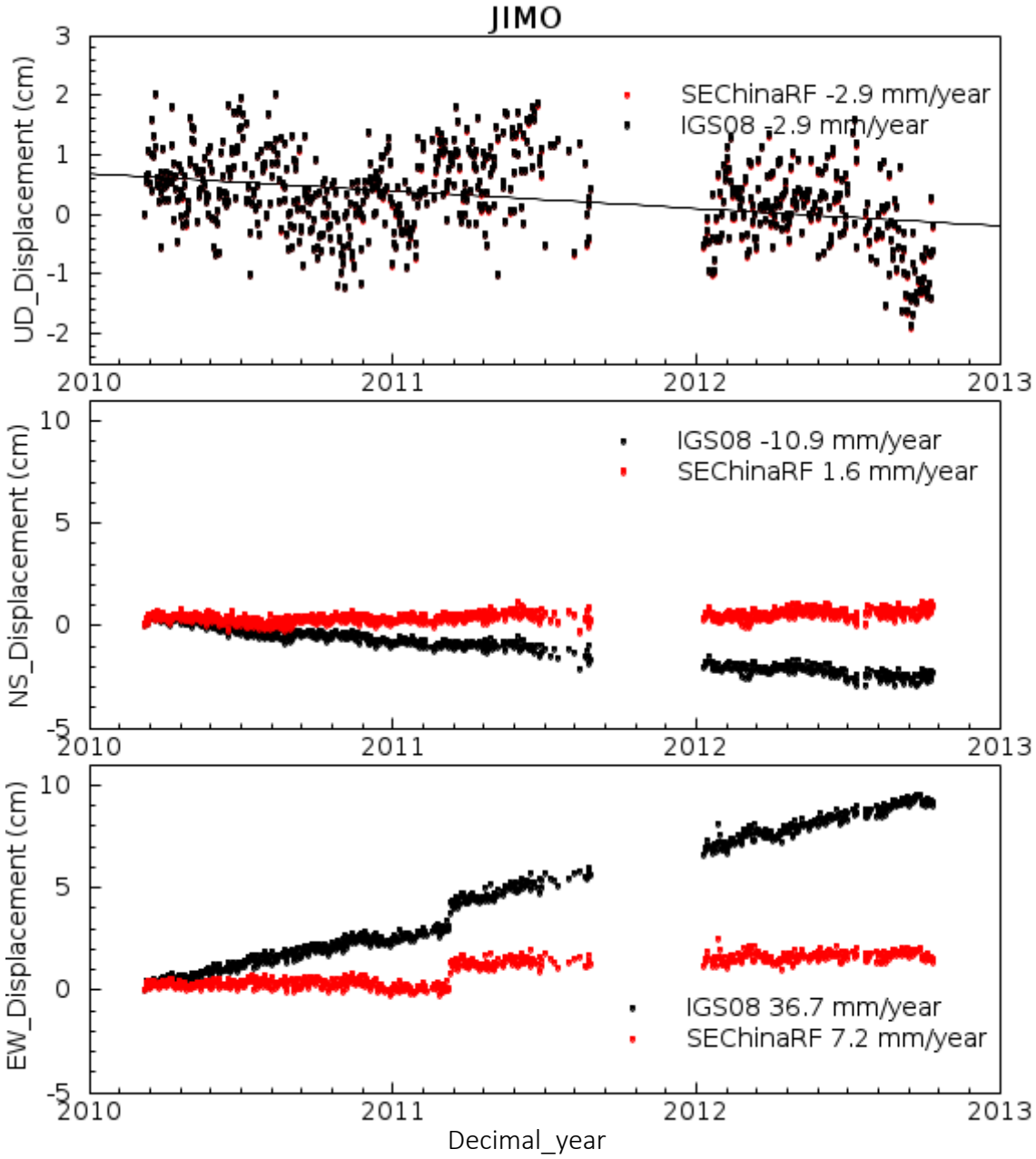

Figure 5-7 Displacement time series at JIMO (2010-2012) referred to IGS08 (global, red) and SEChinaRF (local, black)

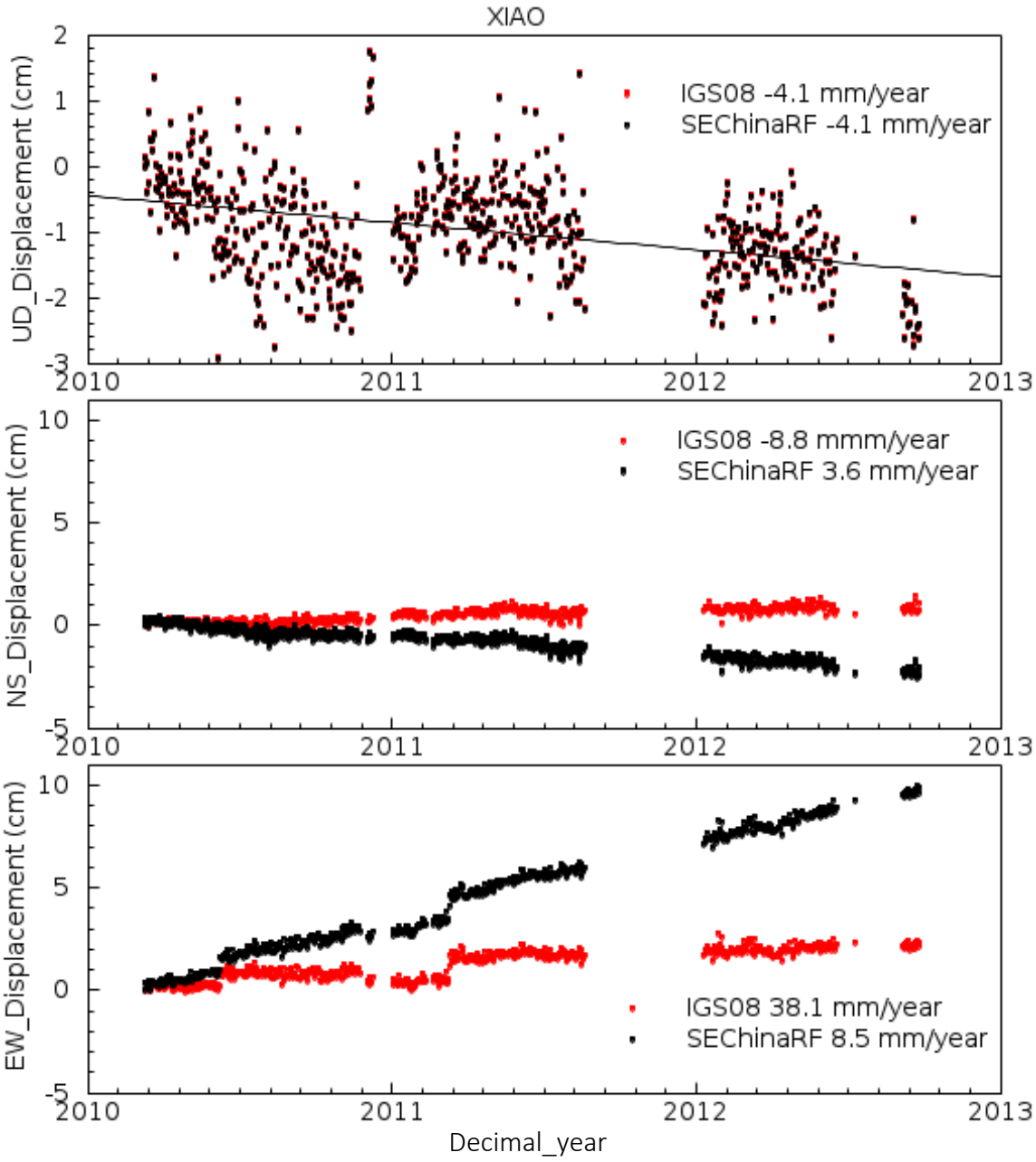

Figure 5-8 Displacement time series at XIAO (2010-2012) referred to two reference frames: IGS08 (global, red) and SEChinaRF (local, black)

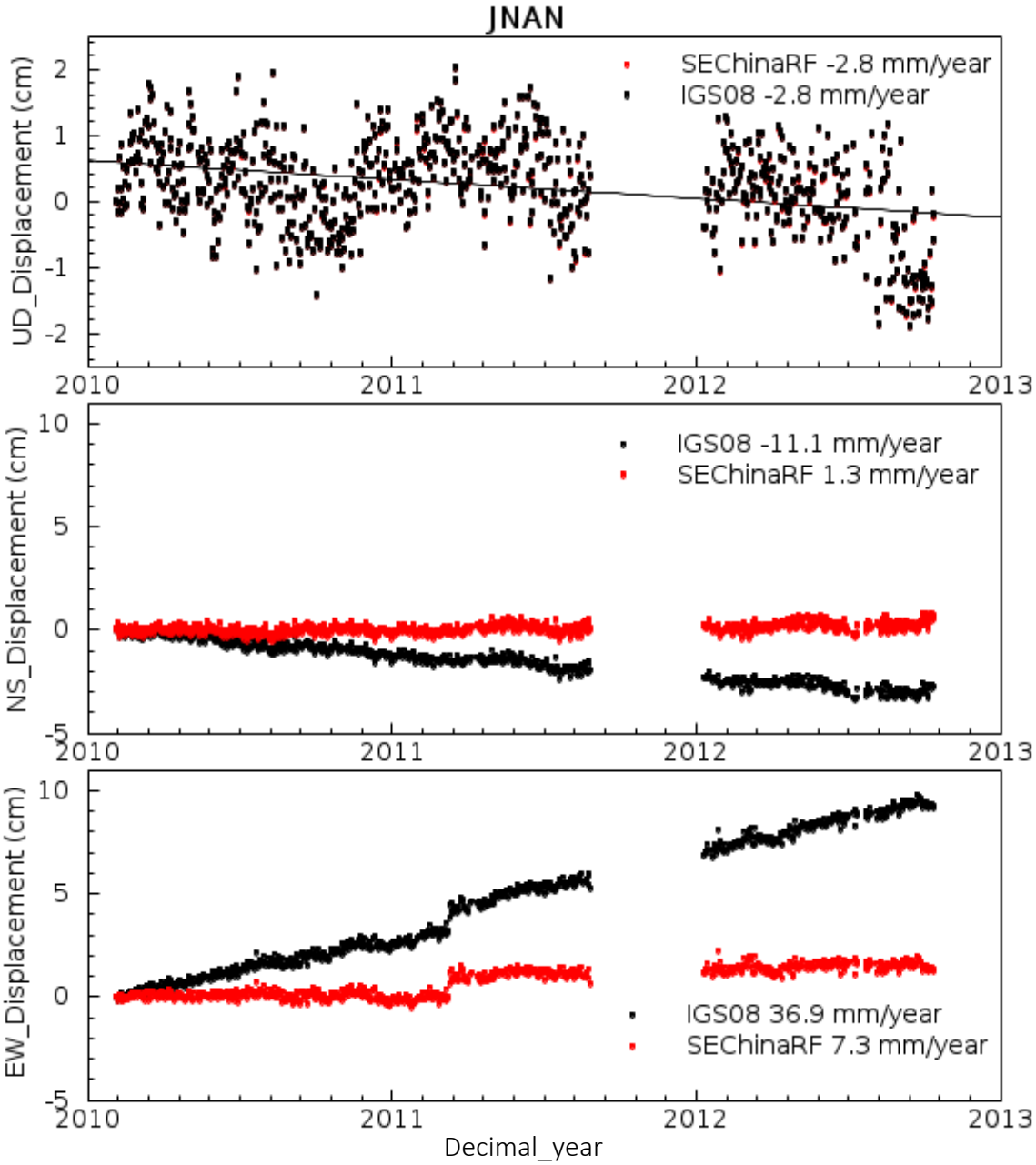

Figure 5-9 Displacement time series at JNAN (2010-2012) referred to two reference frames: IGS08 (global, red) and SEChinaRF (local, black)

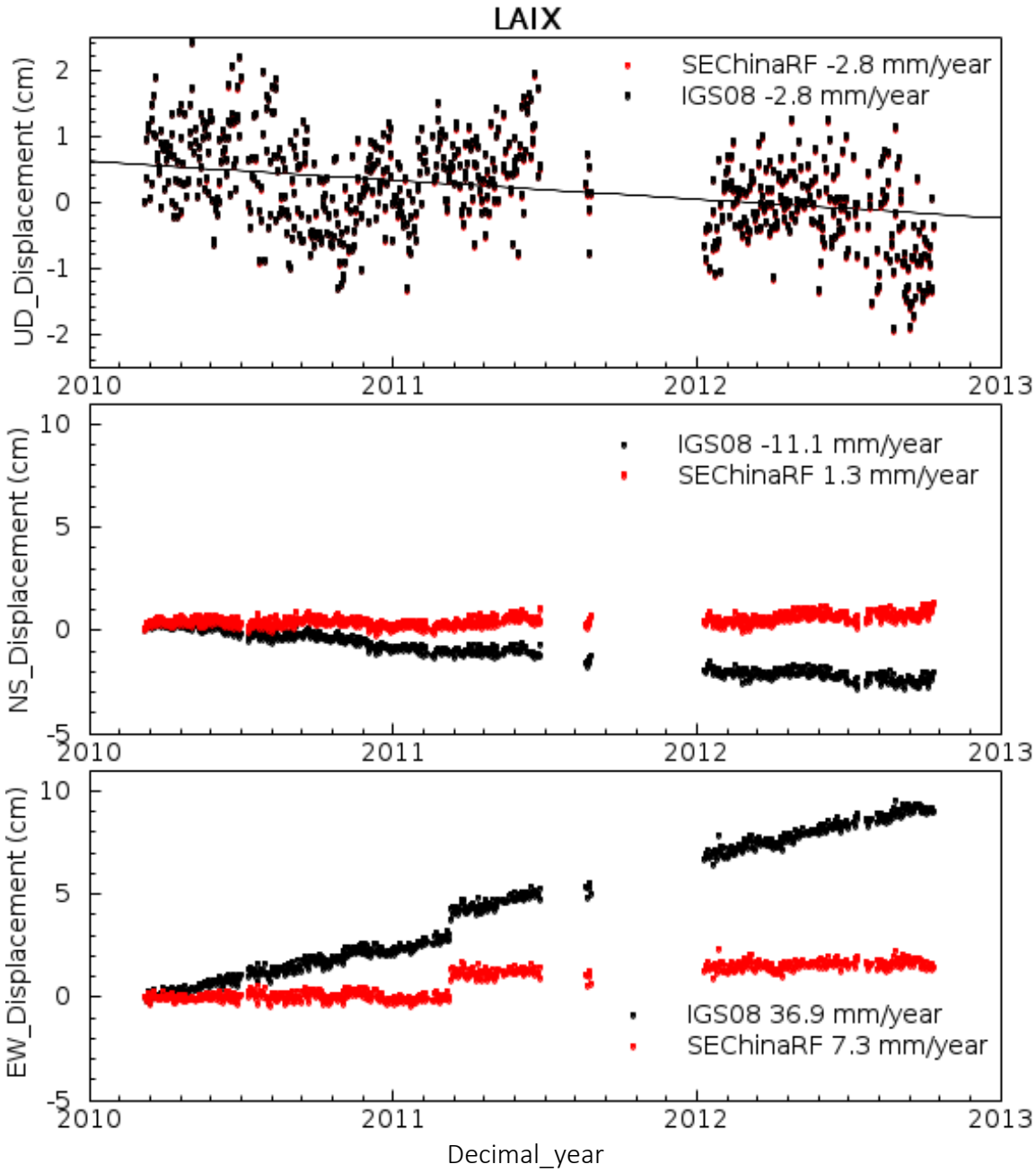

Figure 5-10 Displacement time series at LAIX (2010-2012) referred to IGS08 (global, red) and SEChinaRF (local, black)

5.3 Shanghai

Shanghai is located on the deltaic deposits of the Yangtze River, as shown in Figure 5-1. The total thickness of the Quaternary deposits is about 300 m (Shanghai Geology Office, 1976). Excessive pumping of the groundwater caused compression of the Quaternary deposits, and, subsequently, land subsidence in Shanghai. This has resulted in several social problems in Shanghai. The immediate problem is the increased possibility of flooding. Since 1956, the height of the dike along the coastline increased four times with the crest elevation rising from 5 m to 6.8 m to prevent the potential floods. Other problems have been caused by the land subsidence, including damage to the sewer system, roads, buildings, and subway tunnels.

The Quaternary deposits in Shanghai consists of five aquifers separated by five clayey layers (aquitards). Based on the data reported by the Shanghai Geology Office (1976), an illustrative soli profile with some available physical and mechanical properties is given in Figure 5-10. According to Chai et al. (2004), aquitard I can be divided into the upper mucky clay layer (the first compression layer) and the lower mucky silty clay layer (the second compression layer). Aquitard II consists of the upper mucky silty clay and the lower silty clay layers, which is named as the third compression layer. These two aquitards (I and II) are the main compression layers in Shanghai.

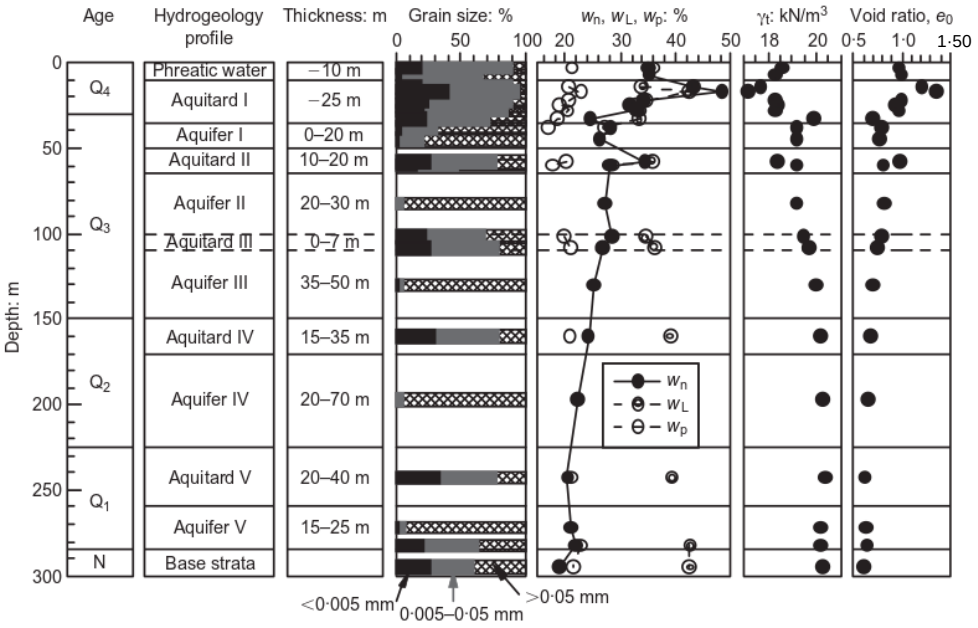

Figure 5-11 An illustrative soil profile at Shanghai (Chai et al., 2004)

In Shanghai, the monitoring of land subsidence began in 1921, and the measured amount of subsidence is 2–3 m in the central area of Shanghai. The history of land subsidence in the urban area of Shanghai can be divided into two periods: a rapid subsidence period (1921–1965) and a controlled period (1965–present) (Zhang and Han, 2002). There has been an increasing period of the subsidence rate from 1990 to 2001.The subsidence rate and the net groundwater pumping rate (net = pumped – recharged) in Shanghai are listed in Table 5-4, from which a strong relationship between the rate of net groundwater pumping and the rate of land subsidence can be observed. The use of recharge to control land subsidence started since 1956, therefore the amount of recharge before 1965 can be taken as zero. From 1957 to 1961, the net groundwater pumping rate was about 200×10^6 m^3/year, and the subsidence rate was as large as 100 mm/year. During the period 1966 to 1989, the net groundwater pumping rate was reduced to about

72×10^6 m^3/year, and the subsidence rate was only 2 mm/year. After 1990, the net groundwater pumping rate was increased again, and the subsidence rate increased accordingly. Figure 5-11 shows the amount of groundwater pumped and recharged from 1961 to 2001.

Table 5-4 Subsidence rate and groundwater pumping rate (Chai et al., 2004).

Period	Average subsidence rate: mm/year	Area of subsidence > 500 mm: km^2	Average amount of groundwater pumping: 10^6 m^3/year	Average amount of recharge to groundwater: 10^6 m^3/year	Net groundwater pumped: 10^6 m^3/year
1921-1948	23	19.3	9	0	9
1949-1956	43	92.8	140	0	140
1957-1961	100		200	0	200
1962-1965	60		156	0	156
1966-1989	2		89	17	72
1990-2001	16	Expanded to suburban area	127	14	113

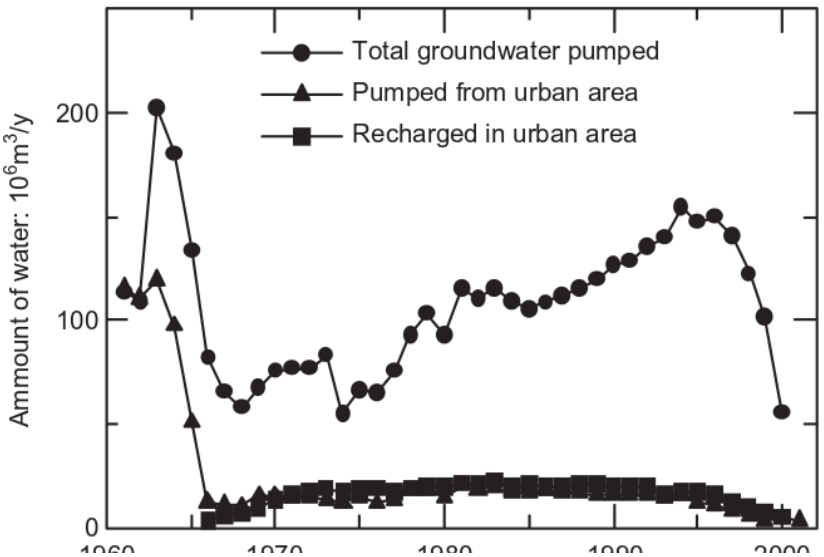

Figure 5-12 Amount of groundwater pumped and recharged (Chai et al., 2004)

Figure 5-12 shows the amount of groundwater pumped from each aquifer in Shanghai. The groundwater was pumped mainly from aquifers II and III before 1965. Then the groundwater pumped locations were shifted to aquifers IV and V, this was because that the compressibility of the lower soil layers is lower than the upper layers. Due to the study of Chai et al. (2004), this variation of the amount of groundwater pumped from each aquifer resulted in a change of groundwater level in each aquifer, and the water level variation in aquifers II, III and IV relates closely to the amount of compression of aquitards and aquifers.

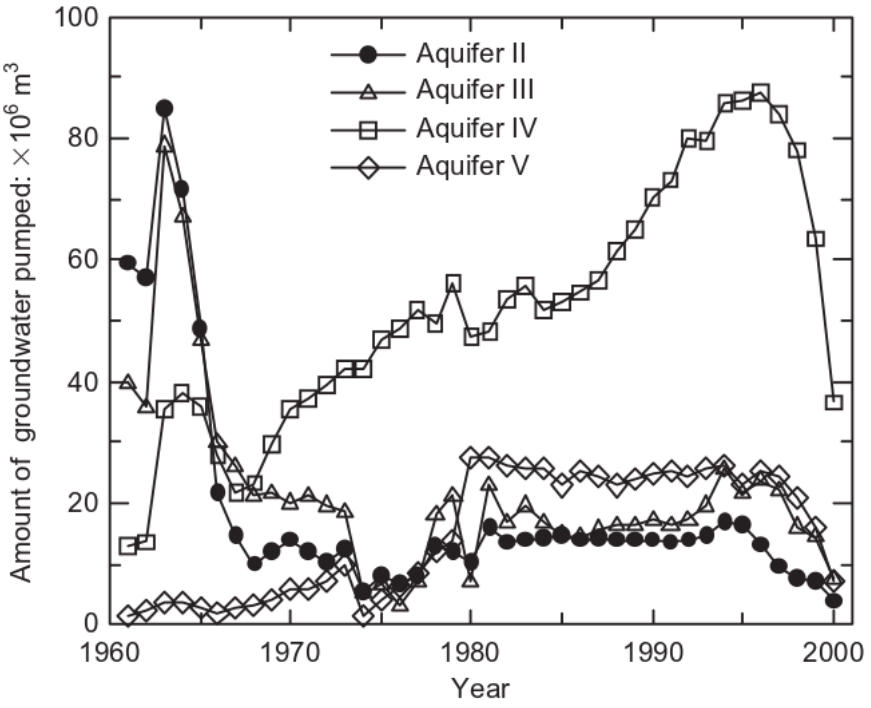

Figure 5-13 Amount of groundwater pumped from each aquifer (Chai et al., 2004)

According to the strong correlation between the amounts of groundwater pumped, the groundwater level in each aquifer, and the rate of land subsidence, the key factor in preventing land subsidence in Shanghai is to control the net rate

of groundwater pumping. In Table 5-4, the rate of land subsidence was about 2 mm/year, with the average net groundwater pumped of 72×10^6 m^3/year. The number indicates that, under the condition of not causing significant water table drawdown in aquifers, the yearly net amount of groundwater can be pumped in the Shanghai area will be around 70×10^6 m^3/year.

In early 2011, the Chinese government established the Group of GPS Data Analysis and Applications (GGDAA) at the Shanghai Astronomical Observatory. And a continuously operating reference station, SHAO, was established at same location in 1996. Figure 5-10 shows the three component displacement time series of SHAO from 1996-2014. It is indicated that the vertical displacement time series of SHAO is comprised of two identifiable time periods: 1997-2004 and 2004-2014. During the first period, no considerable subsidence was recorded at SHAO, and since 2003, the subsidence rate was about 2.2 mm/year. Table 5-5 presents the comparison of the two time period of land subsidence record at SHAO.

Table 5-5 Comparison of the two time period of land subsidence at SHAO (1996-2014)

Station ID	Observation period	Longitude (°)	Latitude (°)	Subsidence rate (IGS08) (mm/yr)	Subsidence rate (SEChinaRF) (mm/yr)	Standard deviation (mm/yr)
SHAO	1996-2004	-238.7995	31.0996	0.89	0.86	0.08
SHAO	2004-2014	-238.7995	31.0996	-2.32	-2.20	0.08

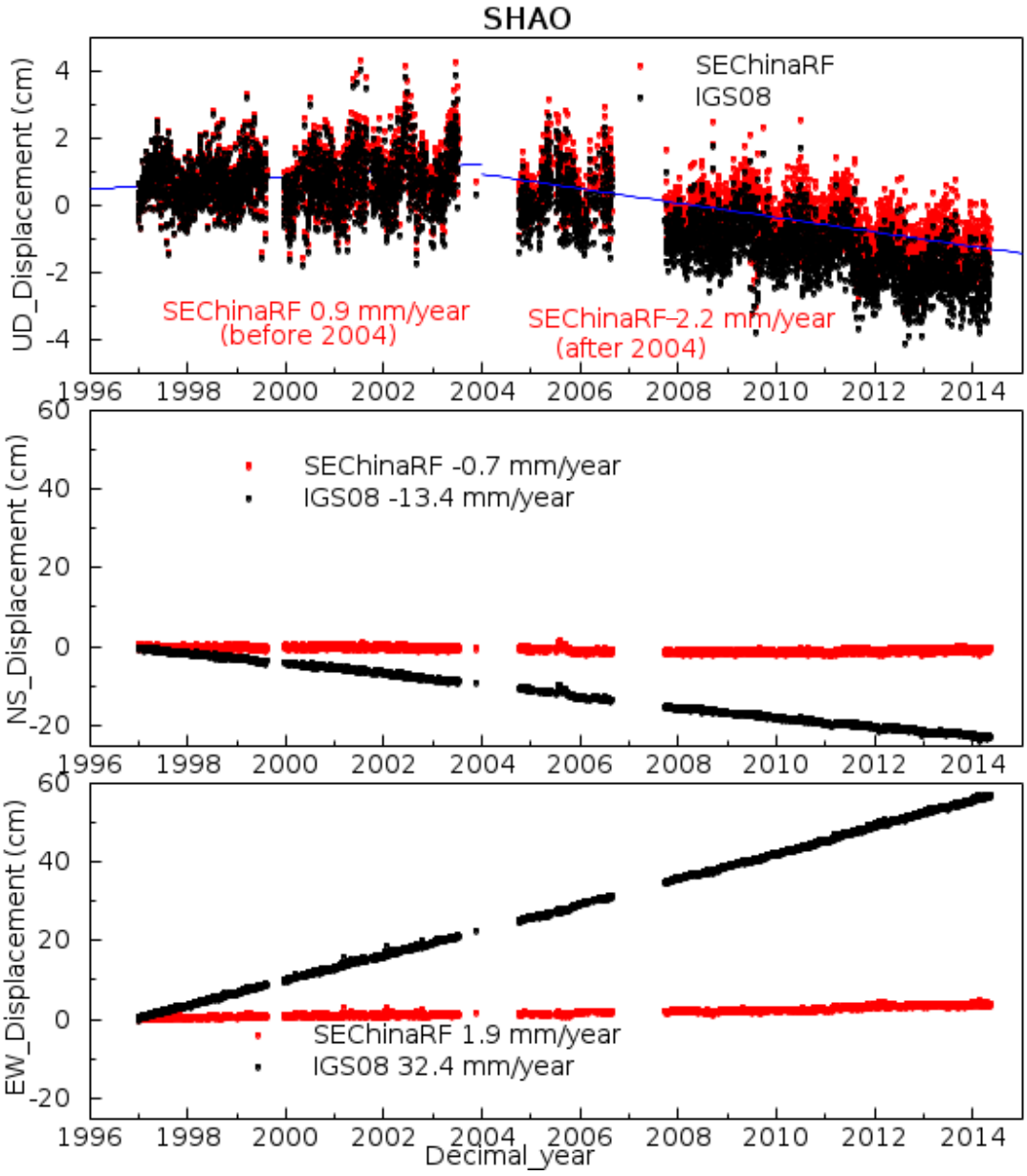

Figure 5-14 Displacement time series at SHAO (1997-2014) referred to two reference frames: IGS08 (global, red) and SEChinaRF (local, black)

5.4 Guangdong

Guangdong is a province located on the coast of the South China Sea (Figure 5-1). It is formerly known as Canton or Kwangtung in English. It covers an area of 179,800 km^2 and has a total population of over 100 million. Guangdong faces the South China Sea to the south with a coastline of 4,300 km and the Leizhou Peninsula on the southwestern end of the province. Guangdong borders Hong Kong and the Macau Special Administrative Regions to the south.

Three GPS stations (GDST, GDSG, and GDZJ) of CMONOC with over a four-year data collection history were investigated. Figure 5-1 shows the distribution of these three stations. Since they are separated by considerably large distance, the vertical displacements of these three stations present different patterns. As shown in Figures 5-11, 5-12, and 5-13, the largest subsidence was observed at GDST, which was 6.9 mm/year; a vertical displacement of -0.3 mm/year was recorded at GDZJ; and the subsidence rate at GDSG was 3.2 mm/year.

Table 5-6 Land subsidence at three GPS stations in Guangdong province (2010-2014)

Station ID	Observation period	Longitude (°)	Latitude (°)	Subsidence rate (IGS08) (mm/yr)	Subsidence rate (SEChinaRF) (mm/yr)	Standard deviation (mm/yr)
GDSG	08/2010-09/2014	-246.4122	24.8461	-3.90	-3.25	0.39
GDST	08/2010-09/2014	-243.3969	23.4178	-14.99	-13.91	1.10
GDZJ	08/2010-09/2014	-249.6960	21.1548	-2.07	-1.35	0.50

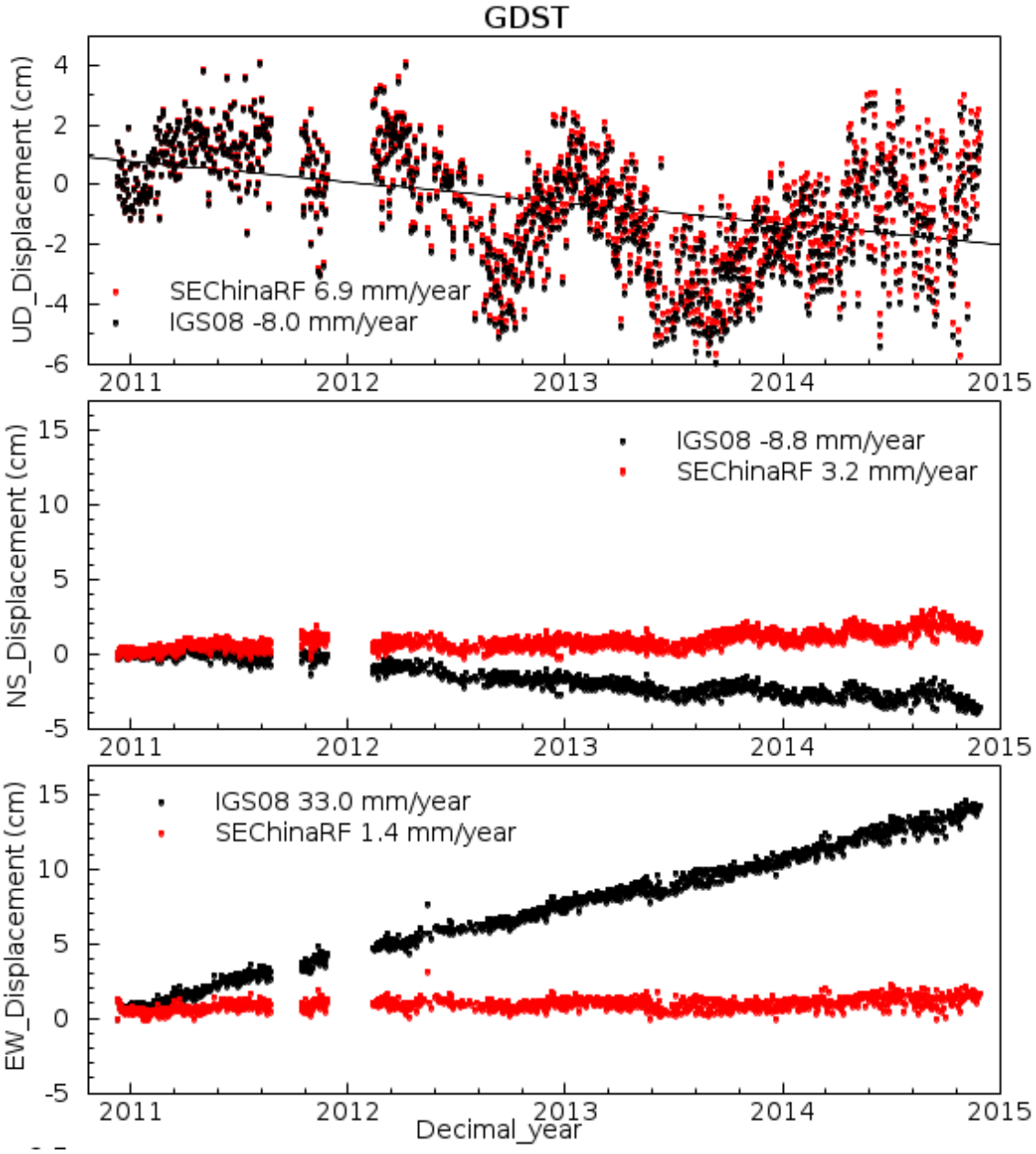

Figure 5-15 Displacement time series at GDST (2010-2014) referred to IGS08 (global, red) and SEChinaRF (local, black)

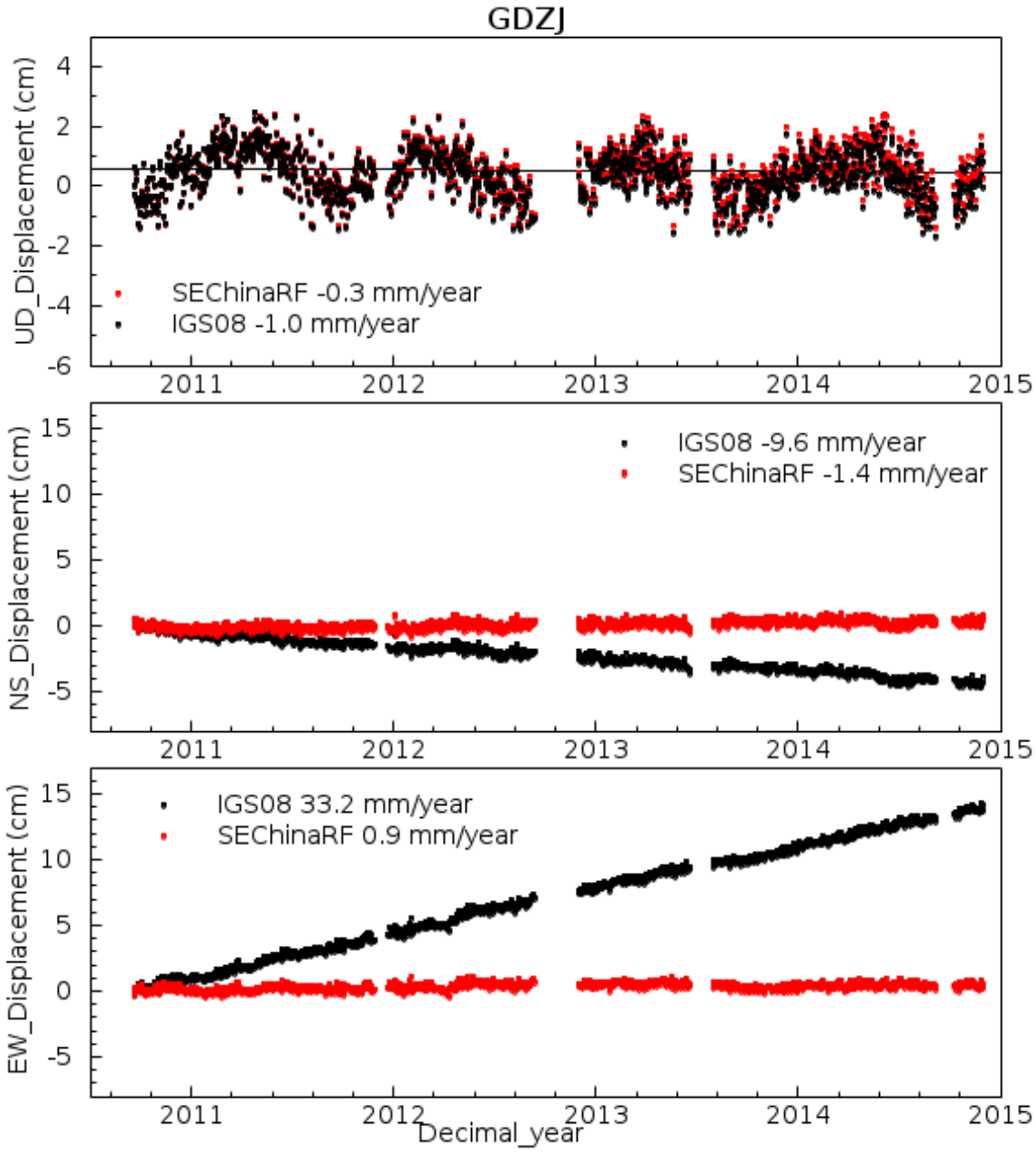

Figure 5-16 Displacement time series at GDZJ (2010-2014) referred to IGS08 (global, red) and SEChinaRF (local, black)

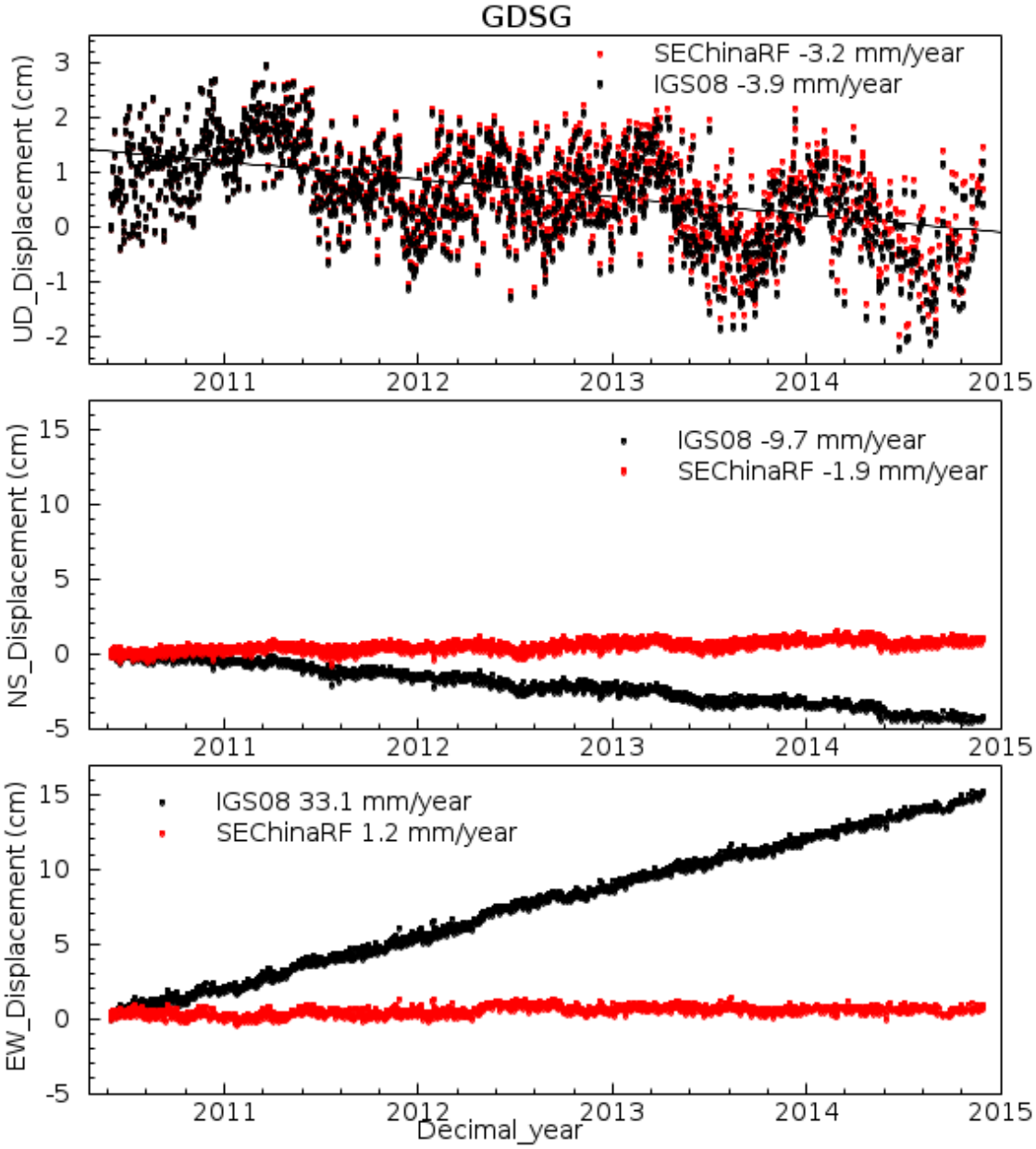

Figure 5-17 Displacement time series at GDSG (2010-2014) referred to IGS08 (global, red) and SEChinaRF (local, black)

Chapter 6 Co-seismic and post-seismic ground deformation induced by the 2011 Tohoku-Oki earthquake in Japan

5.2 Introduction of the 2011 Tohoku-Oki earthquake.

On March 11, 2011, a huge M_W 9.0 megathrust earthquake occurred off the Pacific coast of Tohoku district, northeastern Japan. The Japanese islands are located on the northwest rim of the Pacific Ocean, at the junction of the Pacific, North American, Philippine and Eurasian plates. The plate interface between the Pacific and the overriding continental plates around the Tohoku district is one of the most active areas of seismicity in the world. The earthquake occurred on the subduction zone between the Pacific and North American tectonic plates, in which the Pacific Plate moves westward at a rate of 80 mm/year relative to the Eurasian Plate and eventually plunges underneath the North American Plate.

Figure 6-1 illustrates the tectonic setting of the 2011 Tohoku-Oki earthquake. The earthquake hypocenters shown include earthquakes greater than magnitude 5.0 in the period 1964-2007, and the 2011 Tohoku-Oki earthquake and aftershocks. An earthquake hypocenter is the starting point of the earthquake from which seismic waves travel outward; in the case of larger earthquakes, it is the starting point of slip on a significant portion of a fault plane. In the case of the 2011 Tohoku-Oki earthquake, slip between the plates occurred on the segment of the megathrust fault highlighted in yellow, extending from the cross section through to the northern end of Honshu. The size of the circle represents the magnitude of the

earthquake; the earthquakes shown in green occur deeper than 70 km below the surface.

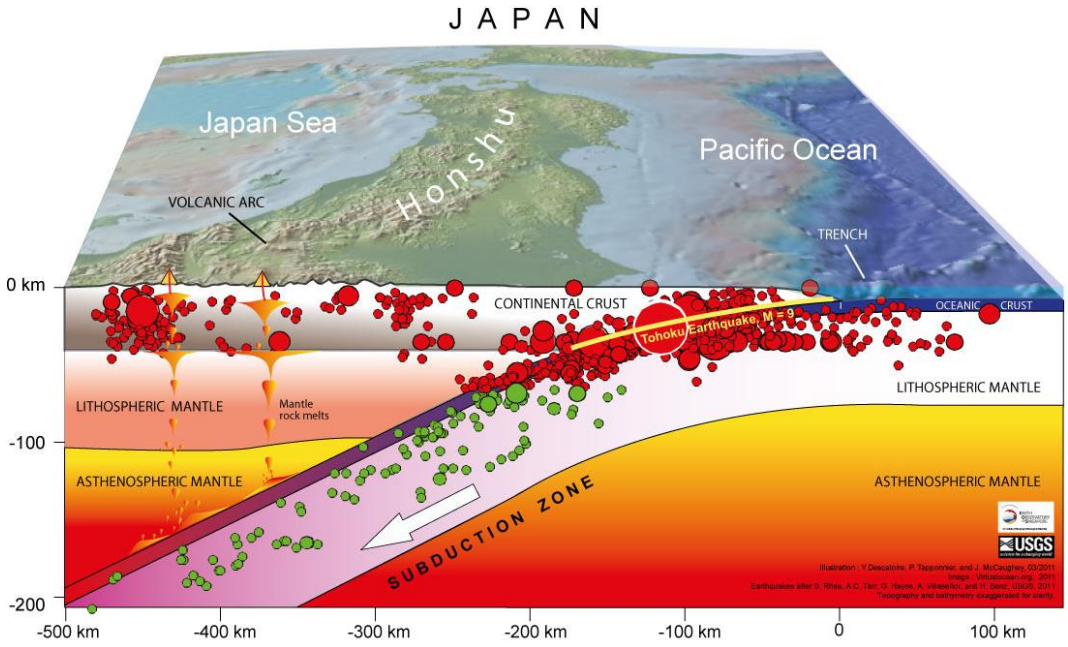

Figure 6-1 The tectonic setting of the 2011 Tohoku-Oki earthquake. The earthquake hypocenters shown include earthquakes greater than magnitude 5.0 in the period 1964-2007, and the 11-March-2011 M 9.0 Tohoku (Japan) earthquake and aftershocks. The yellow line represents the slip between the plates occurred on the segment of the megathrust fault for the 2011 Tohoku-Oki earthquake. The size of the circle represents the magnitude of the earthquake (Source of the figure: Descatoire, 2011)

The epicenter of this earthquake is approximately 70 kilometers east of the Oshika Peninsula of Tohoku and the hypocenter is at an underwater depth of approximately 30 km. It was the most powerful earthquake ever recorded to have occurred in Japan and the fourth most powerful earthquake in the world since modern record keeping began in 1900. The earthquake triggered powerful tsunami waves that reached heights of up to 40.5 meters in Miyako. And it caused an

eastward movement of the northern part of the Honshu Island (the main island of Japan) by as much as 5.3 m (Sato et al., 2011). The Japanese National Police Agency confirmed 15,891 deaths, 6,152 injuries, and 2,584 people missing across twenty prefectures, as well as 228,863 people living away from their home in either temporary housing or in permanent relocation. And its long-term impacts are still under investigations.

5.2 Seismically induced site displacements

Crustal deformation of tectonically active areas is generally described in terms of a cycle that is composed of the following four stages: inter-seismic, pre-seismic, co-seismic, and post-seismic. Sato et al. (2011) studied the co-seismic and post-seismic displacement above the hypocenter of the 2011 Tohoku-Oki earthquake using GPS and acoustic data. A horizontal displacement of 20 meters and a vertical uplift of about 3 meters were observed near the hypocenter. The largest land displacement has been detected at the Oshika peninsula, amounting to about 5 m toward east-southeast (ESE) and about 1 m downward. (Figure 6-2). These co- and post-seismic displacement field obtained from the GPS stations in Japan provides information about near- and intermediate-field deformation. However, how is the far-field co-seismic deformation distributed? What is the scope of its impact? Are the regions of East China affected? If the co-seismic effect exists, in what form does it appear? Investigations to the above questions will not only help to understand the seismogenic structure and spatial distribution of slip

for the Tohoku-oki earthquake, but also are essential in assessing the effect on the earthquake potential in East coast of China.

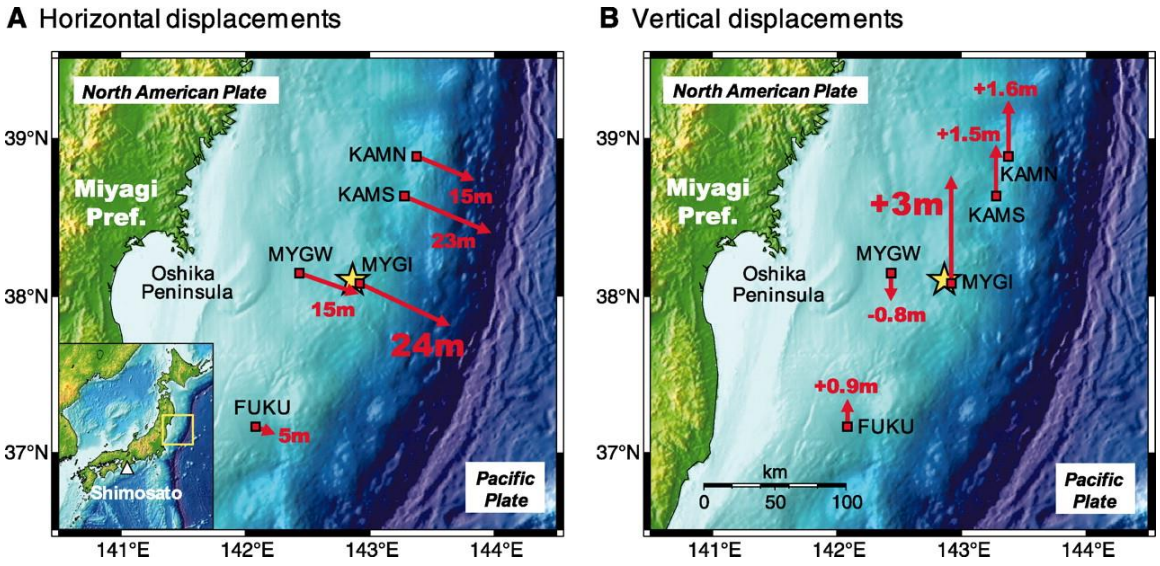

Figure 6-2 Horizontal (A) and vertical (B) co-seismic displacements at the sea-floor reference points, associated with the 2011 Tohoku earthquake. Red squares and a yellow star show locations of sea-floor reference points and the epicenter, respectively. The position reference is Shimosato (Yellow triangle) (Sato et al., 2011)

The China's national key infrastructure project CMONOC provides important data for far-field seismic displacement monitoring, and SEChinaRF provides sufficient accuracy to examine actual co-seismic and post-seismic surface deformation along the China's east coastal region. In this study, the co-seismic and post-seismic ground displacements occurred in three days after the main shock of the earthquake were examined. To determine co-seismic deformation, one approach is to average a short segment of daily data points (~30 days) before and after the event and compute the difference (e.g. Blewitt et al.,

1993; Bock et al., 1993). In this study, this approach was applied to determine the total co-seismic and post-seismic surface deformation of seven selected GPS stations. I used a segment of 60 daily data points before and after the earthquake to calculate the displacements for a higher accuracy. All position coordinates were calculated referred to SEChinaRF.

Table 10 shows the geographic information of the seven GPS stations investigated, including the longitude and latitude coordinates, the distance between the station and the earthquake epicenter, the compass direction of the station referred to the epicenter, the azimuth from the epicenter to each station, and the offset angle, which is defined as the angle in-between the west direction and the line joining the station and the epicenter (Figure 6-3). The offset angle can be calculated by the following equation:

Offset angle = | Azimuth -270| (Unit: °)

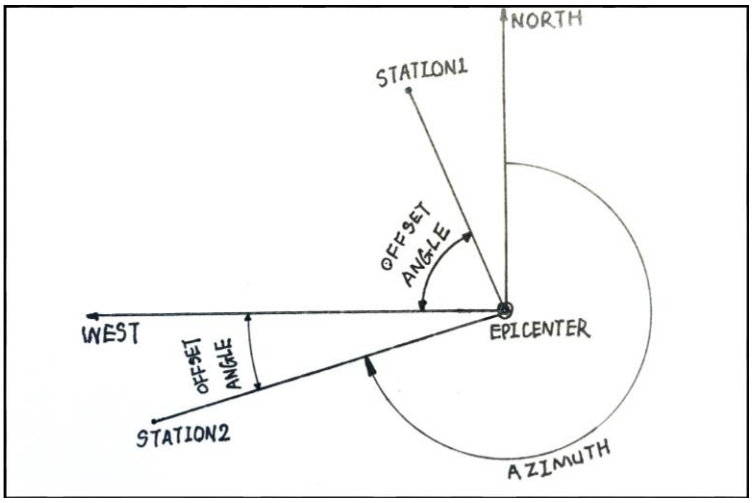

Figure 6-3 the geometry of azimuth and offset angle.

Table 11 shows results of the total horizontal co-seismic and post-seismic displacements in three days (March 11-March 13, 2011) after the main shock. It

can be found that: (1) for most stations (except KHAJ), the total horizontal displacement of a station has a positive correlation with the distance between the station and earthquake epicenter, and (2) the NS displacement shows a positive relationship with the offset angle. Figure 6-4 shows the relationship between the total horizontal displacement and the distance from the epicenter of each station. Figure 6-5 shows the relationship between the NS displacement and the offset angle.

Table 6-1 Geographic information of the seven selected GPS stations.

Station	longitude(°)	latitude (°)	Distance from the earthquake epicenter (Km)	Compass direction from the earthquake epicenter	Azimuth from the earthquake epicenter (Az., °)	Offset angle (°)
KHAJ	135.05	48.52	1277.49	NNW	334	64
CHAN	125.44	43.79	1540.34	WNW	298	28
QYLU	120.45	36.14	1955.82	W	269	1
XIAO	120.30	36.08	1969.93	W	269	1
BJFS	115.89	39.61	2290.83	WNW	281	11
SHAO	121.20	31.10	2091.97	WSW	253	17
HKOH	114.23	22.25	3220.15	WSW	244	26

Table 6-2 The geographic information and total horizontal co-seismic and post-seismic displacements in three days (March 11-March 13, 2011) after the main shock of the 2011 Tohoku earthquake of seven GPS stations along the east coastal region of China

Station	Distance from the earthquake epicenter (Km)	Offset angle (°)	Total EW component displacement (mm)	Standard deviation of EW displacement (mm)	Total NS component displacement (mm)	Standard deviation of NS displacement (mm)	Total horizontal displacement (mm)	Standard deviation of EW displacement (mm)
KHAJ	1277.49	64	10.72	2.06	-12.36	2.23	16.37	2.18
CHAN	1540.34	28	19.89	2.44	-7.45	1.80	21.25	3.03
QYLU	1955.82	1	10.92	2.56	-1.14	2.43	10.98	3.53
XIAO	1969.93	1	11.75	2.44	1.48	1.85	11.85	3.06
SHAO	2091.97	17	5.45	2.40	3.76	2.37	6.63	3.37
BJFS	2290.83	11	8.85	2.32	-0.07	2.01	8.85	3.07
HKOH	3220.15	26	0.53	2.83	-3.03	2.62	3.08	3.86

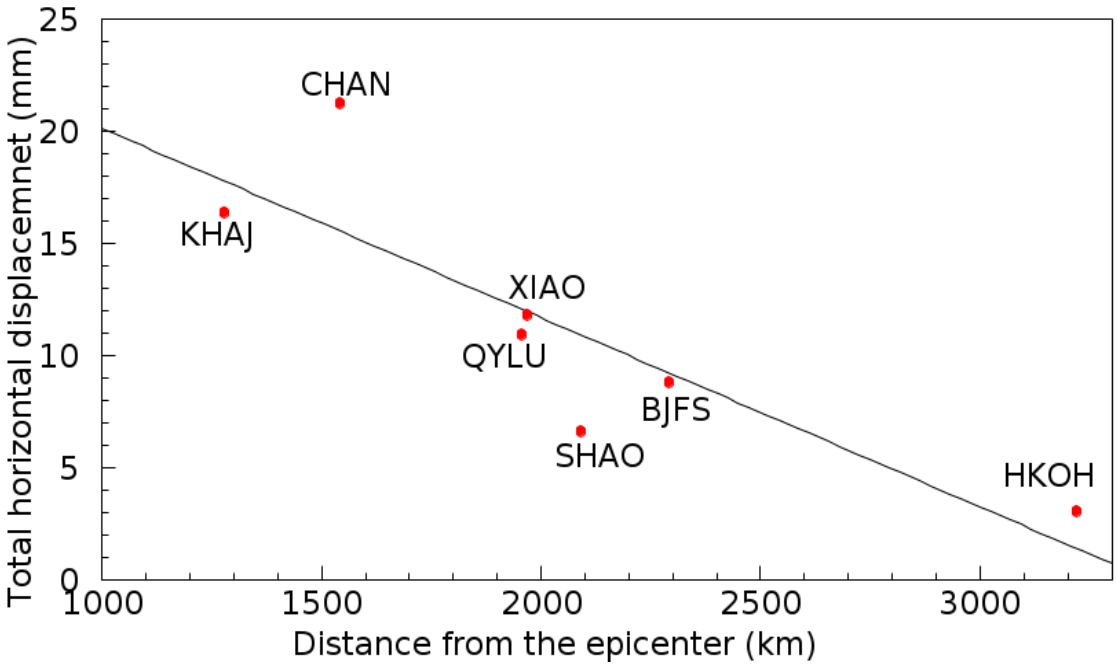

Figure 6-5 Figure showing the relationship between the total horizontal displacement and the distance from the epicenter of each station

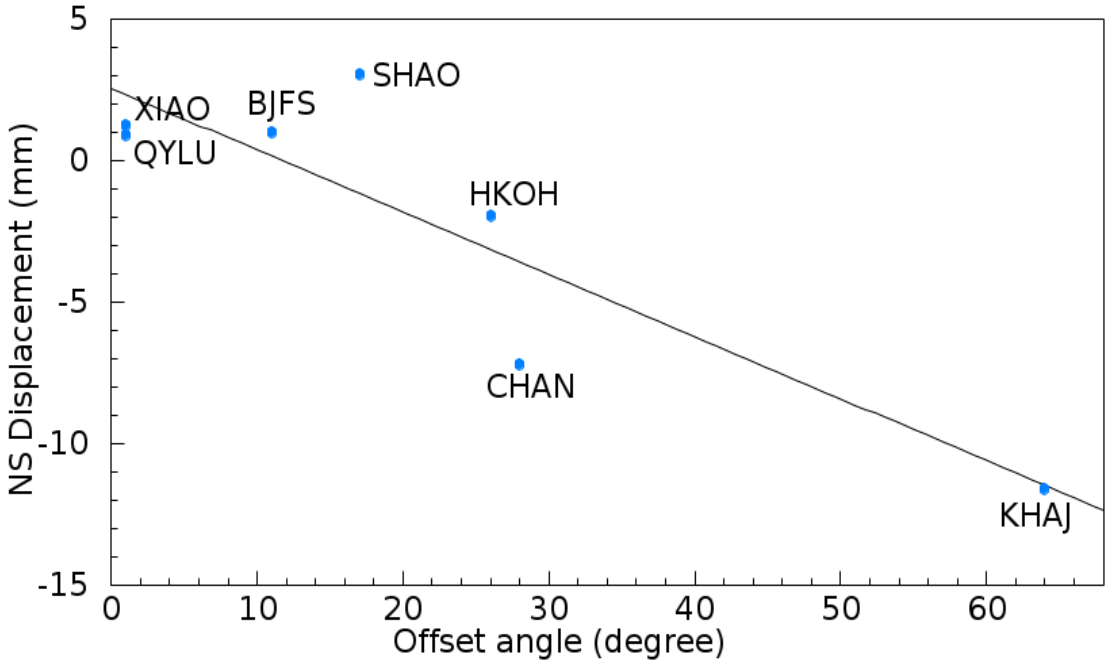

Figure 6-4 Plot showing the relationship between the NS displacement and the offset angle.

Figure 6-7 shows total co-seismic and post-seismic horizontal displacement vectors induced by the 2011 Tohoku earthquake at seven GPS stations along the east coast of China. The error ellipses represent 90% confidence.

Station KHAJ is located north northwest to the earthquake epicenter. Figure 6-7 illustrated the comparison of EW and NS components of the co- and post-seismic displacement time series at KHAJ referred to SEChinaRF. The NS displacement was 12.36 mm southward. It was larger than the EW displacement, which was 10.72 mm. It indicated that the earthquake energy arrived at KHAJ had greater NS component energy than EW component. And this resulted from that the offset angle of KHAJ (64 °) was considerable large.

Station CHAN is located west northwest to the earthquake epicenter. Figure 6-8 illustrated the comparison of EW and NS components of the co- and post-seismic displacement time series at CHAN referred to SEChinaRF. The NS displacement was 7.45 mm southward. It was smaller than the EW displacement, which was 19.89 mm eastward. The total displacement was 21.25 mm, which was the largest displacement observed among these seven GPS stations.

Figures 6-9, 6-10, and 6-11 illustrated the co- and post-seismic displacement time series at BJFS, QYLU and XIAO referred to SEChinaRF. For these three stations, which located west to the earthquake epicenter, the total co- and post-seismic EW component displacements ranged from 8.85-10.92 mm, and no considerable NS component displacement (greater than 1.5 mm) was recorded. From the geometry of the station’s positions, it can be found that the arriving

earthquake energy were primarily propagated from the east of these stations. Therefore, only EW displacements were induced.

Station SHAO is located west southwest to the earthquake epicenter. Figure 6-12 illustrate the co- and post-seismic displacement time series at SHAO referred to SEChinaRF. Both NS and EW displacement were recorded, which were 3.76 mm and 5.45 mm, respectively. The total displacement at SHAO was 6.63 mm. It was smaller than the total displacement at the stations located in northeast of China, because the distance between SHAO and the earthquake epicenter is considerably large.

Station HKOH is located at a long distance from the earthquake epicenter, consequently, no considerable horizontal displacements were recorded at HKOH. Figure 6-13 illustrated the co- and post-seismic displacement time series at HKOH referred to SEChinaRF

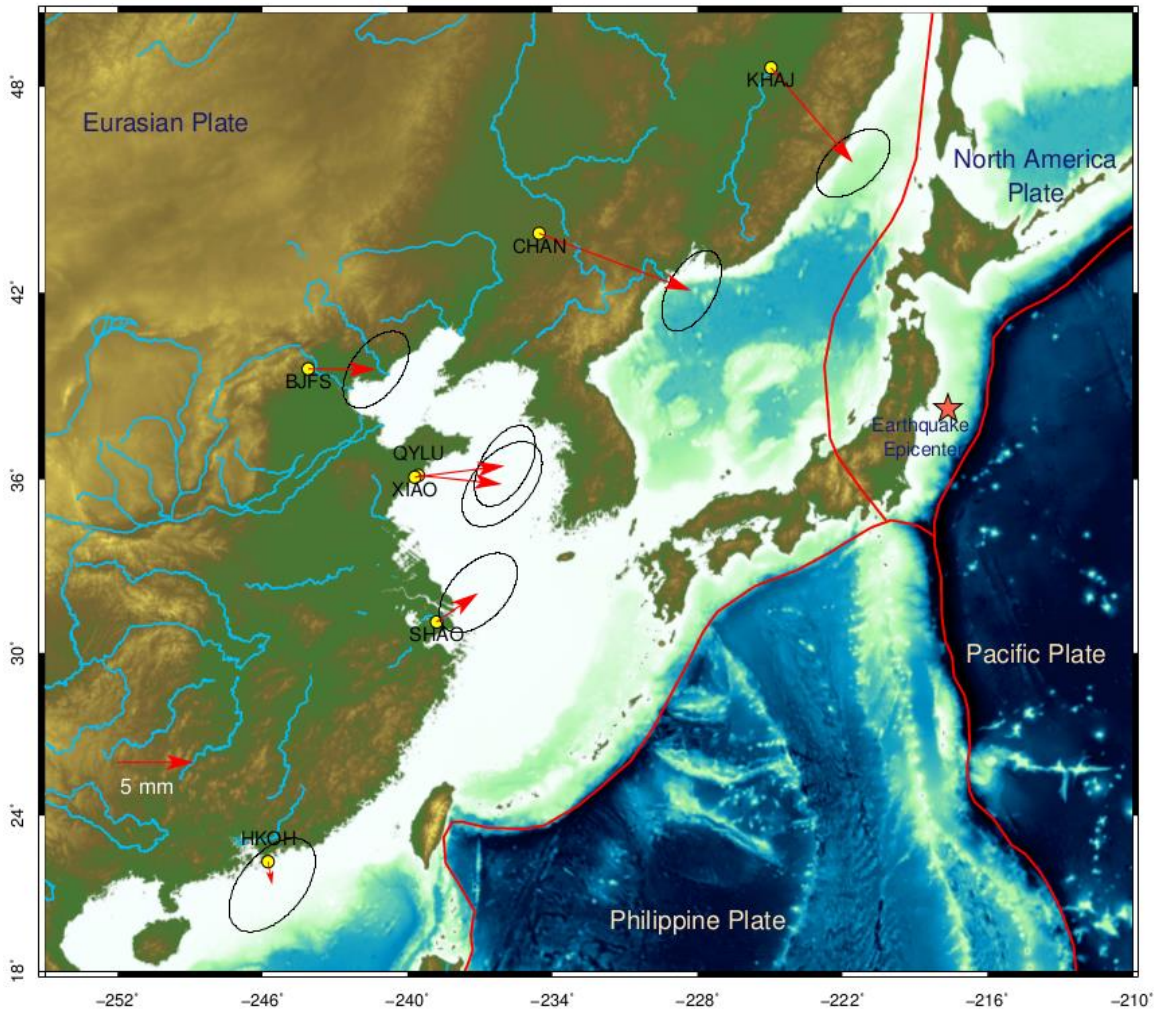

Figure 6-6 Total co- and post-seismic horizontal displacement vectors (with respect to SEChinaRF) at seven GPS stations in three days (03/11/2011-03/13/2011) after the main shock. The error ellipses represent 90% confidence.

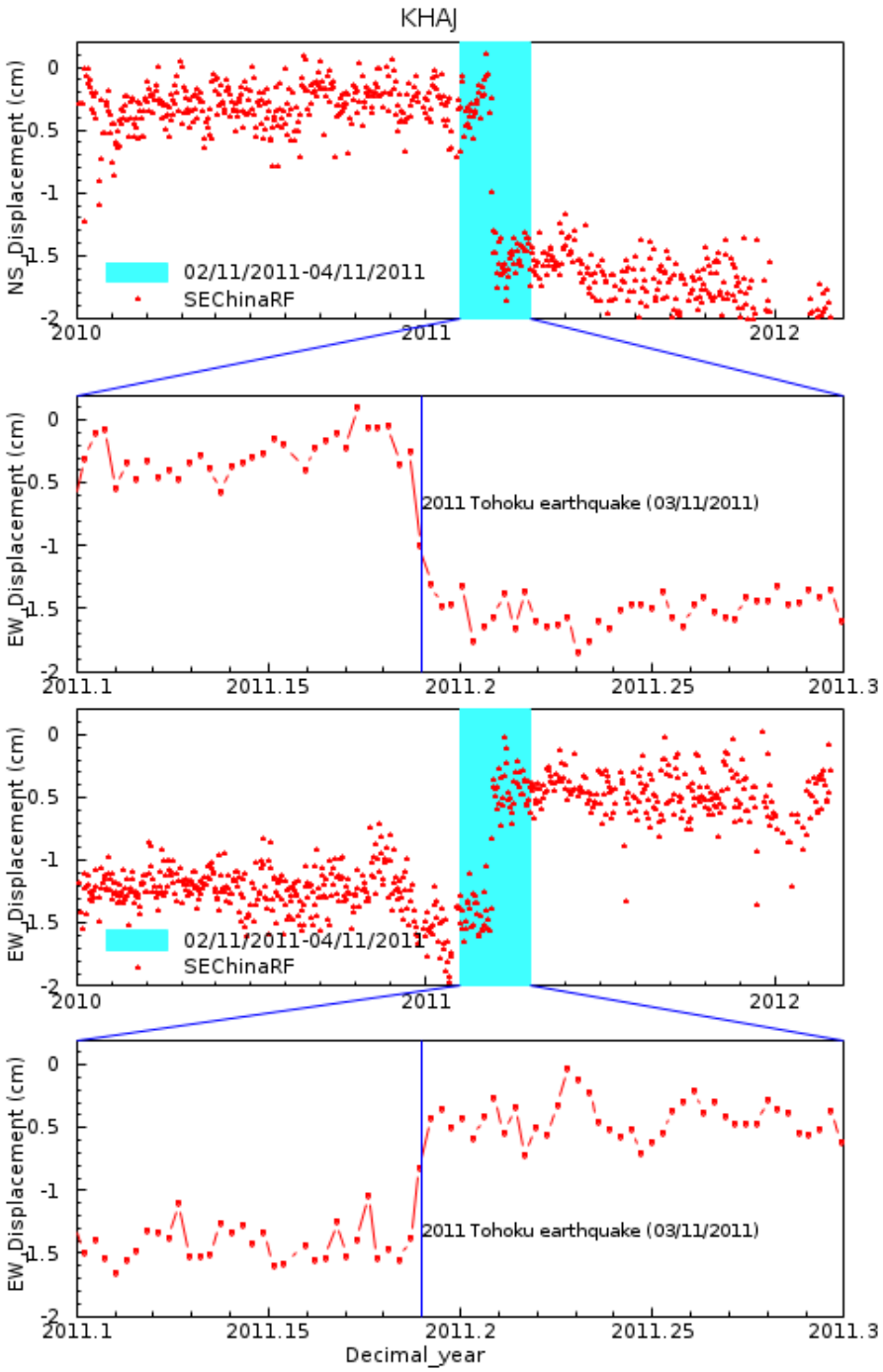

Figure 6-7 Comparison of EW and NS components of the co- and post-seismic displacement time series at KHAJ referred to SEChinaRF. Both the EW and NS components of displacement are zoomed in within a time span of February 2011 to April 2011.

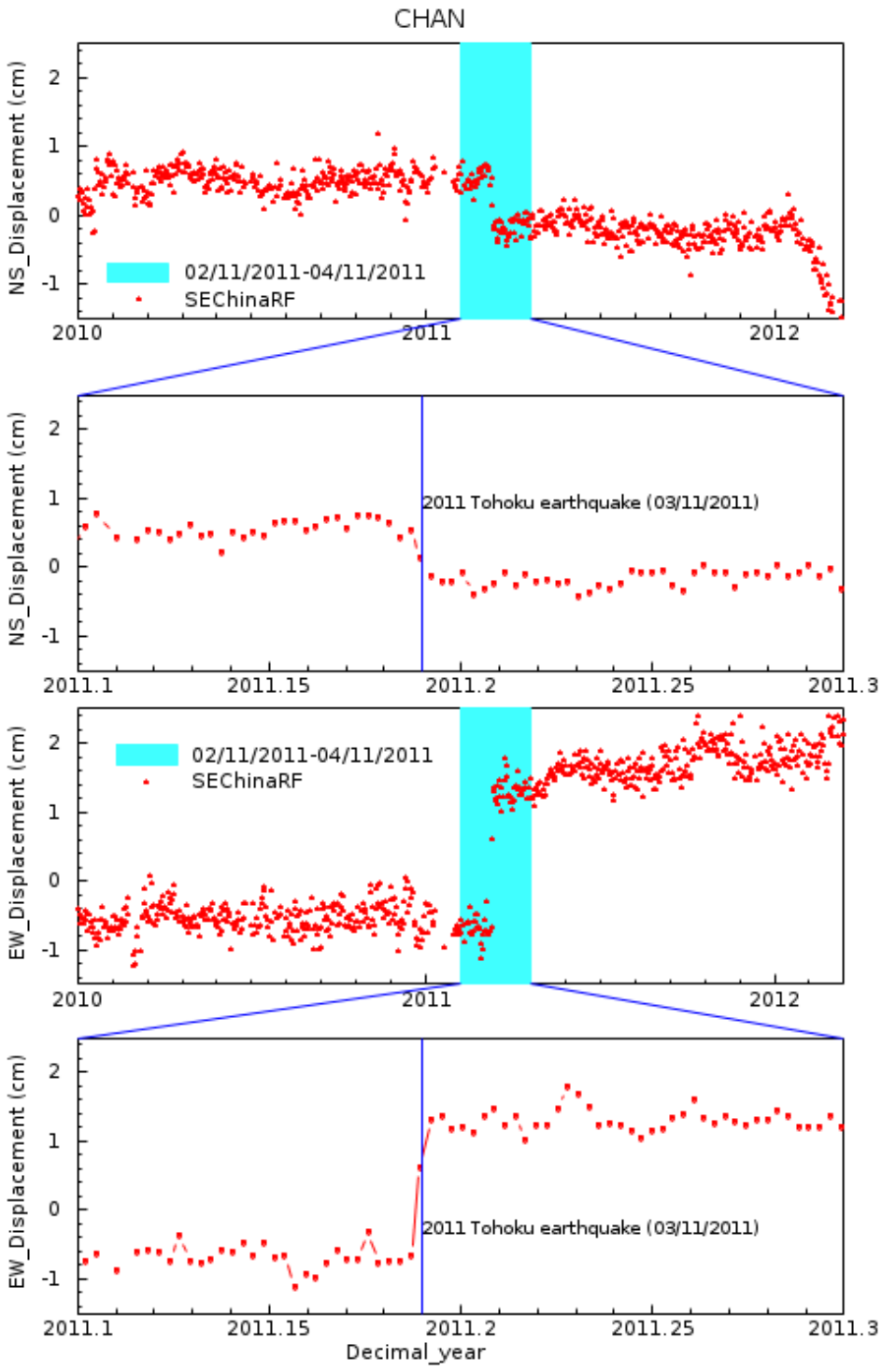

Figure 6-8 Comparison of EW and NS components of the co- and post-seismic seismic displacement time series at KHAJ referred to SEChinaRF. Both the EW and NS components of displacement are zoomed in within a time span of February 2011 to April 2011.

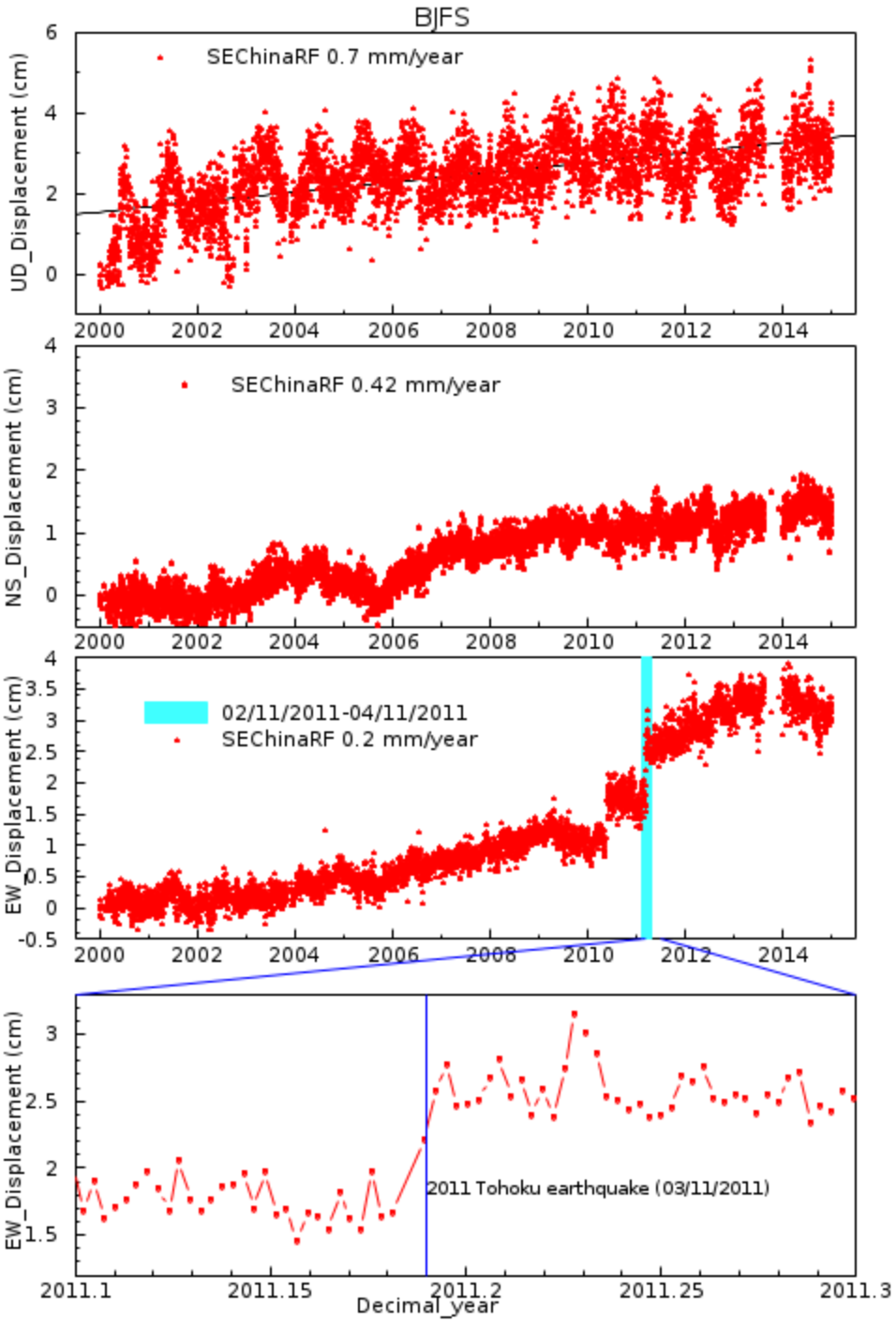

Figure 6-9 Plots showing the co- and post-seismic displacement time series at BJFS referred to SEChinaRF. In the bottom plot, the EW component of displacement is zoomed in within a time span from February 2011 to April 2011.

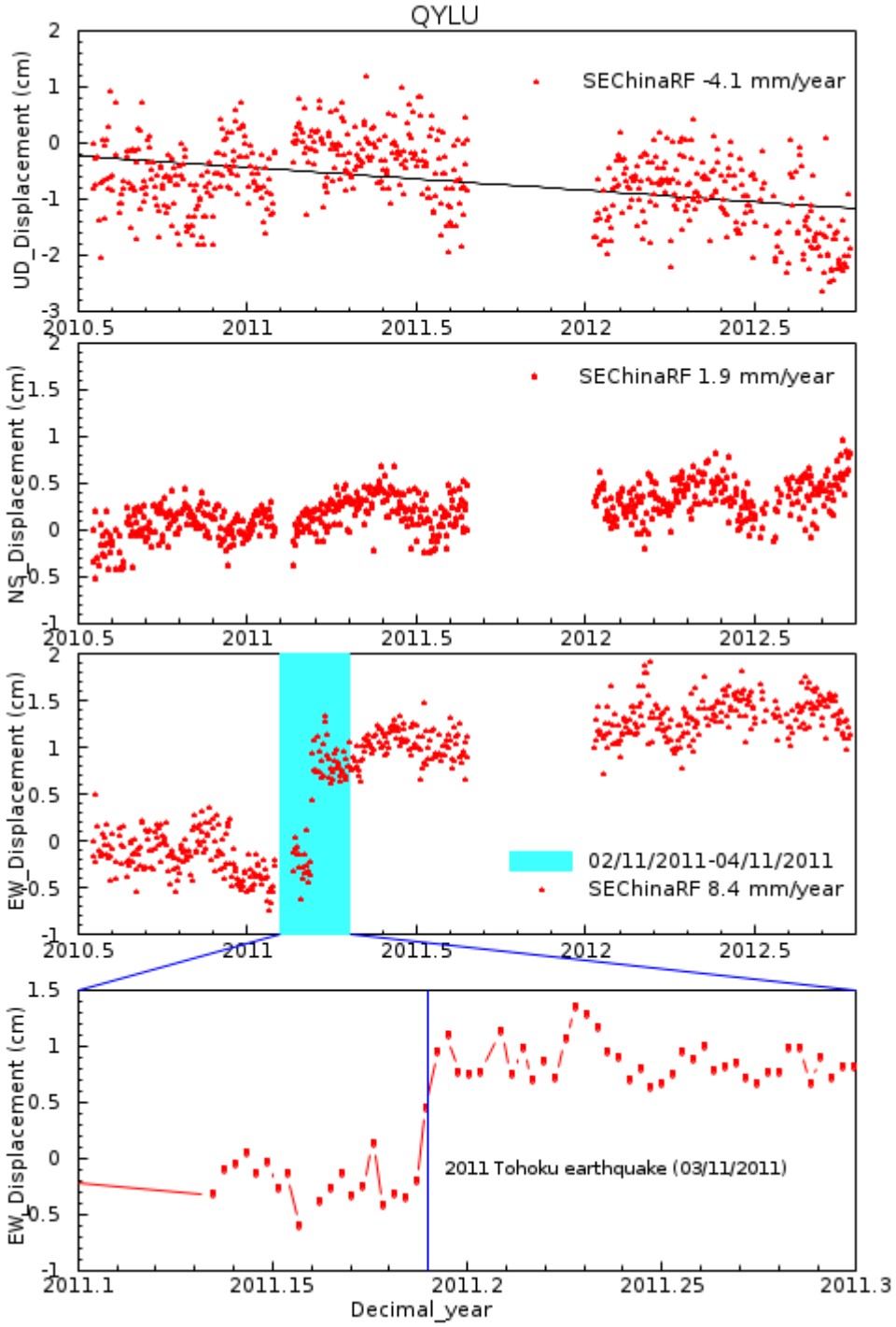

Figure 6-10 Plots showing the co-and post-seismic displacement time series at QYLU referred to SEChinaRF. In the bottom plot, the EW component of displacement is zoomed in within a time span from February 2011 to April 2011.

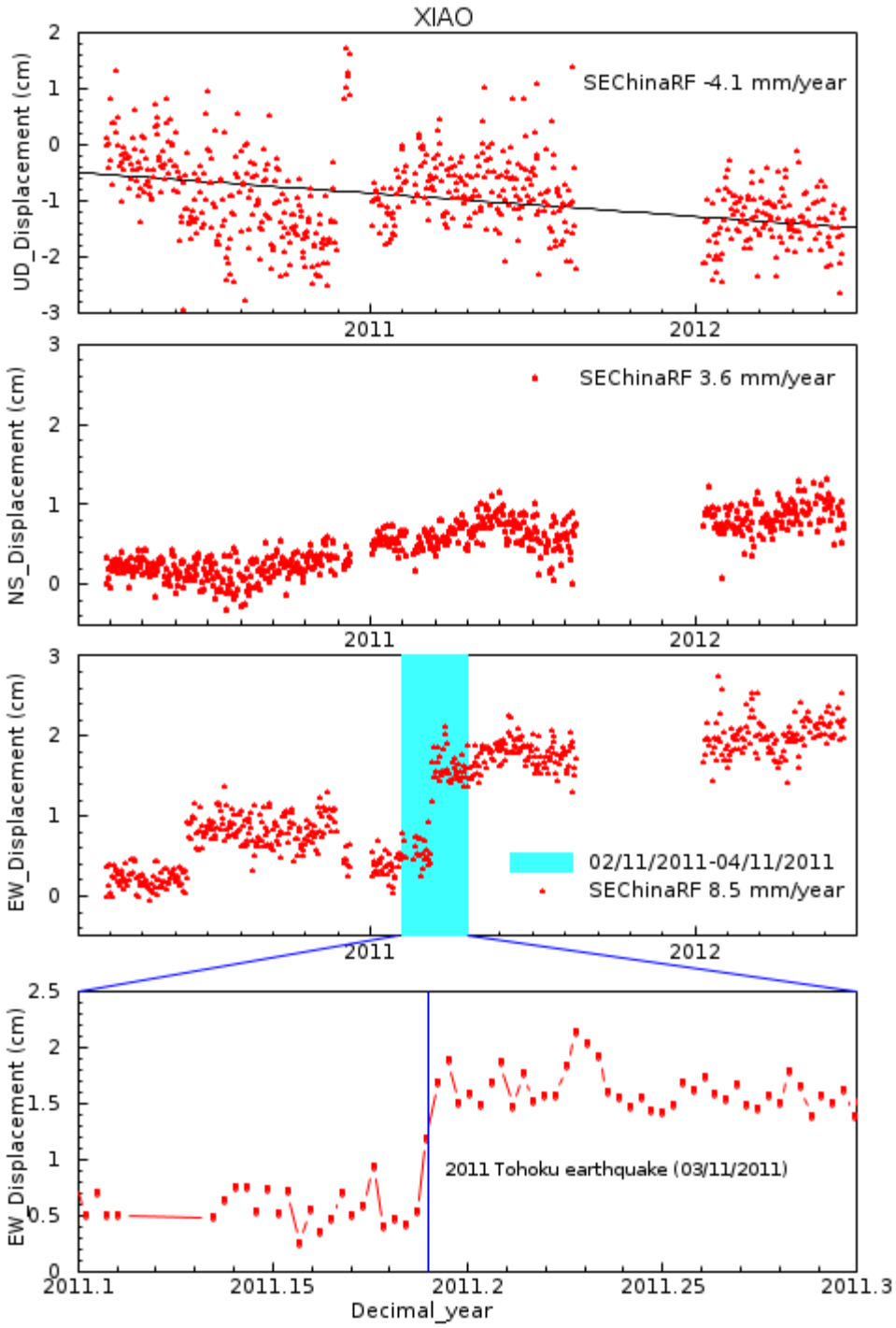

Figure 6-11 Plots showing the co- and post-seismic displacement time series at XIAO referred to SEChinaRF. In the bottom plot, the EW component of displacement is zoomed in within a time span from February 2011 to April 2011.

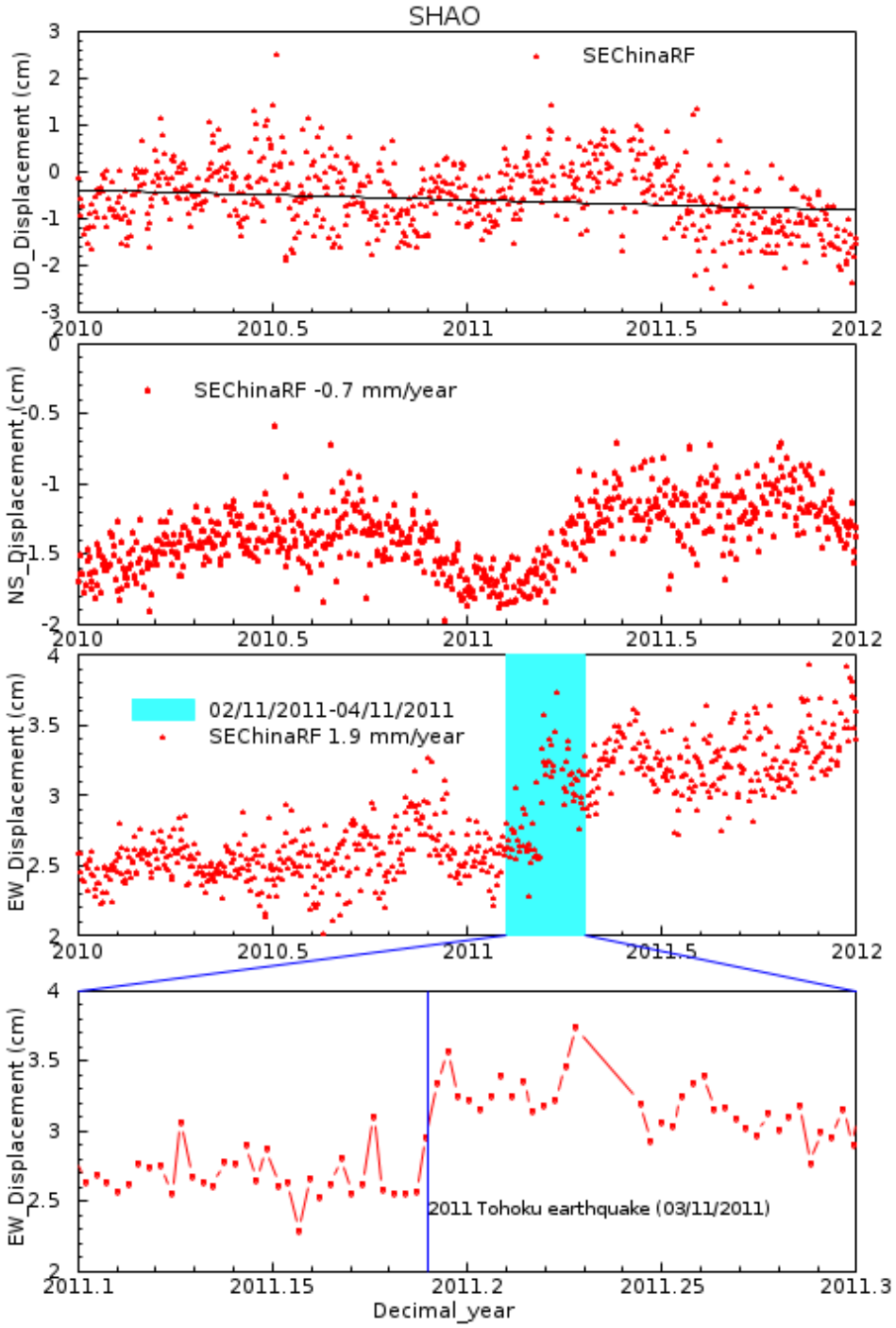

Figure 6-12 Plots showing the co- and post-seismic displacement time series at SHAO referred to SEChinaRF. In the bottom plot, the EW component of displacement is zoomed in within a time span from February 2011 to April 2011.

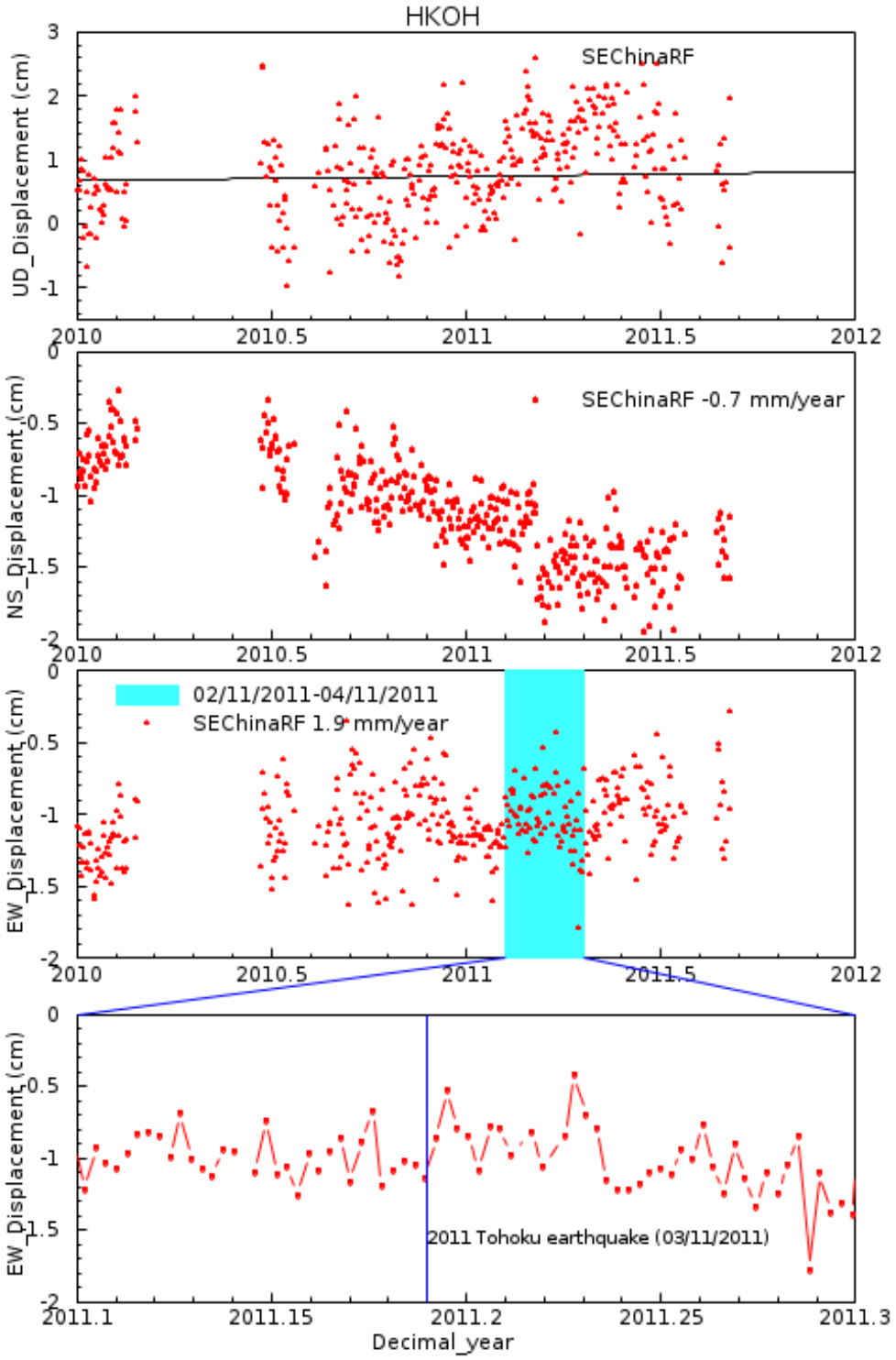

Figure 6-13 Plots showing the co- and post-seismic displacement time series at HKOH referred to SEChinaRF. In the bottom plot, the EW component of displacement is zoomed in within a time span of February 2011 to April 2011.

5.3 Seismically induced site velocity changes

The velocity changes of five GPS stations which have continuously collected data for over seven years are investigated in this part. Table 6-3 shows the velocities of the two horizontal components (EW and NS) recorded at the five stations before and after the 2011 Tohoku-Oki earthquake, and the velocity changes. SHAO and HKOH are located in the southern part of China, and there are considerable distances (2092 km and 3220 km, respectively) between these two stations and the earthquake epicenter. Consequently, they were not significantly influenced by the 2011 Tohoku-Oki earthquake, and the small velocity changes before and after the earthquake could be resulted from other factors. For stations BJFS, it lies in Beijing, north China, and it is 2291 km away from the earthquake epicenter. Therefore, the velocity changes of both EW and NS components were considerably small.

Figure 6-14 shows the horizontal displacement time series of station CHAN (2005-2015) and the velocity changes before and after the Tohoku-Oki earthquake referred to SEChinaRF. CHAN is relatively close (1540 km) to the earthquake epicenter. For EW component, it was moving 0.78 mm/year westward before the earthquake, and 1.94 mm/year eastward after the earthquake. The EW velocity change induced by the 2011 Tohoku-Oki earthquake was 2.72 mm/year toward east. There is no considerable NS velocity change recorded at CHAN.

Figure 6-15 shows the horizontal displacement time series of station KHAJ (2005-2015) and the velocity changes before and after the Tohoku-Oki earthquake

referred to SEChinaRF. KHAJ is located 1277 km away from the earthquake epicenter and in the north northwest direction of the epicenter. In figure 6-14, we can find that, the NS velocity was -0.52 mm/year southward before the earthquake and -5.87 mm/year southward after the earthquake. The NS velocity change is as large as -5.35 mm/year. The EW velocity change at KHAJ is considerably small. The relatively large NS velocity change is primarily due to its short distance and large azimuth (334°) to the earthquake epicenter.

Table 6-3 Horizontal velocities of five stations and the velocities changes before and after the 2011 Tohoku-Oki earthquake.

Site ID	NS_velocity (Before 2011) (mm/year)	NS_velocity (After June 2011) (mm/year)	NS_velocity_change (mm/year)	EW_velocity (Before 2011) (mm/year)	EW_velocity (After June 2011) (mm/year)	EW_velocity_change (mm/year)
KHAJ	-0.64	-5.87	-5.23	-0.40	-1.09	-0.69
CHAN	1.38	1.17	-0.21	-0.78	1.94	2.72
BJFS	1.28	1.06	-0.22	1.43	1.44	0.01
SHAO	-1.08	1.59	2.67	1.47	2.62	1.15
HKOH	-1.31	0.94	2.25	-1.14	1.36	2.5

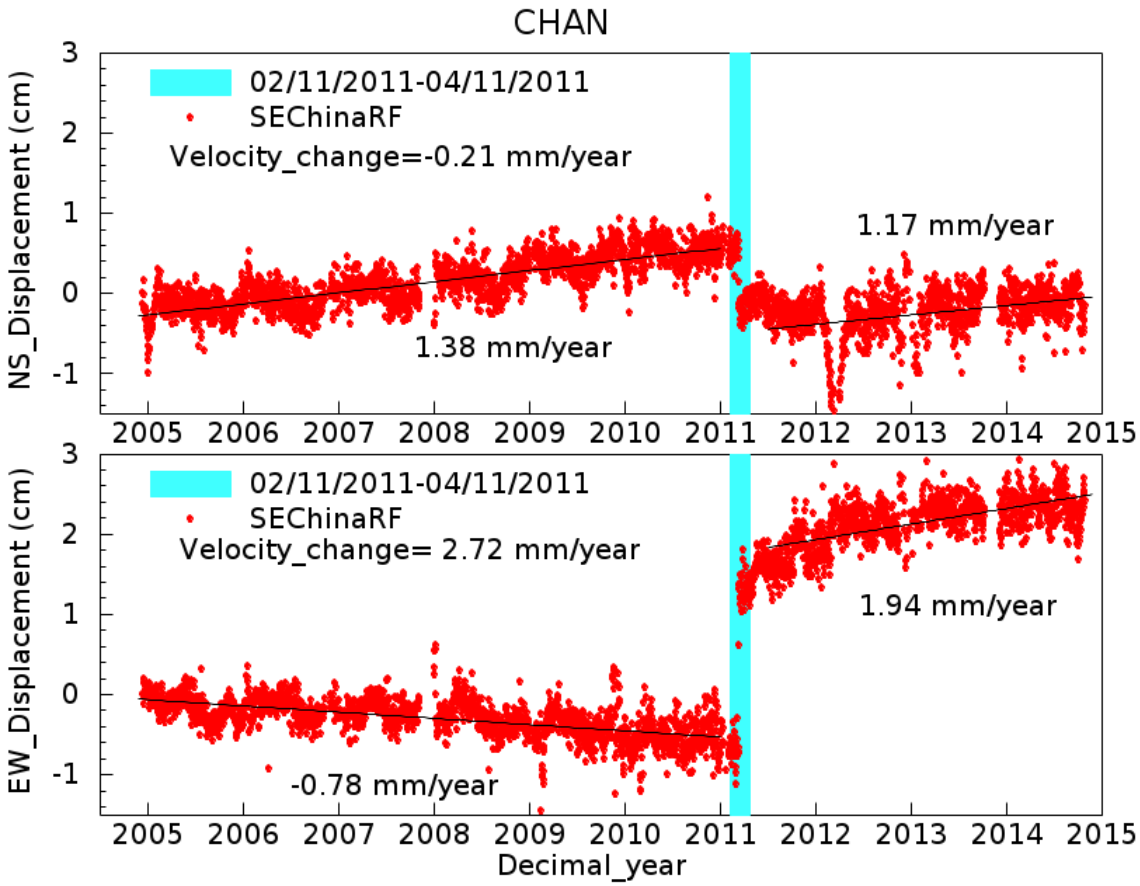

Figure 6-14 Plots showing the horizontal displacement time series of station CHAN (2005-2015) and the velocity changes before and after the Tohoku-Oki earthquake referred to SEChinaRF.

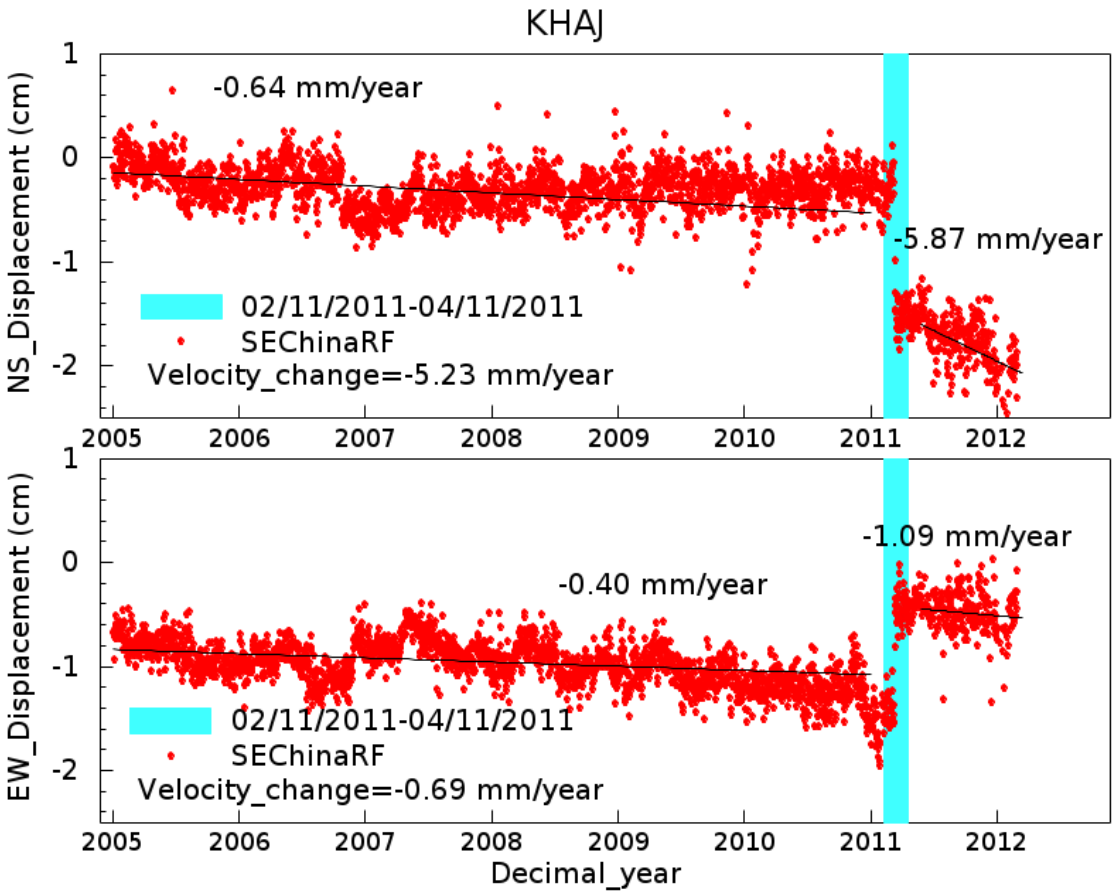

Figure 6-15 Plots showing the horizontal displacement time series of station KHAJ (2001-2012) and the velocity changes before and after the Tohoku-Oki earthquake referred to SEChinaRF.

Chapter 7 Discussion and Conclusions

In this study, ground deformation that recently occurred along the east coastal region of China was investigated based on the GPS measurements. The GPS data were collected from over 100 GPS stations of CMONOC and other organizations, and processed by the GIPSY-OAISIS (V6.3) software package in precise point positioning (PPP) mode. Precise point positioning method was able to produce the position coordinates of each GPS station within a global reference frame (IGS08) with millimeter to centimeter accuracy. These coordinates need to be transferred to a local reference frame to examine the magnitude and direction of local displacements over time.

In chapter 3, a Stable East China Reference Frame (SEChinaRF) was established based on the measurement of five permanent GPS stations, which are located throughout the east coastal region of China, and have been continuously collecting data for at least 7 years. The realization of SEChinaRF is based on a Helmert transformation from the International GNSS (Global Navigation Satellite System) Reference Frame of 2008 (IGS08). SEChinaRF is aligned with the IGS08 at epoch 2013.0. The velocities of these 5 reference stations are minimized to zero or near zero within the stable local reference frame. Within SEChinaRF, the average repeatability (RMS) of PPP solutions is approximately 2-4 mm in the horizontal directions and 7-8 mm in the vertical direction, which are consistent with the accuracy of PPP daily solutions within IGS08. The fourteen parameters for reference frame transformation from IGS08 to SEChinaRF were provided.

SEChinaRF will serve a broad of geoscientific and geodetics study purposes, such as land subsidence, local ground deformation, and co-seismic deformation.

In chapter 4, land subsidence that currently occurred in the Tianjin area from 2010-2014 was studied using GPS data. There are four GPS stations distributed in this area: TJBD, TJBH, TJWQ and HECX, of which the subsidence rates are -1.9 mm/year, -19.4 mm/year, -45.6 mm/year and -21.4 mm/year, respectively. The pattern of land subsidence in Tianjin was compared with the subsidence recorded at three stations in Mississippi Delta, where steady subsidence with an average rate of 4 mm/year occurred during 2002-2012. Through the comparison, it is founded that the subsidence in the Tianjin area was most likely to be caused by human activities instead of tectonic motions. The major driving factor for the current subsidence in Tianjin was determined to be the excessive groundwater withdrawal. And the subsidence rates varying largely even within a small area could be caused by the varied volume of groundwater withdrawal near each GPS station.

In chapter 5, land subsidence in other areas along the China's east coastal region were investigated and analyzed referred to SEChinaRF. Such cities and provinces include Shandong, Shanghai, and Guangdong. In Shandong province, most of the stations (LAIX, TIAN, JIMO, QYLU, XIAO and JNAN) presented steady land subsidence with rates between 2.9 mm/year and 4.9 mm/year from 02/2010 to 08/2012. One exception was HDAO, which recorded 11.3 mm/year subsidence during the same time span. The driving factors of land subsidence in Shandong

still need to be examined. In Shanghai, the vertical displacement time series of SHAO was comprised of two periods, 1997-2004 and 2004-2014. The subsidence rates of these two periods were 0.9 mm/year and -2.2 mm/year, respectively. This indicated that the ground surface in this area has experienced a slow subsidence since 2004. In Guangdong province, different patterns of land subsidence were recorded are three stations: GDST, GDSG and GDZJ during 2010 to 2014, with subsidence rates of 13.9 mm/year, 3.2 mm/year, and 1.3 mm/year, respectively.

The great Tohoku-Oki earthquake that occurred off the Pacific coast of Japan caused rapid ground deformation to the surrounding areas. The co- and post-seismic displacements induced by this earthquake were recorded by most of the GPS stations in the northeast China. In chapter 6, I investigated the displacement time series of seven GPS stations, aiming to understand far-filed the surface deformation associated with the Tohoku-Oki earthquake. The results revealed that the co- and post-seismic horizontal displacements were at the level of millimeters to centimeters in Northeast China, with a maximum of 21 mm at CHAN, and the total horizontal displacement at the GPS stations had a positive correlation with the distance between the each station and the earthquake epicenter. Meanwhile, the term, offset angle, was defined as the angle between the west direction and the line joining the station and the earthquake epicenter in this study. It is founded that the NS displacements recorded at each station showed a positive relationship with the offset angles. Seismically induced site velocity changes of five long-history stations were examined. Relatively large

horizontal velocity changes before and after the earthquake were observed; at CHAN, velocity change was 2.72 mm/year eastward, and at KHAJ, velocity change was 5.23 mm/year southward. The magnitude and direction of velocity changes were determined to be associated with the distance and azimuth to the earthquake epicenter.

References Cited

Anderle, R. J. (1976). Point positioning concept using precise ephemeris. In Satellite Doppler Positioning. 1, 47-75.

Abidin, H. Z., Djaja, R., Darmawan, D., Hadi, S., Akbar, A., Rajiyowiryono, H., Sudibyo, Y., Meilano, I., Kasuma, M., Kahar, J., & Subarya, C. (2001). Land subsidence of Jakarta (Indonesia) and its geodetic monitoring system. Natural Hazards, 23(2-3), 365-387.

Abidin, H. Z., Andreas, H., Djaja, R., Darmawan, D., & Gamal, M. (2008). Land subsidence characteristics of Jakarta between 1997 and 2005, as estimated using GPS surveys. GPS Solutions, 12(1), 23-32.

Bar-Sever, Y. E., Kroger, P. M., & Borjesson, J. A. (1998). Estimating horizontal gradients of tropospheric path delay with a single GPS receiver. Journal of Geophysical Research: Solid Earth (1978–2012), 103(B3), 5019-5035.

Bertiger, W., Desai, S. D., Haines, B., Harvey, N., Moore, A. W., Owen, S., & Weiss, J. P. (2010). Single receiver phase ambiguity resolution with GPS data. Journal of Geodesy, 84(5), 327-337.

Blewitt, G. (1989). Carrier phase ambiguity resolution for the Global Positioning System applied to geodetic baselines up to 2000 km. Journal of Geophysical Research: Solid Earth (1978–2012), 94(B8), 10187-10203.

Blewitt, G., Heflin, M. B., Hurst, K. J., Jefferson, D. C., Webb, F. H., & Zumberge, J. F. (1993). Absolute far-field displacements from the 28 June 1992 Landers earthquake sequence. Nature, 361(6410), 340-342.

Blewitt, G., & Lavallee, D. (2002). Effect of annual signals on geodetic velocity. Journal of Geophysical Research: Solid Earth (1978–2012), 107(B7), ETG-9.

Boehm, J., Werl, B., & Schuh, H. (2006). Troposphere mapping functions for GPS and very long baseline interferometry from European Centre for Medium‐Range Weather Forecasts operational analysis data. Journal of Geophysical Research: Solid Earth (1978–2012), 111(B2).

Bock, Y. (1991). Continuous monitoring of crustal deformation. GPS World, 2(6), 40-47.

Burkett, V. R., Zilkoski, D. B., & Hart, D. A. (2002). Sea-level rise and subsidence: implications for flooding in New Orleans, Louisiana. In US Geological Survey Subsidence Interest Group Conference: Proceedings of the Technical Meeting, Galveston, Texas, 27-29 November 2001, 63-71.

Chai, J. C., Shen, S. L., Zhu, H. H., & Zhang, X. L. (2004). Land subsidence due to groundwater drawdown in Shanghai. Geotechnique, 54(2), 143-147.

Choy, S., Silcock, D., & Zhang, K. (2009). Single frequency precise point positioning using a low-cost GPS receiver. In Surveying & Spatial Sciences Institute Biennial International Conference, 1-14.

Collilieux, X., Altamimi, Z., Coulot, D., Ray, J., & Sillard, P. (2007). Comparison of very long baseline interferometry, GPS, and satellite laser ranging height residuals from ITRF2005 using spectral and correlation methods.Journal of Geophysical Research: Solid Earth (1978–2012), 112(B12).

Dokka, R. K., Sella, G. F., & Dixon, T. H. (2006). Tectonic control of subsidence

and southward displacement of southeast Louisiana with respect to stable North America. Geophysical Research Letters, 33(23).

Dokka, R. K. (2011). The role of deep processes in late 20th century subsidence of New Orleans and coastal areas of southern Louisiana and Mississippi. Journal of Geophysical Research: Solid Earth (1978–2012), 116(B6).

Duan, Y. (1998). Research status on land subsidence and sustainable development in the 21st century of China. The Chinese Journal of Geological Hazard and Control, 9(2), 1-5.

Erkens, G., Bucx, T., Dam, R., De Lange, G., & Lambert, J. (2014). Sinking coastal cities. In EGU General Assembly Conference Abstracts, 16, 14606.

Ferronato, M., Gambolati, G., Teatini, P., & Baù, D. (2006). Stochastic poromechanical modeling of anthropogenic land subsidence. International journal of solids and structures, 43(11), 3324-3336.

Gao, X., Ma, X., & Li, X. (2011). The great triangular seismic region in eastern Asia: Thoughts on its dynamic context. Geoscience Frontiers, 2(1), 57-65.

Gao, Y., & Chen, K. (2004). Performance analysis of precise point positioning using rea-time orbit and clock products. Positioning, 1(08), 0.

Holla, L., & Barclay, E. (2000). Mine subsidence in the southern coalfield, NSW, Australia. Department of Mineral Resources.

Holzer, T. L., & Johnson, A. I. (1985). Land subsidence caused by ground water withdrawal in urban areas. GeoJournal, 11(3), 245-255.

Hu, B., Zhou, J., Wang, J., Chen, Z., Wang, D., & Xu, S. (2009). Risk assessment of land subsidence at Tianjin coastal area in China. Environmental Earth Sciences, 59(2), 269-276.

Hu, R. L., Yue, Z. Q., Wang, L. U., & Wang, S. J. (2004). Review on current status and challenging issues of land subsidence in China. Engineering Geology, 76(1), 65-77.

Jin, S., & Komjathy, A. (2010). GNSS reflectometry and remote sensing: New objectives and results. Advances in Space Research, 46(2), 111-117.

Jonsson, S., Zebker, H., Segall, P., & Amelung, F. (2002). Fault slip distribution of the 1999 Mw 7.1 Hector Mine, California, earthquake, estimated from satellite radar and GPS measurements. Bulletin of the Seismological Society of America, 92(4), 1377-1389.

Kaneko, S., and Toyota, T. (2011). Long-term urbanization and land subsidence in Asian Megacities: An indicators system approach. In Groundwater and Subsurface Environments (pp. 249-270). Springer Japan.

Kedar, S., Hajj, G. A., Wilson, B. D., & Heflin, M. B. (2003). The effect of the second order GPS ionospheric correction on receiver positions. Geophysical Research Letters, 30(16).

King, M., & Aoki, S. (2003). Tidal observations on floating ice using a single GPS receiver. Geophysical research letters, 30(3).

Kolker, A. S., Allison, M. A., & Hameed, S. (2011). An evaluation of subsidence rates and sea-level variability in the northern Gulf of Mexico.Geophysical Research Letters, 38(21).

Klobuchar, J. A. (1987). Ionospheric time-delay algorithm for single-frequency GPS users. Aerospace and Electronic Systems, IEEE Transactions on, (3), 325-331.

Kouba, J., & Heroux, P. (2001). Precise point positioning using IGS orbit and clock products. GPS solutions, 5(2), 12-28.

Kouba, J., & Springer, T. (2001). New IGS station and satellite clock combination. GPS Solutions, 4(4), 31-36.

Kouba, J. (2005). A possible detection of the 26 December 2004 Great Sumatra-Andaman Islands Earthquake with solution products of the International GNSS Service. Studia Geophysica et Geodaetica, 49(4), 463-483.

Lachapelle, G., & Alves, P. (2009). Multiple reference station approach: overview and current research. Positioning, 1(02), 1.

Leake, S. A. (1997). Land subsidence from ground-water pumping. US Geological Survey.

Li, Q., You, X., Yang, S., Du, R., Qiao, X., Zou, R., & Wang, Q. (2012). A precise velocity field of tectonic deformation in China as inferred from intensive GPS observations. Science China Earth Sciences, 55(5), 695-698.

Li, Z., Liu, G., & Ding, X. (2006). Exploring the Generation of Digital Elevation Models from Same-Side Ers Sar Images: Topographic And Temporal Effects. The Photogrammetric Record, 21(114), 124-140.

Lyard, F., Lefevre, F., Letellier, T., & Francis, O. (2006). Modelling the global ocean

tides: modern insights from FES2004. Ocean Dynamics, 56(5-6), 394-415.

Melbourne, T. I., Webb, F. H., Stock, J. M., & Reigber, C. (2002). Rapid postseismic transients in subduction zones from continuous GPS. Journal of Geophysical Research: Solid Earth (1978–2012), 107(B10), ETG-10.

Milliken, K. T., Anderson, J. B., & Rodriguez, A. B. (2008). A new composite Holocene sea-level curve for the northern Gulf of Mexico. Geological Society of America Special Papers, 443, 1-11.

Niu, Z., Min, W., Hanrong, S., Jianzhong, S., Xinzhao, Y., Weijun, G., & Bai, L. (2005). Contemporary velocity field of crustal movement of Chinese mainland from Global Positioning System measurements. Chinese Science Bulletin, 50(9), 939-941.

Ozawa, S., Nishimura, T., Suito, H., Kobayashi, T., Tobita, M., & Imakiire, T. (2011). Coseismic and postseismic slip of the 2011 magnitude-9 Tohoku-Oki earthquake. Nature, 475(7356), 373-376.

Phien-Wej, N., Giao, P. H., & Nutalaya, P. (2006). Land subsidence in Bangkok, Thailand. Engineering Geology, 82(4), 187-201.

Ray, J., Dong, D., & Altamimi, Z. (2004). IGS reference frames: status and future improvements. GPS solutions, 8(4), 251-266.

Rebischung, P., Griffiths, J., Ray, J., Schmid, R., Collilieux, X., & Garayt, B. (2012). IGS08: the IGS realization of ITRF2008. GPS solutions, 16(4), 483-494.

Rocken, C., Johnson, J., Van Hove, T., & Iwabuchi, T. (2005). Atmospheric water vapor and geoid measurements in the open ocean with GPS. Geophysical

research letters, 32(12).

Samper, L. (2011). Multisystem real time precise-point-positioning, Coordinates Magazine, Volume VII, Issue 2, 1-2.

Sato, H. P., Abe, K., & Ootaki, O. (2003). GPS-measured land subsidence in Ojiya City, Niigata prefecture, Japan. Engineering Geology, 67(3), 379-390.

Sato, M., Ishikawa, T., Ujihara, N., Yoshida, S., Fujita, M., Mochizuki, M., & Asada, A. (2011). Displacement above the hypocenter of the 2011 Tohoku-Oki earthquake. Science, 332(6036), 1395-1395.

Shanghai Geology Office (1976). Report on land subsidence in Shanghai (in Chinese)

Shi, C., Lou, Y., Zhang, H., Zhao, Q., Geng, J., Wang, R. ... & Liu, J. (2010). Seismic deformation of the M w 8.0 Wenchuan earthquake from high-rate GPS observations. Advances in Space Research, 46(2), 228-235.

Singh, M. M. (1986). Mine subsidence (No. CONF-8609178-). Society of Mining Engineers of AIME, Littleton, CO.

Snay, R. A. (1999). Using the HTDP software to transform spatial coordinates across time and between reference frames. Surveying and Land Information Systems, 59(1), 15-25.

Snay, R. A., & Soler, T. (2000). Modern terrestrial reference systems part 2: The evolution of NAD 83. Professional Surveyor, 20(2), 1-2.

Snay, R. A. (2003). Introducing two spatial reference frames for regions of the

Pacific Ocean. Surveying and Land Information Science, 63(1), 5-12.

Soler, T., & Snay, R. A. (2004). Transforming positions and velocities between the International Terrestrial Reference Frame of 2000 and North American Datum of 1983. Journal of surveying engineering, 130(2), 49-55.

Simms, A. R., Anderson, J. B., DeWitt, R., Lambeck, K., & Purcell, A. (2013). Quantifying rates of coastal subsidence since the last interglacial and the role of sediment loading. Global and Planetary Change, 111, 296-308.

Tornqvist, T. E., Wallace, D. J., Storms, J. E., Wallinga, J., Van Dam, R. L., Blaauw, M., ... & Snijders, E. M. (2008). Mississippi Delta subsidence primarily caused by compaction of Holocene strata. Nature Geoscience, 1(3), 173-176.

Wang, G. (2011). GPS landslide monitoring: single base vs. network solutions—a case study based on the Puerto Rico and Virgin Islands permanent GPS network. Journal of Geodetic Science, 1(3), 191-203.

Wang, G., & Soler, T. (2012). OPUS for horizontal subcentimeter-accuracy landslide monitoring: case study in the Puerto Rico and Virgin Islands region. Journal of Surveying Engineering, 138(3), 143-153.

Wang, G., Yu, J., Ortega, J., Saenz, G., Burrough, T., & Neill, R. (2013). A stable reference frame for the study of ground deformation in the Houston metropolitan area, Texas. Journal of Geodetic Science, 3(3), 188-202.

Wang, G., & Soler, T. (2013). Using OPUS for measuring vertical displacements in Houston, Texas. Journal of Surveying Engineering, 139(3), 126-134.

Wang, G., Kearns, T. J., Yu, J., & Saenz, G. (2014). A stable reference frame for landslide monitoring using GPS in the Puerto Rico and Virgin Islands region.

Landslides, 11(1), 119-129.

Xu, Y. S., Ma, L., Du, Y. J., & Shen, S. L. (2012). Analysis of urbanization-induced land subsidence in Shanghai. Natural hazards, 63(2), 1255-1267.

Xue, Y. Q., Zhang, Y., Ye, S. J., Wu, J. C., & Li, Q. F. (2005). Land subsidence in China. Environmental Geology, 48(6), 713-720.

Yang, Y., Ying-zhe, T., Chuan-lu, C., Min, W., Peng, Z., Xiao-rui, W. ... & Zu-sheng, Z. (2009). Integrated Adjustment of Chinese 2000 GPS Control Network. Survey Review, 41(313), 226-237.

Yi, L., Fang, Z., He, X., Shijie, C., Wei, W., & Qiang, Y. (2011). Land subsidence in Tianjin, China. Environmental Earth Sciences, 62(6), 1151-1161.

Yu, J., Wang, G., Kearns, T. J., & Yang, L. (2014). Is there deep-seated subsidence in the Houston-Galveston area?. International Journal of Geophysics, 2014.

Zhang, X. L. & Han, Q. D. (2002). Research on land subsidence and its countermeasure in Shanghai. Proc. 1st Symp. on Theory and Practice on Environmental Geotechnics, Shanghai, 57–63 (in Chinese).

Zumberge, J. F., Heflin, M. B., Jefferson, D. C., Watkins, M. M., & Webb, F. H. (1997). Precise point positioning for the efficient and robust analysis of GPS data from large networks. Journal of Geophysical Research: Solid Earth (1978–2012), 102(B3), 5005-5017.